DLR-IB-HR-OP-2019-77

Predictive Quantization for Staggered Synthetic Aperture Radar Systems

Masterarbeit

Nicola Gollin

Deutsches Zentrum
DLR für Luft- und Raumfahrt

Dokumenteigenschaften

Titel	Predictive Quantization for Staggered Synthetic Aperture Radar Systems
Betreff	Investigations for Tandem-L
Institut	Microwaves and Radar Institute
Erstellt von	Nicola Gollin
Beteiligte	Prof. Dr. Lorenzo Bruzzone (Supervisor), Michele Martone (Supervisor, DLR)
Geprüft von	Michele Martone, Dr. Paola Rizzoli (Head of the System Performance Group)
Freigabe von	Dr. Manfred Zink (Head of the Satellite SAR Systems Department)
Datum	02.07.2019
Version	1.0
Dateipfad	-

UNIVERSITÀ DEGLI STUDI DI TRENTO

Dipartimento di Ingegneria e Scienza dell'Informazione

Corso di Laurea in
Ingegneria dell'Informazione e delle Comunicazioni

ELABORATO FINALE

PREDICTIVE QUANTIZATION FOR STAGGERED SYNTHETIC APERTURE RADAR SYSTEMS

Relatore

Prof. Lorenzo Bruzzone

Correlatore

Dr. Michele Martone (DLR)

Laureando

Nicola Gollin

Anno accademico 2017/2018

Acknowledgments

Alla mia Famiglia

Oberpfaffenhofen, September 2018
Nicola Gollin

Abstract

For present and future spaceborne SAR missions, an increasing amount of onboard data is going to be required, due to the employment of large bandwidths, multiple polarizations, and large swath widths, which lead to hard requirements in terms of onboard memory and downlink capacity. In this context, SAR raw data quantization represents an essential aspect, since it affects both, the amount of data to be stored and transmitted to the ground, and the quality of the resulting SAR products. In this master thesis, a data reduction approach based on predictive quantization is investigated in the context of Tandem-L, a DLR proposal for a highly innovative L-band radar satellite mission to monitor the dynamic processes of the Earth. Tandem-L employs staggered PRI, a novel acquisition mode which allows for a swath width up to 350 km and an azimuth resolution in the order of 10 m, resulting in a required data volume of about 8 Terabyte per day. In this case, a certain azimuth oversampling is mandatory in order to properly reconstruct the data in presence of the gaps introduced by the staggered SAR mode. The proposed technique takes advantage of the time variant autocorrelation properties of the non-uniform azimuth raw data stream in order to reduce the amount of data through a novel quantization method, named Predictive-Block Adaptive Quantization. Different prediction orders are investigated by considering the trade-off between achievable performance and complexity. Simulations for different target scenarios show that a data reduction of about 10-15% can be achieved with the proposed technique with a modest increase of the system complexity. Moreover, having a-priori information on the position of the gaps, a technique for their reconstruction based on dynamic bit allocation has been successfully implemented, showing no significant loss of information.

List of Figures

List of Tables

Contents

1 Introduction

In the last decades, satellite Synthetic Aperture Radar (SAR) applications have become of great interest for the scientific community. The capability of those systems allows to provide a high resolution imaging independent from daylight, weather conditions and cloud coverage. For present and future spaceborne SAR missions, an increasing amount of onboard data is going to be required, due to the employment of large bandwidths, multiple polarizations, and large swath widths, which lead to hard requirements in terms of onboard memory and downlink capacity. In this context, SAR raw data quantization represents an essential aspect, since it affects both, the amount of data to be stored and transmitted to the ground, and the quality of the resulting SAR products. In the following subsection the problem is introduced and the goal of the thesis is reported.

A big challenge for future spaceborne remote sensing missions is now turning to the estimation and long-term monitoring of dynamic processes in the Earth's environmental system, such as deformation events, forest and biomass change, and ocean surface currents. The German Aerospace Center (DLR) is investigating an innovative single-pass interferometric and fully polarimetric L-band radar mission, named Tandem-L, which exploits innovative high-resolution wide swath SAR modes, together with the use of large bandwidths, high pulse repetition frequencies, and multiple acquisition channels, resulting in an achievable swath width of about 350 km on ground. Such an increase in term of coverage has as a main drawback the generation of a huge amount of onboard data, which is of around 8 Terabytes per day. One of the proposed solutions to reduce the resulting onboard data reduction suggests to perform a complex onboard processing (i.e. an onboard interpolation, low-pass filtering and decimation) and allows a data reduction up to 50% [23][21]. On the other hand, the onboard computational memory required for the data reduction processing is at the limit of the hardware components, leading to high energy consumption. Moreover, the practical realization of the technique is very complex, including many specific coefficients which must be correctly selected during acquisition. The research of alternative solutions is therefore of great interest in order to have different options to choose for the mission development, which motivates the present master thesis. In this work, a data reduction strategy based on Linear Predictive Coding (LPC) is investigated in the context of Tandem-L. The method has been designed to reduce the complexity as much as possible while achieving a certain data reduction. A mathematical formulation for the novel technique is an interesting goal for understanding in which situation the present method can be more or less efficient. The resulting performance has been verified through Monte Carlo simulations in order to evaluate the solution under different aspects (i.e. final performance versus resulting system complexity). Moreover, other complications introduced by the Tandem-L system such as the presence of missing samples (so-called gaps) during the acquisition, have been investigated and successfully solved through novel coding strategies.

The thesis is structured as follows. In Section 2 the principles of SAR systems are recalled, including specific details of the processing necessary to retrieve the data from

the received echoes. An advanced measurement technique named Interferometric SAR is also reported as the Tandem-L mission will have this features. The specific case of Tandem-L mission is described in Section 3, giving a detailed overview about the mission characteristics and objectives. A specific explanation of the capability of the system is reported also to introduce the problem of onboard data amount. The basics of quantization are reported in Section 4, with both general concepts of real world quantizers and performance evaluations. A specific configuration named Block Adaptive Quantization is also described, being the actual state of the art for satellite SAR system quantization. In Section 5 the Linear Predictive Coding technique, a specific data encoding compression method, is introduced. The application of this technique on SAR system is investigated, giving specific information on a novel quantization method and its theoretical investigation. The result of the analysis are discussed in Section 6, where are also compared with the state of the art technique in quantization. In the last section the conclusion of the work are presented, as well as some outlook for future research steps.

2 Theoretical Background

2.1 Synthetic Aperture Radar (SAR) Remote Sensing

Synthetic Aperture Radar (SAR) is an active remote sensing technique aimed at mapping and monitoring the Earth surface. Atmospheric phenomena such as clouds and fog do not have significant impact on SAR measurements, allowing this type of systems to perform in any weather condition. Moreover, being an active system (i.e. it provides its own illumination), SAR can perform independently also from solar illumination, while using optical passive sensors this is not possible. SAR systems are usually equipped on satellite or airborne platforms, both offering advantages and disadvantages for different applications. While satellites are more stable and guarantee a longer mission lifespan, airborne platforms can achieve higher resolution and are less expensive. SAR systems can either be monostatic or bistatic if one or two sensors are employed for transmission and reception, respectively. In general, radar systems are microwave imaging sensors characterized by an azimuth resolution which is limited by the antenna dimension. Since the antenna beam width is inversely proportional to its dimension (i.e. size), a smaller antenna will be less directive. Thus, to obtain a sufficient resolution, a longer antenna is necessary. This is the case of Real Aperture Radar (RAR), for which the azimuth resolution is given by

$$\delta_a = \theta_h R_0 = \frac{\lambda}{L_a} R_0, \tag{1}$$

where λ is the wavelength, L_a is the azimuth antenna length and R_0 is the the slant range. As an example, for a system with a 5 m antenna, operating in L band ($\lambda =$25 cm) and a flying orbit of 500 km, the azimuth resolution will be in the order of kilometers. A longer antenna could improve the δ_a but the physical and mechanical constraints imposed by airborne and particularly spaceborne platforms do not allow antennas of longer dimension. To overcome this limitation, Synthetic Aperture Radars (SAR) exploits the high stability of the moving platform (better in spaceborne systems) considering the formation of a synthetic antenna [18]: an appropriate combination of the received echoes allows to construct a virtual aperture much longer than the physical antenna, hence achieving resolutions which are suitable for the observation of physical and geometrical parameters on the Earth's surface.

2.1.1 SAR Acquisition Concept

The geometry of a SAR acquisition (valid in general for airborne or spaceborne) is shown in Figure 1. The platform moves along the *radar track* (azimuth direction) at a given height h_s and a given speed v_s, whereas the *slant range* is the direction perpendicular to the radar's flight path and is indicated by R_0. The *swath width* W_g is the ground range extension of the radar scene and is given by

$$W_g = \frac{\lambda R_0}{W \cos \theta_i},\tag{2}$$

where W is the antenna length in elevation, and θ_i is the incidence angle defined between the range direction and the normal on the surface. The azimuth footprint extension is instead defined as

$$L_s = \frac{\lambda R_0}{L},\tag{3}$$

where L is the antenna length in azimuth direction. Differently from the range extension, the azimuth scene extension depends (for most of the acquisition modes) on the data take duration. From equation (3), as well as from Figure 1, it is possible to notice that the antenna footprint L_s in azimuth is also equivalent to the *synthetic aperture*, which is defined as the azimuth extension within which a point on ground is "seen" by the radar pulses.
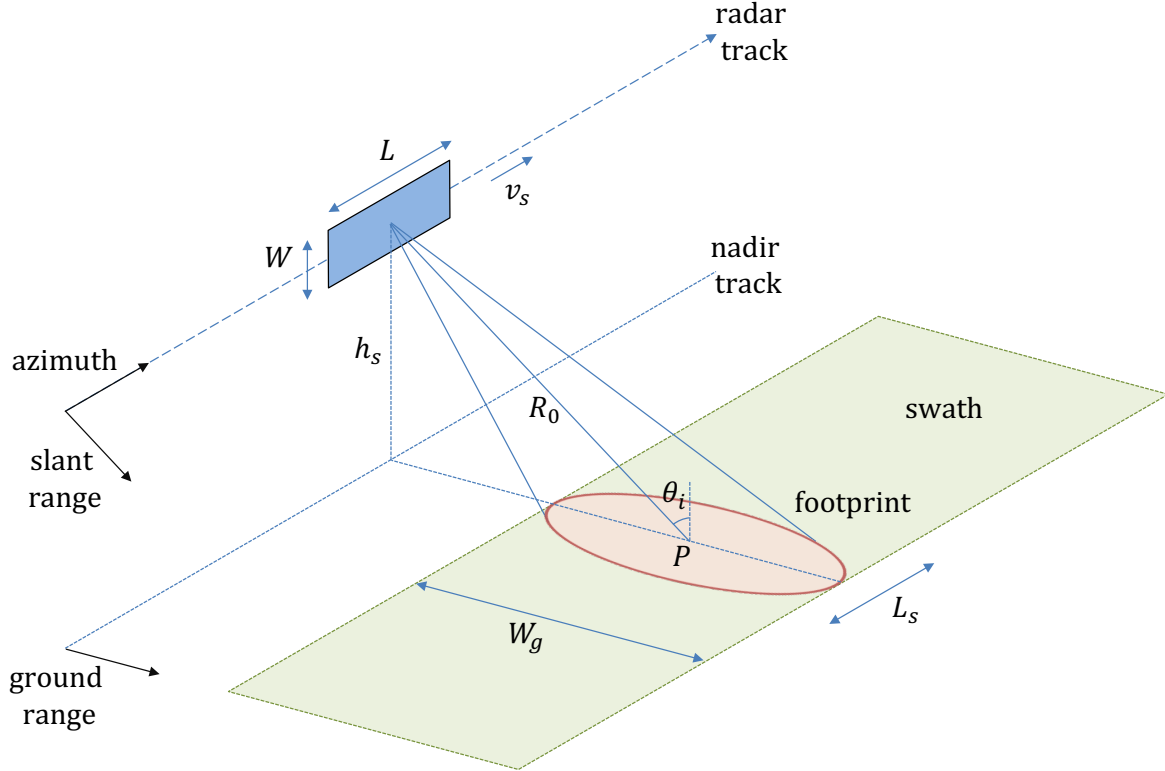
Figure 1: SAR Geometry

The SAR systems transmits a radar wave which impinges the targeted area with an incidence angle θ_i defined from the range vector and the normal to the surface. The antenna footprint directly depends on the antenna dimension in both direction, according to (2) and (3). SAR are coherent radar systems, meaning that the amplitude and phase of the received echo are recorded, which are dependent on both, the physical and dielectric properties of the irradiated target, as well as on the sensor parameters, such as the antenna

4

pattern and the wavelength. The received signal is weighted by the antenna pattern both in transmission and reception. For rectangular apertures, the antenna pattern G can be reasonably approximated by

$$G(\psi_a, \psi_r) = \operatorname{sinc}^2\left(\frac{L}{\lambda}\psi_a\right) \operatorname{sinc}^2\left(\frac{W}{\lambda}\psi_r\right),\tag{4}$$

where ψ_a and ψ_r are the off-center angles in azimuth and range direction, while the sinc functions are squared to consider both transmission and reception process. As known in radar systems, the energy of the antenna pattern is typically considered between the half power beamwidth angles (3 dB). If a sinc^2 pattern is considered, the half power beamwidth is located at $\pm 0.443\frac{\lambda}{W}$, hence the range and azimuth beamwidths can also be expressed as

$$\beta_r = 0.886\frac{\lambda}{W}\tag{5}$$

$$\beta_a = 0.886\frac{\lambda}{L}.\tag{6}$$

The proper definition of the SAR geometry is of crucial importance to accurately describe and model the performance of the SAR system under consideration. Typically, it is possible to employ a spherical Earth approximation, as shown in Figure 2 and Figure 3. In particular, the satellite velocity is a critical parameter in order to describe theoretically the antenna pattern and its properties. The relevance of the each parameter will be analyzed in detail in Section 5.2.
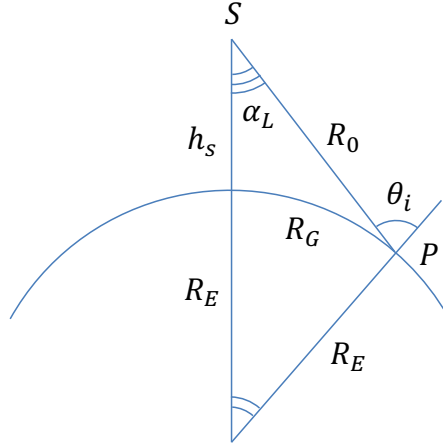
Figure 2: Spherical SAR Geometry in the plane defined by the Earth's center, a point scatterer P and the radar closest approach to it R_0. The height of the satellite is expressed as h_s, while R_e represents the radius of the earth.

In Figure 2, it is pictured the spherical SAR geometry in the plane of earth's center, the point scatterer P and the closest radar approach R_0. It is possible to notice that the observation angle α_L is different from the incidence angle θ_i due to the earth's curvature.
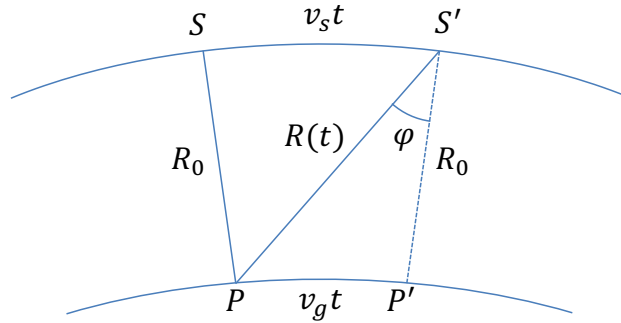
Figure 3: Spherical SAR Geometry in the plane defined by the radar track and the point scatterer P.

Considering S the position of the antenna (pictured in Figure 3) in the closest position to the scatterer P (at time $t = 0$), at time t the radar will have moved to S' with speed v_s. The speed of the radar beam on ground is denoted as v_g and can be approximated as

$$v_g \cong v_s \frac{R_E}{R_E + h_s}. \tag{7}$$

The range of the radar to the point scatterer $R(t)$ can be expressed as

$$R(t) \cong \sqrt{R_0^2 + (v_r t)^2} \cong R_0 + \frac{(v_r t)^2}{2R_0}, \tag{8}$$

where the effective speed v_r is the geometric mean of v_s and v_g

$$v_r = \sqrt{v_s v_g}. \tag{9}$$

Finally, the azimuth angle ϕ is derived as

$$\tan \phi = \frac{v_g t}{R_0}. \tag{10}$$

2.1.2   SAR Imaging Modes

SAR systems can acquire data in different modes, hence exploiting the typical trade-off between spatial coverage and azimuth resolution, which are shown in Figure 4 and shortly recalled in the following.

- **Stripmap**: Is the standard mode in SAR systems. The acquisition is performed through a fixed antenna pattern and thus a single swath is imaged as the platform moves (Figure 4a). It is a continuous imaging mode since the azimuth extension may vary depending on the data take duration. The swath width for this methodology is typically of about 30 to 50 km, maintaining an azimuth resolution of 5 m or less.

<table>
<tr><td>(a) Stripmap.</td><td>(b) ScanSAR.</td><td>(c) Spotlight.</td></tr>
</table>
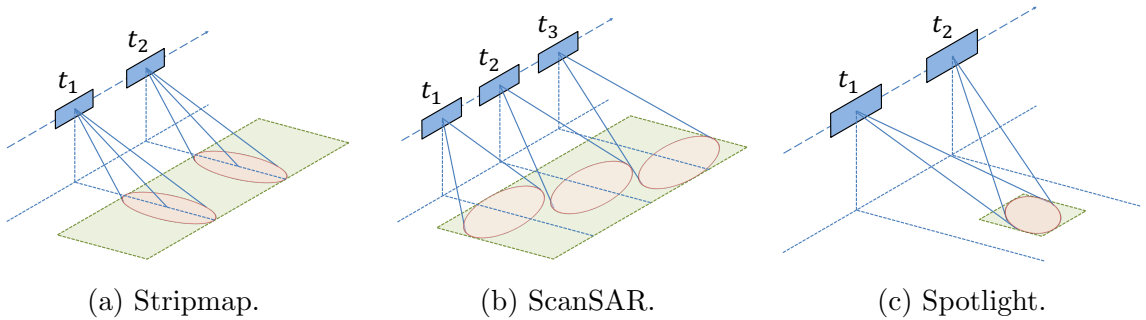
Figure 4: SAR acquisition modes.

- **ScanSAR**: If a wider area has to be covered, the antenna elevation pattern is steered to different elevation angles, which leads to multiple sub-swaths (Figure 4b). Each sub-swath is illuminated by a shorter Section of pulses with respect to the Stripmap mode, leading to a degraded azimuth resolution of around 15 m or more. On the other hand, after an appropriate processing, the resulting acquisition covers a larger swath, usually in the order of hundreds of kilometers. Like Stripmap, also ScanSAR is a continuous imaging mode.

- **Spotlight**: When, on the other hand, a finer resolution is required, the antenna pattern is steered in azimuth towards a fixed point (Figure 4c). The synthetic aperture is maximized, giving the highest resolution achievable by the system, usually in the order of 1 m or below. The counterpart of this gain in resolution is the lack of the continuous imaging mode, meaning that the acquisition is not anymore continuous in the azimuth direction but is fixed on a patch with a typical extension of a few kilometers. To increase the coverage multiple, non-contiguous patches (also called "vignettes") can be recorded during a single radar flight.

2.2 SAR Image Formation

The set of raw echoes received by the SAR sensor fills a two dimensional matrix of unresolved dispersed reflections from the scatterers on ground, hence a SAR acquisition represents the projection of the 3D information (imaging) into a 2D matrix of *unfocused* echoes in both (range and azimuth) dimensions. The required processing to retrieve the SAR *focused* data consist mainly in a convolution of the raw data with the reference function of the system in range and azimuth dimension. To shortly recall, the convolution of two functions f and g is defined as

$$f * g = \int_{-\infty}^{+\infty} f(\tau) g(t - \tau) \, d\tau. \tag{11}$$

SAR systems usually employs for transmission a *chirp* signal, which is a frequency modulated pulse waveform, characterized by a constant amplitude in time and a pulse time τ. The instantaneous frequency of a chirp signal is linearly varying over time t according to $f_i = k_\tau t$, where k_τ is the chirp rate, which also defines the range bandwidth $B_\tau = k_\tau \tau$.

The chirp signal is defined as

$$g(t) = \cos\left[\phi_0 + 2\pi\left(f_0 t + \frac{k_\tau t^2}{2}\right)\right] + j \cdot \sin\left[\phi_0 + 2\pi\left(f_0 t + \frac{k_\tau t^2}{2}\right)\right], \qquad (12)$$

where f_0 and ϕ_0 represents the carrier frequency and its phase respectively. After the chirp transmission the *echo window* follows, a time interval in which the radar receives the reflected signal from the target and stores it in the on-board memory. Such a transmission and reception process is repeated every Pulse Repetition Interval (PRI), which is the reciprocal of the Pulse Repetition Frequency (PRF = 1/PRI). In order to take into account timing constraints (which are out of the scope of this thesis and will not be detailed), typical PRFs for spaceborne SAR systems are in the order of a few thousand of Hertz.

The time variable in the azimuth direction (*azimuth time*) is often referred to as *slow time*, since it is in the order of seconds (i.e. the duration of the SAR acquisition). On the other hand, the *range time* is denoted as *fast time*, because the time delay between transmission and reception for the imaged swath is in the order of tens of microseconds. By knowing the antenna pattern, the amplitude and phase of the raw azimuth signal at time t can be obtained from $R(t)$ and ϕ, reported in equation (8) and (10) respectively.

The received waveform is amplified, down-converted to the baseband and then discretized in time and amplitude, (by means of sampling and quantization operation, respectively) by an analog-to-digital converter (ADC). Once digitized, the raw data are transmitted on ground through the downlink antenna. Here the SAR processing is carried out, which consists in a two matched filter operations, one in range and one in azimuth direction as shown in Figure 5.
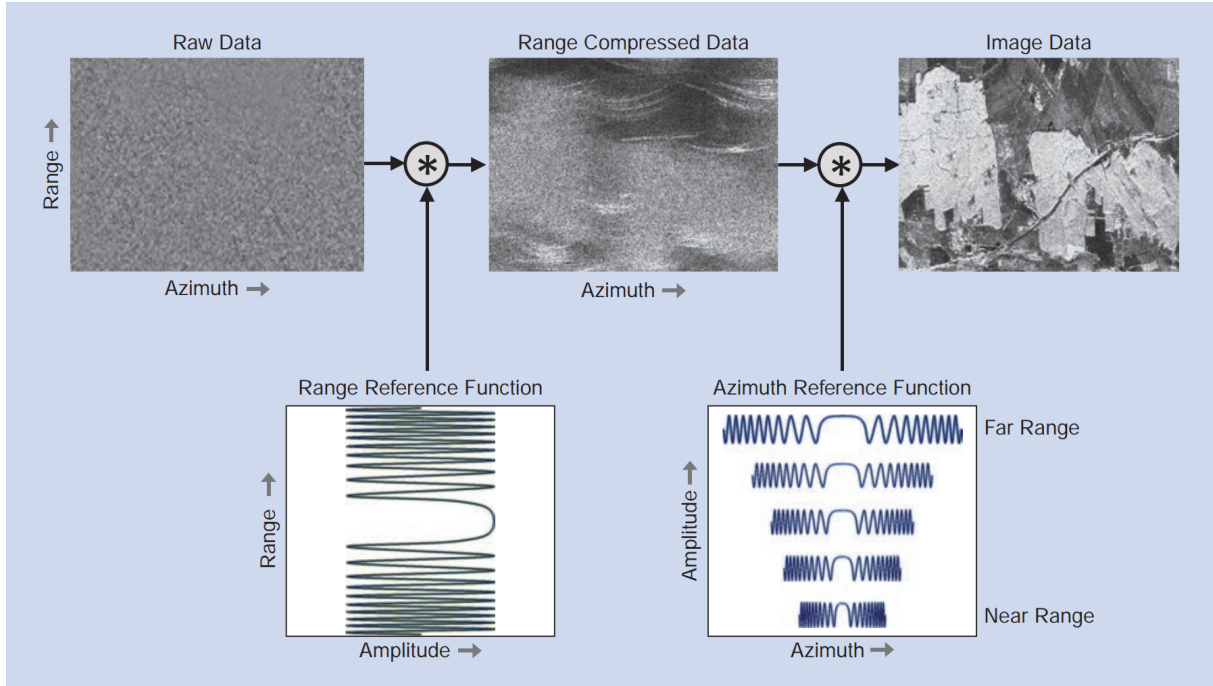
Figure 5: SAR Processing workflow.

2.2.1   Range Focusing and Resolution

Focusing operation is fundamental in order to opportunely visualize the received data and retrieve the information needed. The range compression process is carried out by exploiting the range reference function (RRF), which is the complex conjugate of the transmitted chirp signal

$$s_r(t) = g^*(t) \tag{13}$$

where $g(t)$ is the envelope defined in (12). Usually, the RRF is weighted with a Hamming filter to reduce side lobe effects, then is transformed through a Fast Fourier Transform (FFT) in the frequency domain. This transformation is way more efficient from the computational point of view since the convolution operation in time domain is a multiplication in frequency domain. The result of the multiplication is then re-transformed in time domain, giving the range compressed data, which reveals only the distance between the radar and all the points of the ground belonging to the swath.

The range resolution of the system depends on the pulse coding. Considering a chirp waveform with a duration of τ seconds, the distance in slant range between two targets Δ_R and c_0 as the speed of light, it is possible to define the time delay between the two received echoes reflected from the two targets

$$\Delta_t = \frac{2\Delta_R}{c_0}. \tag{14}$$

From that, to clearly separate the two echoes, , i.e. to avoid the echo overlapping of the two backscattered waves, the chirp length τ should satisfy the following condition

$$\tau \leq \frac{2\Delta_R}{c_0}, \tag{15}$$

from which the range resolution of a SAR system can be derived as

$$\delta_\tau = \frac{c_0}{2B_\tau}. \tag{16}$$

In the above equation the relationship $B_\tau = \frac{1}{\tau}$ has been exploited. As it can be noticed, the range resolution is not subject to any geometrical parameter of the antenna, being uniquely dependent on the chirp bandwidth B_τ.

2.2.2   Azimuth Focusing and Resolution

Similarly to the range compression, the azimuth compression is performed by multiplying all azimuth lines in frequency domain by the azimuth reference function (ARF), which is the complex conjugate of the expected response from a point target on ground. It is possible to express the ARF considering a point scatterer at range $R(t)$

$$s_a(t) = A \sqrt{\sigma_0} e^{i\phi_s} e^{-i\frac{4\pi}{\lambda}R(t)}. \tag{17}$$

In the above expression, A is the amplitude of the signal, σ_0 is the radar cross section and ϕ_s is the scattering phase. The exponent $\frac{4\pi}{\lambda}R(t)$ gives the contribution of phase variation with respect to the time-varying distance $R(t)$.

As introduced in Section 2.1, real aperture radars have a very limited azimuth reso-

lution due to the geometrical constraint of the antenna dimension. Thus, the synthetic aperture is exploited in order to overcome this limitation by considering a synthetic virtual antenna which is much longer then the physical one, which corresponds to the path length of the antenna during which the scattered echo from a point target is received.
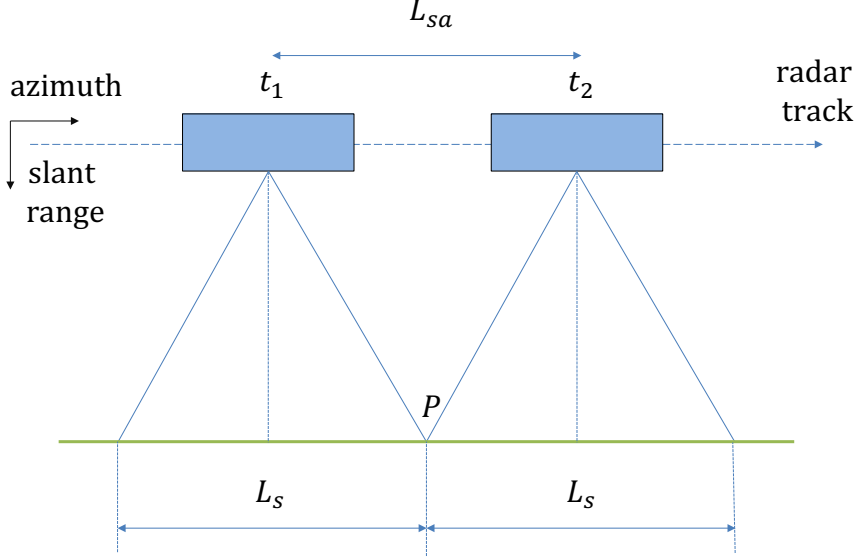
Figure 6: Synthetic aperture L_{sa} and the azimuth antenna footprint L_s, $L_{sa} = L_s$.

The beamwidth of an antenna of length L_s is derived in (3), and equals the synthetic aperture L_{sa}. By coherently combining all returns received by the SAR from the point P in Figure 6, the best attainable resolution achievable by a SAR system is

$$\delta_a = \frac{L}{2}. \tag{18}$$

The above equation shows that, for a SAR system, the azimuth resolution is directly proportional to the azimuth antenna length (hence, a short antenna yields a finer resolution) and, most important, that it is independent of the distance between satellite and target. This apparently surprising conclusion can be explained if considering that a radar with a shorter antenna will have a wider beamwidth and is therefore able to see any point on the ground for a longer virtual antenna length, hence achieving a better azimuth resolution. However, this result must be subjected to further constraints considering e.g. the system timing and the sampling process. Indeed, in azimuth direction the sampling rate must be larger than the Doppler bandwidth (B_d) of the signal, according to the well known Shannon sampling theorem. The sampling rate is equal to the PRF of the system, giving the following equations

$$\mathrm{PRF} \geq B_d \quad \text{or} \quad v_s \cdot \mathrm{PRI} \leq \frac{L}{2}. \tag{19}$$

10

From (19) comes out that for movement of $L/2$ at least one sample should be recorded. If the PRF is increased, to achieve e.g. the best attainable resolution as in (18), the receiving echo window must be consequently decreased, hence limiting the swath width. It is clear that the trade-off between sampling rate and swath width must be taken into account in SAR systems design. To overcome this limitation, multi-channel SAR system systems have been investigated in the last decade [4][9], which are often referred to as High Resolution Wide Swath (HRWS) SAR systems. On the other hand, by considering such systems a much larger amount of data is going to be generated, which requires proper methodologies to be efficiently stored on board as well as transmitted to the ground.

2.3   Radar Parameters

The informative level contained in the SAR data is dependent on the several parameters which have been introduced in the previous Section. In particular, the wavelength determines the backscattered power and the Signal-to-Noise-Ratio (SNR) of the imaged area: the backscattering level of a surface having rough scattering in X band (λ=3.1 cm) may be smooth and specular if irradiated in L band (λ=23 cm). The polarimetric capability of a SAR also influences the radar signature of an object, meaning that the same object has a different backscattering properties if different polarization combinations in transmission and reception are considered (e.g. HH or HV, where H stands for horizontal and V for vertical polarization). Fully polarimetric SAR systems exploit this important feature by extracting information on the scattering mechanism as volume scatterers, surface scatterers and multiple scatterers. The incidence angle θ_i is another parameter for determining the backscatter level, which decreases with shallow values of θ_i (i.e. for a given altitude h the range increases with increasing the incidence angle, hence lowering the SNR). As introduced before, the range resolution depends on the chirp bandwidth B_τ, whereas the (best attainable) azimuth resolution equals half of the azimuth antenna size.

2.3.1   Distributed Scatterers and Speckle

Scatterers observed by SAR systems can be divided in two different classes: *point scatterers* and *distributed scatterers*. The former are considered as a main dominant scatterer within the resolution cell, while the latter are considered as an ensemble of non-dominating scatterers within the resolution cell. In this last case, the backscatter level is generated as the sum of those non-dominating scattering elements. It is possible to assume the *distributed scatterers* as a normal random distribution applying the central limit theorem. While for medium resolution SAR systems and most of land covers this assumption is valid under the condition of a circular distribution of the scatterers, for high resolution systems and artificial scatterers (such as urban areas), this assumption may be not valid anymore. Considering a circularly distributed Gaussian complex image, its probability density function (PDF) can be modeled as

$$f_x(x) = \frac{1}{\pi \bar{I}} \exp \left\{ \frac{Re(x)^2 + Im(x)^2}{\bar{I}} \right\}, \qquad (20)$$

where $\bar{I}$ is the intensity of the complex image $f_x(x)$. Moreover, no correlation between the real and imaginary part of the scatterers is typically assumed, meaning that also the magnitude and phase are independent from each other. It is possible to define the PDF

11

of the intensity and of the magnitude of a given pixel, respectively, as

$$f_i(I) = \frac{1}{\bar{I}} \exp\left\{\frac{-I}{\bar{I}}\right\} \qquad where \qquad I = |x|^2 \tag{21}$$

$$f_x(M) = \frac{2M}{\bar{I}} \exp\left\{\frac{-M^2}{\bar{I}}\right\} \qquad where \qquad M = |x|. \tag{22}$$

By calculating the average power received for distributed scatterers, multiple scatterers are not considered and the total average power is defined as the sum of all power contributions from each individual particle. The received power is known through the radar equation, defined as

$$\bar{p}_r = \frac{P_t G^2 \lambda^2}{4\pi^3} \sum_i \frac{\sigma_i}{R_i^2}, \tag{23}$$

where P_t is the transmitted power and G is the antenna gain (considered squared for both transmission and reception), λ is the wavelength. The second part of the equation describes the scattering contribution as a summation of single scatterers, considering R_i the individual distance from the radar. The spatial variance of scatterers within a resolution cell over a mean value is defined *speckle*. *Speckle* is often referred to as a noise contribution, which is related to the random disposition of scatterers within a resolution cell, and is reasonably modeled as a multiplicative process. Thus, an increasing amount of power in transmission to suppress this disturbance is pointless, as the noise variance increases as the transmitting power increases. On the other hand. in order to mitigate speckle, a non-coherent (i.e. involving only the signal intensities) averaging process known as *multilooking* can be performed. Even though the multilooking process causes a degradation in the resulting resolution, it removes speckle, hence increasing data interpretability. Since speckle is related to the spatial variance of the backscattered signal within a resolution cell, a higher resolution reduces the number of scatterers, leading to a lower speckle. Multilooking process can be therefore understood as a low-pass filtering on the image and can be implemented following different approaches:

- **Spatial Domain Approach:** Adding the neighbouring pixels in all direction (within a certain window) and perform an average on the number of pixels.

- **Time Domain Approach:** Dividing the synthetic aperture in multiple sections and process each of them as a single section according to the number of looks.

- **Frequency Domain Approach:** Performs the same synthetic aperture separation of the Time Domain Approach defining the segments in Frequency domain, i.e. considering Doppler and range sub-bands according to the number of looks.

Multilooking process improves the overall radiometric accuracy, but also introduces, as a drawback, a degradation in resolution. The impact in terms of accuracy gained and loss in resolution is dependent on the number of looks: the more the looks, the higher the radiometric accuracy and the lower the resulting resolution.

2.3.2 Backscatter Intensity, σ_0

Once they have been acquired and properly processed, SAR images display the amount of reflectivity of the captured area on ground. The higher the reflectivity of the targets, the higher the intensity of the image area associated to them. The reflectivity variation of the scene imposes two more steps in SAR process chain: calibration and geocoding. The first is carried out by defining a relationship between the measured value σ_0 and the known reflectivity of an object, as, e.g., a corner reflector. Geocoding, instead, is the conversion of backscattering value from slow/fast time (t, τ), to the real position of ground (latitude/longitude). The side-looking geometry of SAR system introduces geometrical distortions mainly caused by the mapping of a three dimensional scene in a two dimensional plane. If considering variations in elevation within the scene, three kinds of distortions may occur, as shown in Figure 7.

(a) Layover. (b) Foreshortening. (c) Shadow.
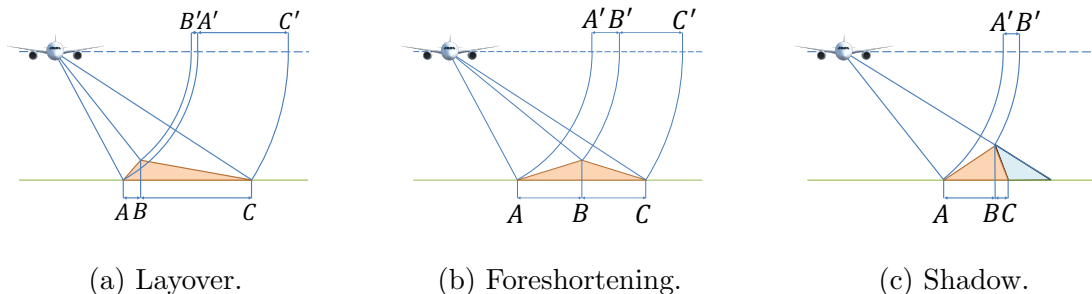
Figure 7: Side-Looking geometry distortion.

Layover (Figure 7a) occurs when the terrain shows a high slope angle, reducing the range of the portion of the target located higher in altitude. *Foreshortening* (Figure 7b) is the wrong relative distance from the satellites of elevated targets, while *Shadow* areas obstruct the transmitted wave, giving no scattering information of the area that lies in the shadow. The occurrence of these distortions can be described by means of specific relationship among the elevation (i.e. look) angle and the local terrain slope.

2.4 Interferometric SAR (InSAR)

SAR systems retrieve information of the targeted area by exploiting the scattering properties of the targets. Interferometric SAR systems (InSAR) usually features a bi-static or a multi-static configuration, performing an acquisition of the scene in different space positions and/or time instances. The amount of information with this type of technique is highly informative, especially if considering the phase information between two or more acquisitions. In particular, the phase is made up of two different contributions: the *propagation phase* and the *backscattered phase*. While the first is related to the distance between the sensor and the scatterer, the latter includes the contributions of phase difference given by the target properties. InSAR measurements are used to estimate with high accuracy geophysical parameters such as ground deformation, glacier movements and altitude topography (also named Digital Elevation Models, DEMs). Since differences of phase are taken into account in InSAR processing, the accuracy of the measure can be in the order of centimeters and even millimeters. Having such a high precision from a satellite platform with all its advantages (i.e. altitude stability, revisit time and operational life), in
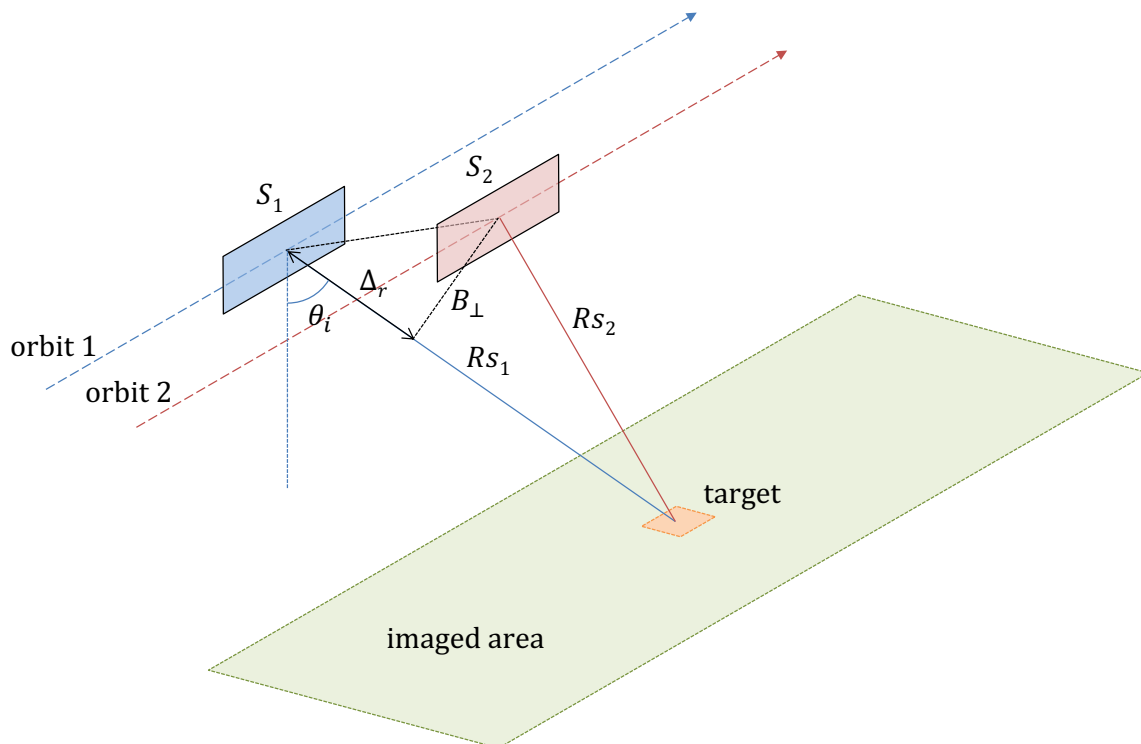
Figure 8: Interferometric SAR acquisition.

the last decades InSAR missions are increasing their interest and relevance in the context of remote sensing applications, both in spaceborne and airborne systems.

2.4.1 Acquisition Modes

An InSAR acquisition can be carried out in the same time instance, featuring two receiving antennas, or at difference time frames, by revisiting the targeted area. The two images are said to be acquired in **single pass mode** if the time lag between them is zero, otherwise the interferometric acquisition is carried out in **repeat pass mode**. If the two satellites are aligned in the along track dimension, it is said to be **along track interferometry**, which is very effective for the estimation of the ocean currents and sea surface spectrum, and usually operated in single pass mode to maximize the temporal correlation between the two acquisition. By aligning the two platforms in the across track direction (i.e. perpendicular to the flight direction), the acquisition is said to be **across track interferometry**. This configuration is suitable for the generation of DEMs, both in single and repeat pass mode. For a coherent combination of the two interferometric images, a co-registration is mandatory, meaning that the value of the pixels of an image (*slave*) must be interpolated to fit the geo-coded pixel grid of the other image (*master*). A sketch of an interferometric acquisition is given in Figure 8. The interferometric phase between the two sensors S_1 and S_2 is given by

$$\Delta_\phi = \frac{4\pi}{\lambda}\Delta_r, \tag{24}$$

where Δ_r is the travel path different between the two received signals. If single pass mode is considered, $\Delta_r = 2(Rs_1 - Rs_2)$, while in repeat pass configuration $\Delta_r = Rs_1 - Rs_2$ (if S_1 is considered as master). The perpendicular baseline between the two platforms is defined as $B_\perp$, while h is the height of the target and θ_i is the incidence angle (in this example, flat Earth and topography are assumed for simplicity). From the interferometric configuration of Figure 8 it is moreover possible to define the height of ambiguity (HoA), which corresponds to a complete 2π cycle of the interferometric phase, as

$$\text{HoA} = \frac{\lambda \cdot Rs_1 \cdot \sin(\theta_i)}{B_\perp}, \tag{25}$$

where λ is the radar wavelength, $Rs1$ is the slant range, θ_i is the incidence angle and $B_\perp$ is the baseline perpendicular to the line of sight.

2.4.2 Coherence and Phase Errors

InSAR acquisitions are evaluated trough the interferometric coherence γ. γ represents the normalized complex correlation between the *master* and the *slave* images, giving information on the amount of noise present in the interferogram, and is defined as

$$\gamma = |\gamma| \cdot e^{j\phi} = \frac{E\left[s_1 \cdot s_2^*\right]}{\sqrt{E[|s_1|^2]} \cdot \sqrt{E[|s_2|^2]}}. \tag{26}$$

The operator E indicates the statistic mean, i.e. the expectation of the corresponding random variable. Considering X a random variable made up of finite samples $x_1, x_2, \ldots, x_m$ and associated to a given probability $p_1, p_2, \ldots, p_m$, the expectation of X is given by

$$E[X] = \sum_{i=1}^{m} x_i p_i. \tag{27}$$

The coherence can be modeled as the product of different noise sources, assuming statistical independence between them. It is defined as

$$\gamma = \gamma_{\text{SNR}} \cdot \gamma_{\text{Quant}} \cdot \gamma_{\text{Amb}} \cdot \gamma_{\text{Rg}} \cdot \gamma_{\text{Az}} \cdot \gamma_{\text{Vol}} \cdot \gamma_{\text{Temp}}, \tag{28}$$

where γ_{SNR} is the coherence loss due to the limited SNR, γ_{Amb} is related to ambiguities decorrelation, γ_{Rg} is the baseline decorrelation, γ_{Az} models the coherence loss due to the relative Doppler shift spectra, γ_{Vol} represents the volume decorrelation contribution while γ_{Temp} is the temporal decorrelation. Here, γ_{Quant} is the coherence loss in raw data quantization. Being γ a product of noise sources, any contribution smaller than 1 will degrade the overall performance.

The most relevant contribution in the overall coherence is typically the γ_{SNR}. The finite sensitivity in the receivers causes a loss in the SNR, and is defined as

$$\gamma_{\text{SNR}} = \frac{1}{\sqrt{(1 + \text{SNR}_1^{-1}) \cdot (1 + \text{SNR}_2^{-1})}}, \tag{29}$$

where SNR_1 and SNR_2 are the SNRs for each channel, and can be obtained as

$$\text{SNR} = \frac{\sigma_0(\theta_i)}{\text{NESZ}_{1,2}(\theta_i)}. \tag{30}$$

In the upper equation σ_0 is the normalized backscattering coefficient, defined as function of the incidence angle (θ_i) and the NESZ (Noise Equivalent Sigma Zero) is the measure of sensitivity of the system (i.e. its "noise floor").

Being the interferometric phase error a key parameter in InSAR systems, its probability density function can be defined as

$$p_\phi(\phi) = \frac{\Gamma\left(N_l + \frac{1}{2}\right)\left(1 - \gamma_{tot}^2\right)^{N_l} \gamma_{tot}\cos(\phi)}{2\sqrt{\pi}\Gamma(N_l)\left(1 - \gamma_{tot}^2\cos^2\phi\right)^{N_l + \frac{1}{2}}} + \frac{\left(1 - \gamma_{tot}^2\right)^{N_l}}{2\pi}F\left(N_l, 1; \frac{1}{2}; \gamma_{tot}^2\cos^2\phi\right), \tag{31}$$

where ϕ is the interferometric phase difference, Γ is the gamma function, N_l is the number of looks and F is the hypergeometric function [10]. The standard deviation of the single-point phase error is a typical parameter to define the performance of the system.

$$\sigma_\phi = \sqrt{\int_{-\pi}^{+\pi} \phi^2 p_\phi(\phi)\ \mathrm{d}\phi} \tag{32}$$

The relationship between the total coherence and the interferometric phase is shown in Figure 9, where the number on each curve represents the corresponding number of looks (N_l).
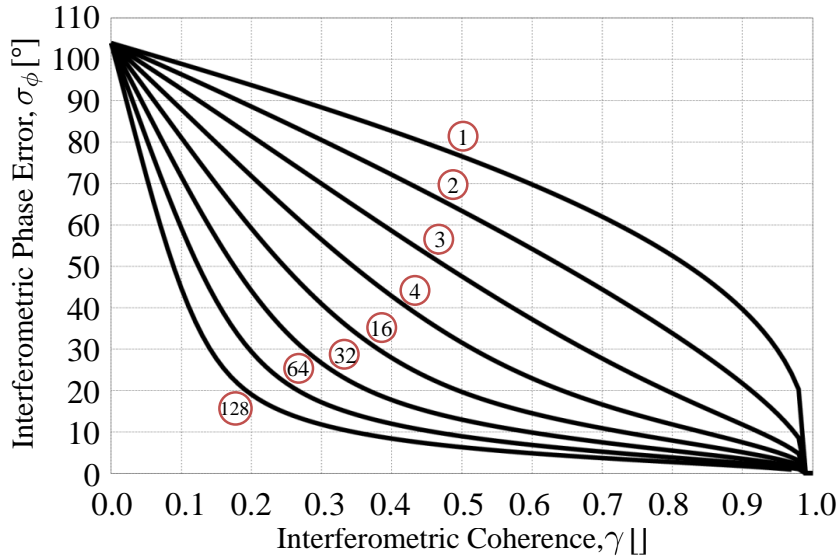
Figure 9: Standard deviation of interferometric phase error as a function of coherence, for different number of looks.

3 The Tandem-L Mission

Tandem-L is a DLR (Deutsches Zentrum für Luft- und Raumfahrt) mission proposal for a highly innovative L-Band SAR satellite mission for the observation of dynamic processes of the Earth's surface [17]. Thanks to the novel imaging techniques and a recording capacity of 8 Terabytes per day, it will provide essential information for solving scientific questions in the biosphere, cryosphere, geosphere and hydrosphere environments (Figure 10).
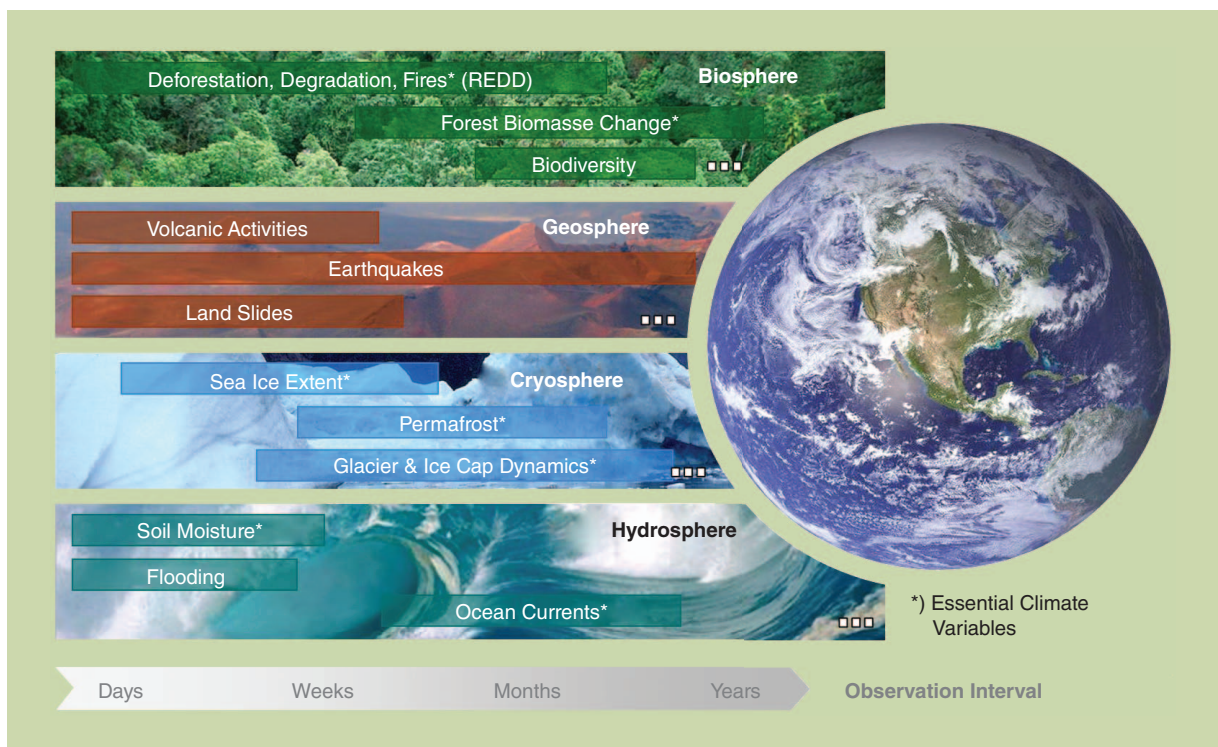
Figure 10: An overview of the Earth's dynamic processes which will be assessed and monitored by the Tandem-L mission.

3.1 Mission Goals and Characteristics

The mission consist of two L-Band (λ=23.6 cm) SAR satellites equipped with a reflector antenna employed for SAR acquisitions, with variable formation flight configurations depending on operative mode (Figure 11). A list of the mission parameters is reported in Table 1 Having as main characteristic the high degree of innovation with respect to the current technology, the systematic acquisition concept is based on two imaging modes: 1) 3-D structure mode with bistatic radar operation and 2) deformation imaging mode with differential SAR interferometry. Both the imaging modes allow to achieve the following mission objective:

1. Global measurement of 3-D forest structure and biomass, to understand the ecosystem dynamics and the carbon cycle;

2. Systematic recording of deformation of Earth's surface with millimetric accuracy for risk analysis and earthquake research;

3. Quantification of glacier movements and melting processes in polar regions for better predictions of sea level rise;

4. High resolution measurement of soil moisture for advanced water cycle research;

5. Constant observation of coastal zones and sea ice for environmental monitoring and ship routing;

6. Mapping of agricultural fields for crop and rice;

7. Infrastructure and disaster monitoring.
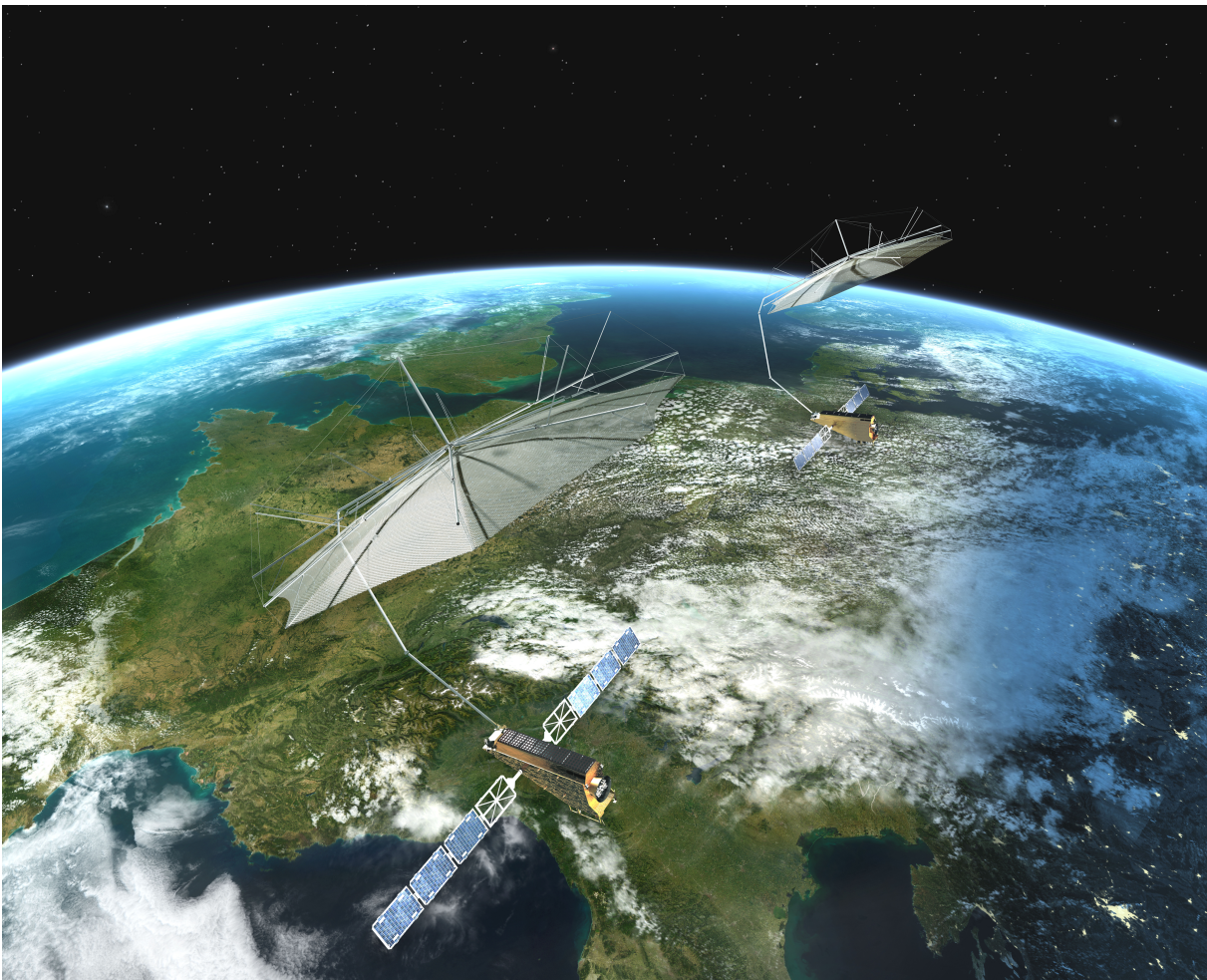
Figure 11: Artistic view of the two satellites equipped with a reflector for the Tandem-L mission.

The goal of the mission is to acquire interferometric images of a large spectrum of the global landmass once a week. An advanced downlink channel trough Laser Communication Terminal (LCT) could extend the acquisition method, allowing the monitoring of the entire landmass twice a week. Existing remote sensing mission are inadequate in terms of imaging performance and measurement resolution for correctly observe large scale processes precisely, making Tandem-L the only SAR mission able to do that. If considering the operative lifespan of the project, the opportunity for acquiring large areas with high spatial resolution within a short revisit time is fundamental also in emergency and hazard scenarios. From the original SAR data (often referred to as Level-1 product), DLR proposes a series of advanced products, with the aim of extracting relevant parameters from the original Level-1 acquisitions. At this stage, 10 application areas of products of Level-2 and 3 (so-called "high-level products"), have been defined considering the capabilities of the proposal [17]:

- **Large scale deformation:** Tandem-L configuration is suitable for monitoring terrain deformation, and in this field, five different applications are considered: *inter-seismic deformation*, *co-seismic deformation*, *tectonics for volcanoes*, *urban subsidence* and *landslides*. All of these measurements will be provided with an accuracy in the order of millimeters.

- **Global DEM:** All land surfaces will be covered twice a year in 10-meter resolution in polarimetric bistatic interferometric mode. From these acquisitions a digital elevation model and a digital terrain model will be generated, at a final resolution comparable with the actual DEM generated from the acquisitions of TanDEM-X system [10].

- **Forests:** In forest applications, Tandem-L has capabilities to provide products for estimating *forest structure*, *forest height* and *forest biomass*. Especially this last parameter is fundamental to better understand the terrestrial carbon cycle process.

- **Wetlands:** From wetlands areas it is possible to define the *wetland inundation maps* and the *pan-tropical mangrove extent*.

- **Agricultural maps**: the mapping of the *paddy rice field* at high resolution and the remaining *agricultural areas* will deliver crop calendars and crop classification maps.

- **Soil moisture:** mapping of the *spatial variability* of the soil moisture within few days (1-4) and the monitoring of the changes in large areas to provide information on spatial and temporal pattern of the soil.

- **Land ice and permafrost:** The dynamic of the processes in the Artic areas are still a case of study, whereas Tandem-L cryosphere products will contain crucial information for a better understanding of this scientific field. In particular *glacier velocity* estimation will be possible as well as the information regarding *ice structure*, *ice sheet elevation change*, *grounding line position* and *permafrost extent*.

- **Sea ice:** both *sea ice extent* and *sea ice type classification* will be available, allowing the science community to have Earth-wide information.

Parameter	Value
Orbit Height	745 km
Horizontal baselines	1 km . . . 18 km
Inclination	98.4°
Revisit time	16 days
Frequency	L band
Range bandwidth	up to 85 MHz
Azimuth resolution	1 m . . . 10 m
Swath width	50 km . . . 350 km
Downlink capacity	8 Terabytes/day
Look direction	left / right
Reflector diameter	15 m
Mission lifetime	10 years
Polarization	single/dual/quad

Table 1: Tandem-L system parameters.

- **Ocean monitoring:** A number of new products in the field of large scale hydrology will be available for the first time: *ocean currents estimation*, *wind speed velocity*, *coastal area change*, and *water level change.*

- **Emergency mode:** In case of natural disaster (e.g. flooding, fires and volcanic events) a high resolution imaging mode will provide crucial information on the affected areas.

Tandem-L mission will be capable of high resolution wide swath (HRWS) through a feed array which illuminates a reflector. Each element of the array will illuminate a different area on ground without overlapping with other beams. Scanning operation in reception is performed from near to far range, known as SCORE (SCan-OnREceive) [11], is done through a digital phase array. Tandem-L acquisition scheme is shown in Figure 12. High resolution wide swath imaging allows to achieve a swath width in the order of about 350 km, maintaining a resolution of 10 m. Considering the actual TanDEM-X mission, a resolution of 6 m is achieved under a limited swath width of 30 km. Such an increase of swath aperture with high resolution imposes severe constraints in term on data volume, on-board memory and system complexity.
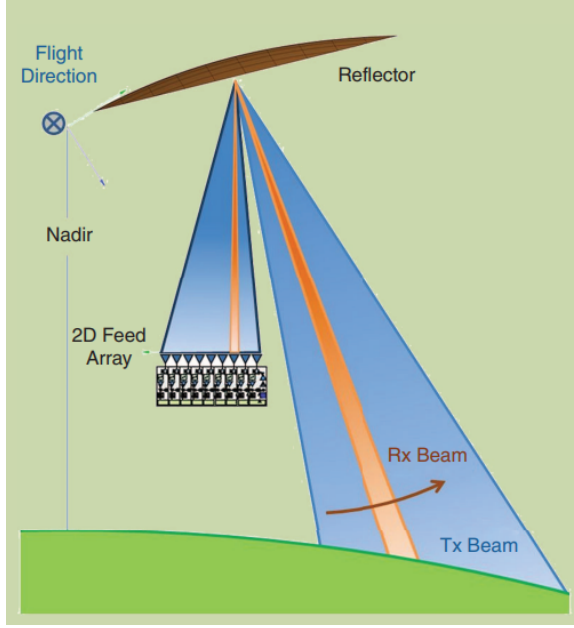
Figure 12: Tandem-L Scan-On-Receive principle.

3.2 Staggered SAR

For any SAR system, an intrinsic trade off between best attainable azimuth resolution and swath width exists. By selecting a fixed PRF for the system, in the focused image blind ranges will be observed, as shown in the left part of Figure 13. The extension of blind ranges in the slant range dimensions is equal to

$$\Delta R_{0,blind} = c_0\tau \tag{33}$$

being τ the range chirp duration. If considering that the time interval when each feed element is transmitting is in the order of microseconds, this will results in hundreds of meters in the image lost in the blind range. Moreover, their position do not change along the azimuth, making the information contained in the missing samples impossible to recover.

Staggered SAR consists in the employment of a variable PRI along the azimuth dimension. This way, it is possible to make vary the azimuth position of the gaps. In particular, by exploiting elaborated sequences of PRIs, one can impose that no more than one sample is missed in azimuth direction, as shown in the right-hand side of Figure 13). This way, the lost information can be recovered by implementing an opportune interpolation across the azimuth dimension [21][22]. To obtain the focused data, staggered SAR raw images need to be interpolated on a uniform grid, in order to properly perform the azimuth compression. This is done through a *Best Linear Unbiased* (*BLU*) interpolation, which exploits the correlation between the neighbouring azimuth samples to estimate in an optimal manner the value on the uniform grid. Estimation of missing samples must be carried out with high accuracy in order to limit the reconstruction errors, which would otherwise inevitably lead to subsequent error in the focused data. Since the *BLU* interpolation exploits the correlation in the azimuth dimension, an oversampling is necessary to narrow the time lag between two samples and hence to opportunely recover the infor-
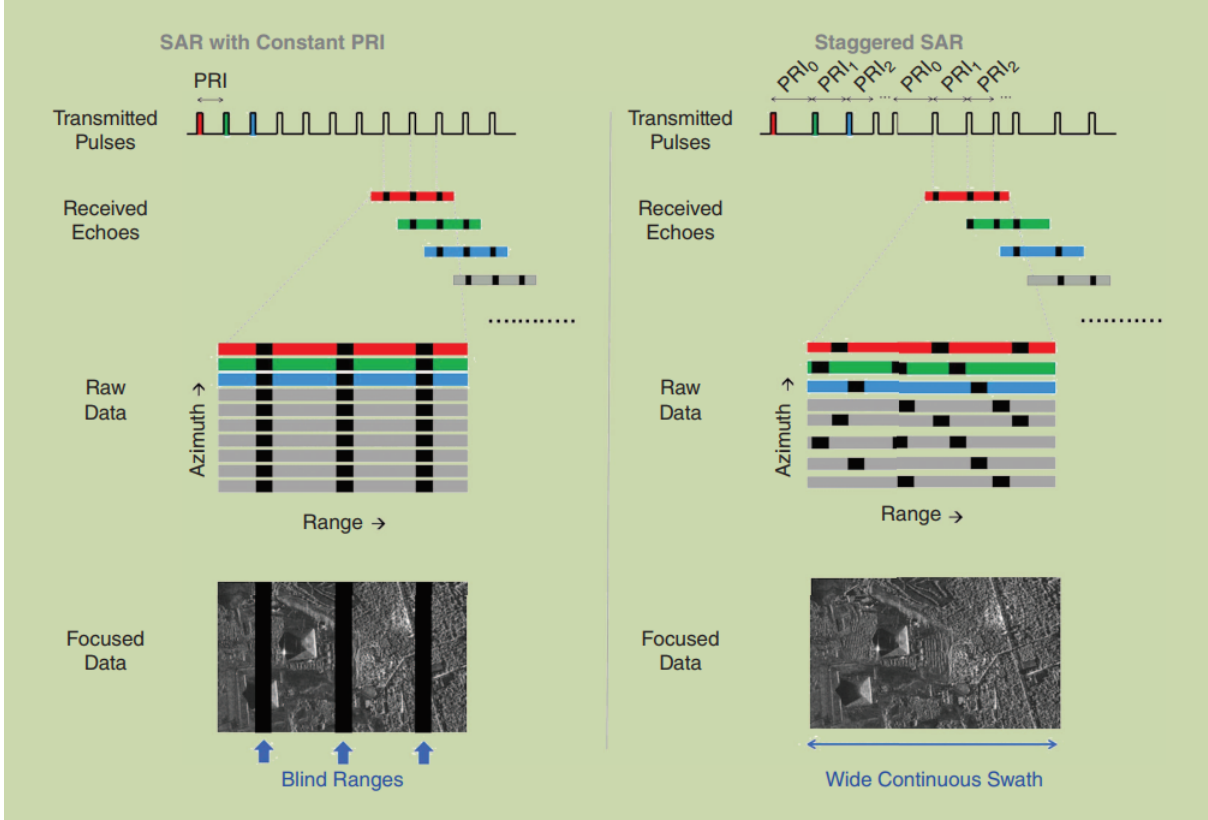
Figure 13: Location of blind ranges, (left) for a system with constant PRI and (right) staggered PRI.

mation lost in correspondence of the gaps positions. It is important to point out that such an oversampling (by means of a larger average PRF, as defined in (19)) is necessary in order to avoid the occurrence of large sidelobes in the impulse response function of the system. The oversampling leads to an increase in terms of samples in the azimuth dimension, hence a wider amount of on-board memory is required. Shannon's sampling theorem defines the sampling rate for a proper discretization of continuous processes without loss of information. The processing bandwidth employed during azimuth focusing is around 780 Hz, whereas the mean PRF of about 2700 Hz [21]. Thus, the amount of oversampling for Tandem-L case is around 250%. This means that the oversampling is not necessary to retrieve the focused data with higher accuracy, occupying valuable on board memory. On the other hand, it is not possible to discard exceeding samples without performing the required processing to retrieve the value in gaps positions. This aspect is crucial for the data reduction approach proposed in this thesis and will be discussed in detail in Section 6.3.

4   SAR Raw Data Quantization

The received SAR echo is an analog signal transduced by the antenna, which needs to be digitized in order to be stored in the digital memory. The analog-to-digital conversion (ADC) can be further decomposed in two processes: sampling (i.e. time discretization) and quantization (i.e. amplitude digitization). SAR raw data quantization is detailed in this chapter. The degree of fidelity in the digitization process is a fundamental parameter especially in SAR missions: an inaccurate quantization scheme can degrade the data and making impossible their interpretation, while a too fine quantization scheme leads to the overflow of on-board memory reducing the amount of measurement possible within a given time period. What is usually done is the employment of lossy quantization schemes as a trade-off, taking into account the introduced degradation as an acceptable loss with respect to the final product and the required performance. On-board data reduction techniques can be implemented, yet the computational complexity needs to be as low as possible to obtain high reliability and throughput while using minimal satellite resources.

4.1   Quantization Basics

In SAR systems the analog signal is usually quantized using a relatively high bitrate (e.g. 8 bits/sample) and then further data reduction operations are performed. Each quantization techniques is characterized by a fixed number of outputs, and quantization is basically implemented by mapping the amplitude of the input into the nearest possible output. The amount of possible outputs within a fixed amplitude range is defined by the number of bits used for each sample, which define the "alphabet" of the quantizer. Since binary domain is taken into account, the number of possible output values are defined as 2^{N_b}, where N_b is the number of bits assigned to each sample. The discretization process always introduces a certain error, which is maximum when a sample lies exactly in between two possible output values (i.e. on the decision threshold). This error is randomly distributed and usually referred to as quantization noise. Let us consider an analog input signal $s_x(t)$, then the quantized output from an ADC can be defined as $s_{\mathrm{adc}}(t)$. The quantization process is schematically illustrated in Figure 14, and can be seen as an amplification of the input signal by a factor A and an additive noise source, $q(t)$, which is the quantization noise. The quantization error is defined as the difference between the original signal and its quantized version $Q_i(\mathrm{x})$ as

$$q = \mathrm{x} - Q_i(\mathrm{x}) \quad \text{if} \quad \mathrm{x} \in [d_i, d_{i+1}] \tag{34}$$

where d_i represents the decision level associated to the ith quantization interval.

4.1.1   Uniform and Non-Uniform Quantization

The transfer function of the quantization process is a non-linear staircaise-like function, bounded in the maximum and minimum output values and characterized by M levels (i.e. $M = 2^{N_b}$). Depending on the arrangement of the decision levels, it is possible to
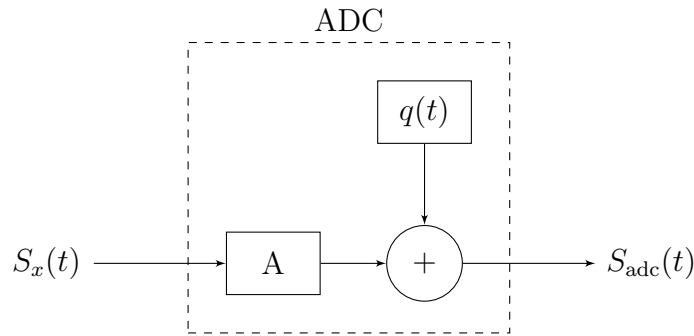
Figure 14: ADC flowchart, considered as a variable gain amplifier A and an additive noise source $q(t)$.

define the *midriser* and *midtread* quantizers, according to Figure 15 the first one (Figure 15a) has a decision threshold in 0, meaning that this value is not present in the possible output. The second one (Figure 15b) instead includes the 0 as a possible reconstruction (output) value, meaning that an input value with amplitude less than $\Delta/2$ is mapped as 0 without considering its sign.

(a) midrise quantizer

(b) midtread quantizer
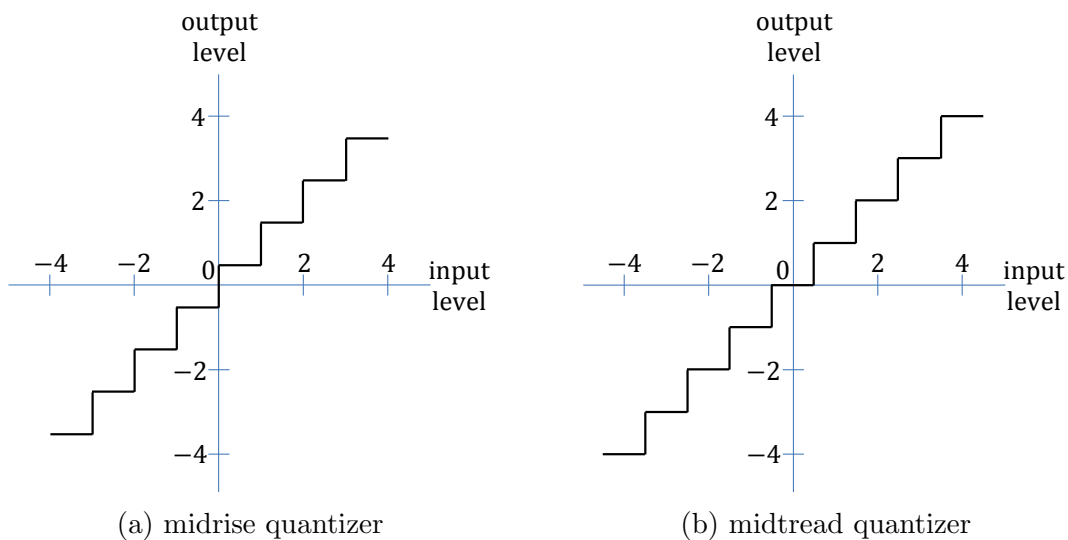
Figure 15: Midrise (left) and midtread (right) quantization schemes.

A quantizer can either be *uniform* or *non-uniform* depending on the step size Δ, which represents the portion of the input mapped in one single output value. If considering a uniformly-spaced step size, the quantizer is said to be *uniform*; on the other hand, a quantizer having a variable step size is said to be *non-uniform*. The choice to use a uniform quantizer instead of a non-uniform one comes when the input signal is *uniformly* distributed; in every other case (e.g. the signal has a normal distribution) one can optimize the distribution of the quantization decision levels in such a way that the mean square error (MSE) is minimized, and this always ends up with a non-uniform quantizer). This means that if the input statistics are known, it is possible to define the best suitable type of quantizer. Optimal quantizer design must take into account the suitable number of levels and the correct threshold arrangement. As introduced above, the characteristic of

24

the step size Δ must be choosen according to the statistics of the input signal. Let us consider an input signal x having zero mean and variance σ_x^2

$$\sigma_x^2 = E[X]^2 = \int_{-\infty}^{+\infty} x^2 p_x(x)\, \mathrm{d}x. \tag{35}$$

The quantization error Q as in (34) is also as a zero mean normal distributed random variable with variance σ_q^2.

$$\sigma_q^2 = E[Q]^2 = \int_{-\infty}^{+\infty} [x - Q_x]^2 p_x(x)\, \mathrm{d}x, \tag{36}$$

then the integration of this expression is considered in the whole span of the decision levels ($M = 2^{N_b}$), giving as result

$$\sigma_q^2 = E[Q]^2 = \sum_{k=1}^{M} \int_{k}^{k+1} [x - Q_x]^2 p_x(x)\, \mathrm{d}x. \tag{37}$$

The maximum and minimum output value of the quantizer are known as V_{clip}, which defines the boundary of the quantizer $[-V_{\text{clip}}, +V_{\text{clip}}]$. By knowing the number of levels and the boundary of operation of the quantizer, it is easy to derive the step length (i.e. the "resolution" of the quantizer) under the uniform quantizer assumption as

$$\Delta = \frac{2V_{\text{clip}}}{2^{N_b}}. \tag{38}$$

The number of decision levels is fixed to the number of bits employed in the quantization process, the V_{clip} bound instead must be selected to reduce the error. In particular, the dynamic range of the input signal and the quantizer must be as close as possible

$$|x| \leq V_{clip} = \frac{\Delta \cdot 2^{N_b}}{2}. \tag{39}$$

The probability density function of the error can be assumed to be uniformly distributed in the step size interval if this is small, giving as result

$$p_q(q) = \begin{cases} 1/\Delta & \text{if } |q| \leq \Delta/2 \\ 0 & \text{otherwise,} \end{cases} \tag{40}$$

The last equation allows to express in closed form the variance of the quantization error as

$$\sigma_q^2 = \Delta^2/12 = \sigma_x^2\, 2^{-2N_b}. \tag{41}$$

4.1.2 Block Adaptive Quantization (BAQ) for SAR Systems

A received echo is made up of both, high and low power contributions, which are generated by high and low reflectivity of the targets, respectively. Thus, the power of the raw signal is space varying. For SAR imaging such a dynamic variability is typically in the order of several decibels, meaning that, for achieving the required accuracy in SAR products, the employment of a standard, uniform ADC as it has been presented above,
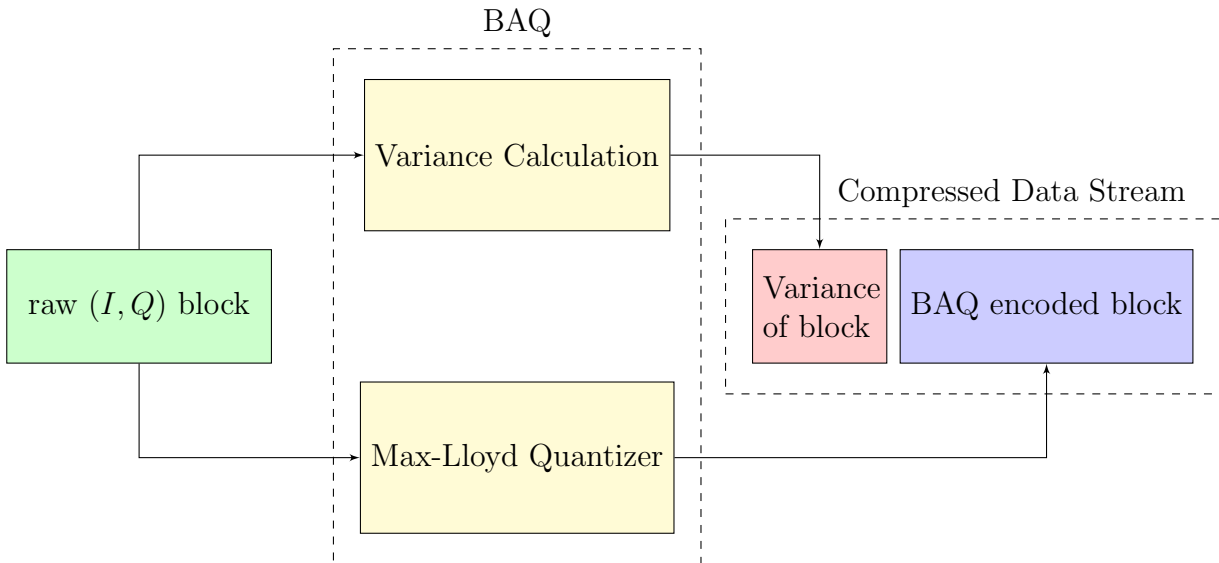
Figure 16: Block adaptive quantization (BAQ) flowchart.

is applicable only if a very large number of bits N_b is employed. This makes the use of uniform quantizers not suitable for typical spaceborne SAR systems. In this scenario, adaptive quantization is mandatory to overcome the high dynamic variability of the signal. Block Adaptive Quantization (BAQ) is a quantization scheme which allows to efficiently compress SAR raw data and it is nowadays widely used as quantization standard for spaceborne SAR systems [13][12]. By exploiting the input signal statistics, a raw data block is quantized independently from the others, making possible the quantization decision levels to be adapted to its specific dynamic. This quantization scheme is known as Max-Lloyd quantizer, adapting the quantization boundary to the normal statistics of the input signal [13][16]. This method allows for high performance in quantization, meaning that it is possible to encode more information using less memory. The compression process can be carried out both in time domain and in frequency domain. The first allows a better signal to quantization noise ratio, but it is not optimized for the compression of the spectral envelope in range and azimuth direction. Even though the second technique has higher performance, operating in frequency domain implies high complexity in hardware [3]. BAQ is usually implemented as a cartesian quantizer, meaning that the two components of the complex raw signal (I and Q) are treated separately, since the assumption of statistical independence between In-phase and Quadrature components holds (see (20)). Polar BAQ [19] has also been investigated leading to no significant gain in terms of performance. As an example, both the TerraSAR-X and TanDEM-X satellites from DLR [25] employ cartesian BAQ for on-board raw data compression. For TerraSAR-X and TanDEM-X, the input raw signal is clipped ($V_{\text{clip}} = \pm 127.5$) and then quantized at 8 bit per sample through a uniform ADC. The BAQ start with the decimal interpretation of the I and Q quantized values, as in

$$I_{adc,n} = (-1)^s \cdot \left(0.5 + \sum_{i=0}^{6} M_i \cdot 2^i \right) \qquad (42)$$

26

Compression Rate, n_{BAQ}	C	E_{max}	M_{max}
8:2	2.20374	24	1
8:3	5.28038	20	3
8:4	8.50475	16	7
8:6	15.2549	8	31

Table 2: Parameters for BAQ encoding for different compression factors as implemented in TerraSAR-X and TanDEM-X. In the first columns (Compression Rate), the 8 at each row indicates the ADC bits, and the second number is the effective n_{BAQ} employed for BAQ compression.

$$Q_{adc,n} = (-1)^s \cdot \left(0.5 + \sum_{i=0}^{6} M_i \cdot 2^i \right) \tag{43}$$

Here, n is the sample index and i the i-th bit of the ADC encoded sample, while s represent the sign bit. The decimal interpreted signal is then divided in blocks of fixed length and given as input to the BAQ. The block size is determined as a trade off between the similarity of power between the samples and the gaussian statistics within the block. This means that a block should be large enough to satisfy the gaussian assumption, but small enough to have almost constant dynamic.

BAQ encoding of an input signal in TerraSAR-X and TanDEM-X can be seen as the following sequence of steps:

1. The output of the ADC ($I_{adc,n}$ and $Q_{adc,n}$) is divided into blocks along the range line. The chosen length for each block is $L_{BAQ} = 128$ samples.

2. Depending on the compression rate (n_{BAQ}) in charge, the corresponding C value is selected from Table 2.

3. The exponent E_1 is calculated as

$$E_1 = 4 \cdot \log_2 \left(1 + \frac{1}{L_{BAQ}} \sum_{n=1}^{L_{BAQ}} \left(|I_{adc,n}| + |Q_{adc,n}| \right) \right) - C, \tag{44}$$

which is strictly related to the corresponding block.

4. The exponent value E_1 is compared with the E_{max} value in Table 2, giving the final exponent E as the minimum between E_{max} and E_1 rounded to the closest integer lower or equal to it

$$E = \min \left\{ E_{max}, \lfloor E_1 \rfloor \right\}. \tag{45}$$

The exponent E is stored and transmitted on ground together with the data stream (see 7.).

5. With the retrieved E value, the raw samples $I_{adc,n}$ and $Q_{adc,n}$ are scaled to $\bar{I}_n$ and $\bar{Q}_n$

$$\bar{I}_n = \frac{I_{adc,n}}{2^{E/4}} \qquad \text{and} \qquad \bar{Q}_n = \frac{Q_{adc,n}}{2^{E/4}} \tag{46}$$

27

6. Whether the absolute value from a sample exceeds the M_{max} limit, it is bounded to that. The result from this operation is defined as

$$I_{BAQ,n} = \frac{\bar{I}_n}{|\bar{I}_n|} \cdot \min\left\{|I_n|, M_{max}\right\} \quad \text{and} \quad Q_{BAQ,n} = \frac{\bar{Q}_n}{|\bar{Q}_n|} \cdot \min\left\{|Q_n|, M_{max}\right\} \quad (47)$$

7. The resulting value (mantissa) is finally uniformly quantized between $[-M_{max} - 0.5, \; M_{max} + 0.5]$ employing n_{BAQ} bits per sample.

The quantized block (mantissa and exponent) is then stored on board and then transmitted on ground through the downlink channel. In decoding, the original value is reconstructed just by applying

$$I_{BAQ,n} = (-1)^s \cdot \left(0.5 + \sum_{i=0}^{n_{BAQ}-2} K_i \cdot 2^i\right) \cdot 2^{E/4}, \quad (48)$$

where s is the sign bit, and K_i the value of the i-th bit (0 or 1). The quadrature phase is retrieved in the same manner.

4.1.3 Quantization Parameters
In order to describe a quantizer some key parameters have to be taken into account which are detailed below.
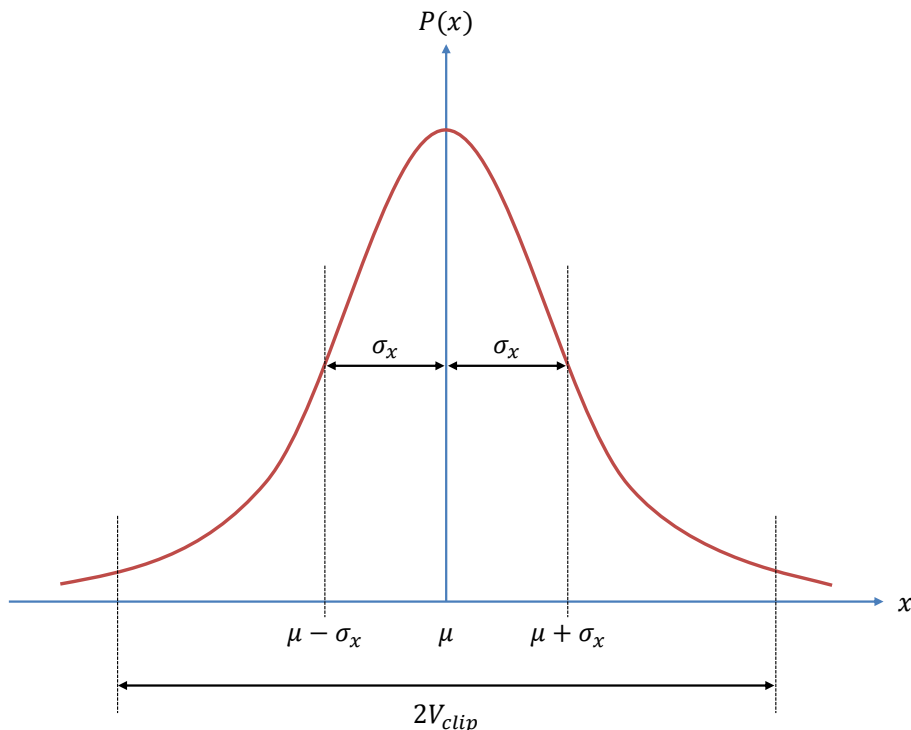
Figure 17: Probability density function of input signal and clipping threshold.

Signal-to-Clipping Ratio, $\gamma_{\mathbf{clip}}$

It is the measure of relationship of the clipping and the input signal variance. It is important in performance comparison between different types of quantizers, and is defined as

$$\gamma_{\text{clip}} = \frac{\sigma_{\text{x}}}{V_{\text{clip}}}, \tag{49}$$

where σ_x is the standard deviation of the input signal and V_{clip} the clipping voltage, as depicted in Figure 17. If considering that the input signal is complex and assuming that the standard deviation of the two components is the same, it follows that

$$\gamma_{\text{clip}} = \frac{\sqrt{\sigma_{\text{in}I}^2 + \sigma_{\text{in}Q}^2}}{V_{\text{clip}}} = \sqrt{2} \cdot \frac{\sigma_{\text{in}I}}{V_{\text{clip}}}. \tag{50}$$

When performance evaluation is taken into account, the γ_{clip} value is forced to be the same for all the considered quantizers. This is done by choosing a fixed value of γ_{clip} and adapting the input signal dynamic to that. The α parameter is the multiplication factor that allows the scaling of the input signal and can be derived as

$$\alpha = \frac{\gamma_{\text{clip}} \cdot V_{\text{clip}}}{\sqrt{2} \cdot \sigma_{\text{in}I}}. \tag{51}$$

Signal-to-Quantization Noise Ratio (SQNR)

The signal-to-quantization noise ratio is the ratio between the signal and the introduced quantization error. For real signals it can be expressed as

$$\text{SQNR} = \frac{\sigma_x^2}{\sigma_q^2}. \tag{52}$$

If a complex signal is considered, the SQNR can be calculated for real and imaginary part separately with (52), or by considering (53), where the sum on the available pixels of the square absolute is considered.

$$\text{SQNR} = \frac{\sum_{i=1}^{N} |x_i|^2}{\sum_{i=1}^{N} |q_i|^2} \tag{53}$$

In the upper equation i represent the index of the samples, x is the non quantized data while q is the difference between the original data and the quantized data. As previously introduced in (41), the variance of the quantization error varies with the number of bits employed in quantization. Substituting (41) in (52) and performing an evaluation in dB for an optimum ADC quantizer, we obtain

$$\text{SQNR}_{\text{dB}} = 10 \cdot \log_{10} 2^{2N_b} \approx 6 \cdot N_b \text{ dB} \tag{54}$$

which shows that, for each bit per sample added for quantization, a gain of approximately 6 dB in terms of SQNR is obtained, which is a well known result from rate-distortion theory [7].

Quantization Coherence, γ_{quant}

As previously introduced in 2.4.2, the coherence in the interferometric acquisitions is also dependant on the quantization. In order to express the γ_{quant} value, only the SQNR is necessary, since it is a very informative measure on the quantization impact. The quantization coherence can be expressed as

$$\gamma_{quant} = \frac{1}{1 + \frac{1}{\text{SQNR}}} = \frac{\text{SQNR}}{1 + \text{SQNR}}. \tag{55}$$

4.2 Quantization Errors in SAR

As discussed above, quantization process introduces errors, which can be measured in terms of SQNR. Both intrinsic characteristics of a cartesian quantizer (I and Q components treated separately) and clipping operation are cause of errors of different types and effects. Thus, *granular* and *clipping* errors are due to the quantization operation, while the *low scatterer suppression* is an error which occurs in synthetic aperture radar acquisitions.

4.2.1 Granular and Clipping Errors

Being the dynamic range of the quantizer limited by V_{clip} (Figure 17), for a fixed number of bits per sample, the granular error is considered as the quantization error within the decision threshold. As introduced before, the error within the decision threshold is maximum when the sample lies on the threshold. If the dynamic range is increased with respect to the input power (i.e. by reducing γ_{clip} or equivalently enlarging V_{clip}), the decision threshold will be wider, meaning that the granular noise will be greater. On the other hand, shrinking too much the V_{clip} to avoid high granular error will exclude a wide part of the PDF of the input signal from the quantization space. All the samples laying outside the interval $[-V_{\text{clip}}, +V_{\text{clip}}]$ will be coded as the maximum value available in the quantization space, introducing clipping (or overhead) errors. The standard deviation of the granular error can be expressed as

$$\sigma_{E_g} = \sum_{i=1}^{N} \int_{y_i-\Delta/2}^{y_i+\Delta/2} (x - y_i)^2 f(x) \mathrm{d}x, \tag{56}$$

considering N reconstruction levels defined as y_i with $i = 1 \dots N$. In the same way, it is possible to define the standard deviation of the clipping error integrating the PDF of the input signal outside the quantization boundary, leading to

$$\sigma_{E_c} = \int_{-\infty}^{y_1-\Delta/2} (x - y_1)^2 f(x) \mathrm{d}x + \int_{y_1-\Delta/2}^{+\infty} (x - y_N)^2 f(x) \mathrm{d}x. \tag{57}$$

It is clear that a correct choice of the quantizer dynamic with respect to the input signal is a key element in order to design a well-operating quantizer. The relationship between these two error contributions can be seen in Figure 18, which is the result of a Monte Carlo simulation representing the SQNR of a uniform quantizer at different values of γ_{clip} and different bitrates. The left part of the graphs shows a decreasing value of SQNR as γ_{clip} decreases, describing the granular error. The effect of the clipping error is noticeable

30
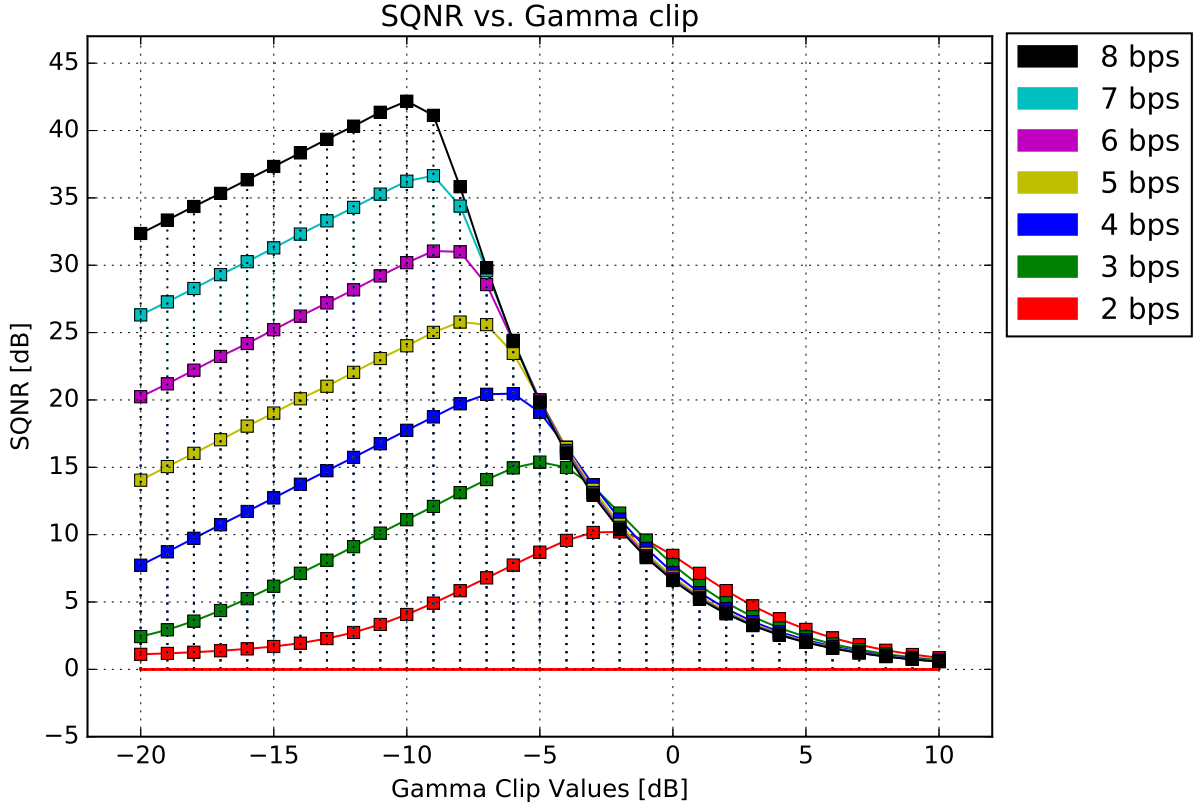
Figure 18: Monte Carlo simulation showing the SQNR performance of a uniform ADC for different bitrates and different values of signal-to-clipping ratio (γ_{clip}).

with values of γ_{clip} greater than -10 dB, and the error contribution has more impact. From that it is possible to select the best γ_{clip} value at -10 dB, giving this value the best trade off between the two errors. It is important to recall that for real applications it is better to adapt the γ_{clip} to a value lower than -10 dB in order to further reduce the occurrence of clipping errors (which most affect the performance) at a cost of a slight increase of granular errors.

4.2.2   Low Amplitude and Low Scatterer Suppression

Cartesian quantizers introduce granular and clipping error depending on the selected quantization space. If phase errors due to quantization are considered, one can notice that they strongly depend on the corresponding signal amplitude. In particular, the phase error is bounded to a maximum of 45°, according to

$$|\Delta_\phi|_{max} = \frac{|\theta_{x_a,y_a} - \theta_{x_b,y_b}|}{2}. \tag{58}$$

Such a high phase error is present in the nearest quadrants of the quantization space, as pictured in Figure 19. Green vectors represent two possible raw signal values, while the black vectors represent the quantized version to the nearest possible output between the decision boundaries. It is possible to notice that the same amount of granular error is present (i.e. the quantization steps is the same for both signals), while the phase error is larger for the sample with lower amplitude. Having less sensitivity near the 0

31
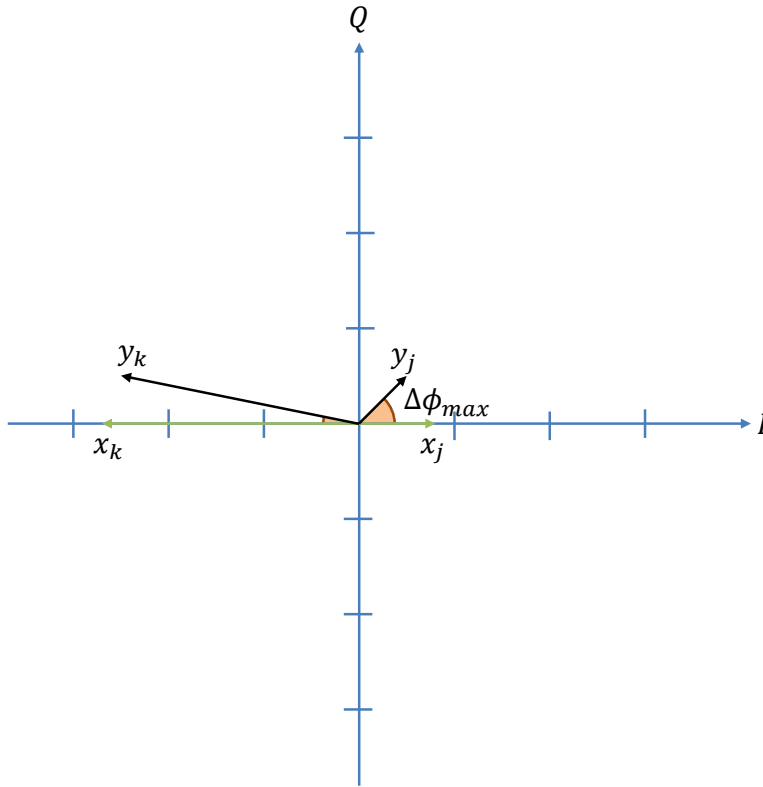
Figure 19: Phase error in cartesian quantizers for low and large amplitude signals. Green vectors represent two possible raw signal values, while the black vectors represent the quantized version to the nearest possible output between the decision boundaries. The resulting phase is more degraded for the sample with lower amplitude.

value imposes that the phase of low backscattered targets will be much more imprecise, lowering the performance of phase-based techniques such as interferometry. Beside that, low backscatter areas are also affected from the so called low scatterer suppression [6][15]. This phenomena is due to the relationship between the beamwidth extension, expressed by the synthetic aperture, the chirp length and the distance between two (or more) targets within the scene. If such a distange is much smaller than the synthetic aperture of the antenna and the chirp length respectively, high reflective targets overlap their response on low scatterers. BAQ adapts the quantization dynamic to the statistics of the signal, therefore, if the two overlapping targets have different magnitude responses, the strong signal is better reconstructed, whereas the low one is heavily distorted. In Section 6.3 an application in a simulated scenario showing low scatterer suppression effects will be presented.

5 Predictive Quantization for SAR Systems

On-board memory represents a critical resource for spaceborne SAR systems since satellite platforms can not be upgraded during their lifetime. Different on-board compression techniques for SAR systems have been presented in the literature [16],[19], aiming at exploiting the intrinsic correlation patterns between samples to reduce the amount of data. The capability to encode a higher amount of information is challenging when measurements must be sent on ground. Linear Predictive Coding (LPC) has been introduced in the late 60's and applied in the field of speech encoding, where data troughput of early communication systems was a limiting factor. This technique is the joint operation of a predictor and a quantizer, reconstructing the original signal performing the reverse process in reception.

5.1 Linear Predictive Coding

SAR system application scenarios impose severe constraints: on-board compression techniques need to be relatively simple from the complexity and computational point of view, on the other hand the highest compression performance should be achieved. High performance and complex techniques for data reduction field are not applicable for spaceborne SAR, where on-board electric power is not available in large quantity. If considering a discrete time signal, the encoding is normally done sample by sample (or on block of samples, as implemented by the BAQ, see Section 4.1.2), associating to each amplitude value a digital number according to discretization levels. This operation is the simplest encoding system and is known in communication systems as Pulse Code Modulation (PCM). Increasing the complexity, it is possible to consider the Differential Pulse Code Modulation (DPCM), which introduces the concept of *differential coding*. This means that the to-be-quantized signal for a sample $s[\mathrm{n}]$ will be then the difference between $s[\mathrm{n}]$ and the previous sample $s[\mathrm{n}-1]$.

$$s_d[\mathrm{n}] = s[\mathrm{n}] - s[\mathrm{n}-1] \tag{59}$$

The process is reversed in reception, which allows to reconstruct a distorted version (since the quantization is a lossy process) the original values. DPCM reduces the dynamic of the signal if the assumption that a sample is similar (i.e. correlated) to its previous it is in charge (i.e. the signal should not vary too much between two samples). In order to increase the performance of differential coding, Linear Predictive Coding (LPC) [7] is considered. The idea of this technique is to encode the difference of one sample and its prediction. By having a-priori information on the signal statistics a proper estimation of its behaviour design of the predictor can be implemented. The prediction process is a linear combination of the N preceeding samples, where N defines the *order* of the predictor. Considering $\tilde{s}[\mathrm{n}]$ the prediction from N previous samples, it can be expressed as

$$\tilde{s}[\text{n}] = \sum_{i=1}^{N} \beta_i \left(s[\text{n} - i] + e[\text{n} - i] \right), \tag{60}$$

where the β_i values are the *weights* assigned to each i-th previous sample and $e[\text{n} - i]$ represent the quantization error on the i-th previous sample. Being the prediction process a linear combination, the complexity remains in principle sustainable for an on-board implementation. Together with the prediction process, a quantizer is employed to discretize the difference between the sample and the prediction. The dynamic of the resulting difference is lower with respect to DPCM, making this technique a good compromise between complexity and performance. The encoding process for the n-th sample is pictured in Figure 20.
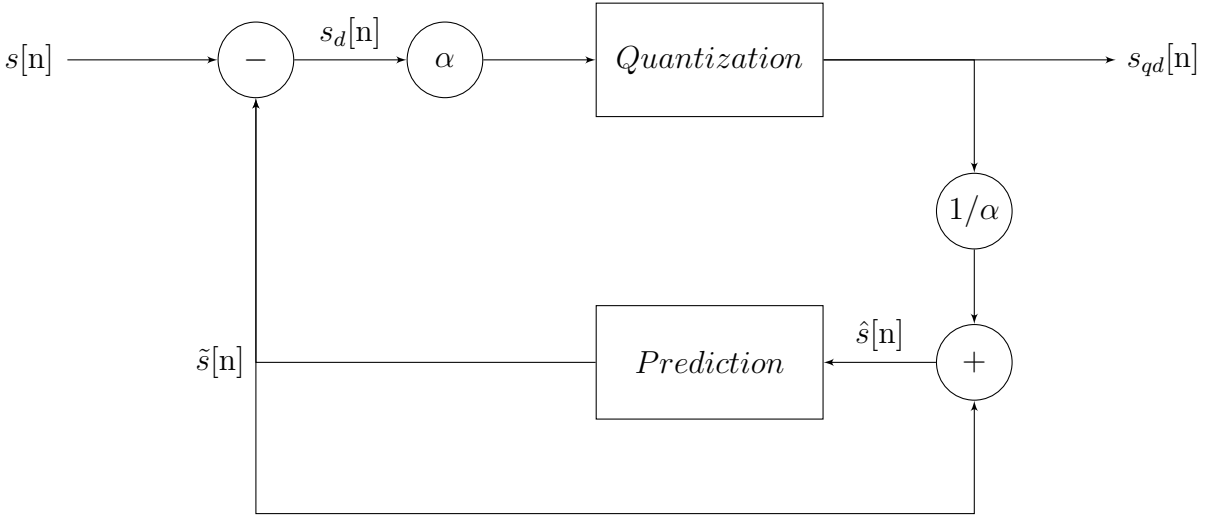
Figure 20: Predictive quantization encoding flow scheme.

In the figure above, it is possible to identify the input sample $s[\text{n}]$ from which its prediction $\tilde{s}[\text{n}]$ is subtracted, giving as result the prediction difference, pictured as $s_d[\text{n}]$. The α scaling comes from (51) and is a key parameter for the overall performance analysis, since it scales the signal to the desired dynamic (γ_{clip}) and hence allows for a fair comparison among different quantization schemes. After the quantization process, the resulting quantized difference, named $s_{qd}[\text{n}]$ is transmitted on ground and exploited to predict the subsequent sample. The dynamic of $s_{qd}[\text{n}]$ is scaled after the multiplication with α, thus it needs to be rescaled to the original dynamic of $s[\text{n}]$, since the subtraction process must be coherent. The prediction block operates as defined in (60), by weighting the N previous samples with the corresponding β. The recursive inclusion of $\tilde{s}[\text{n}]$ in the summation on the right-hand side of Figure 20, before the prediction block allows for proper reconstruction of the original signal to be fed in the prediction block. For correctly retrieving the previous sample necessary in the prediction stage from $s_{qd}[\text{n}]$, the previous prediction $\tilde{s}[\text{n} - 1]$ is added to it. Thus, the role of the recursion is to correctly represent the previous sample. It is possible to substitute (60) in (59) and performing an expansion

evaluation for two discrete time instances

$$s_{qd}[\text{n}] = s[\text{n}] - \tilde{s}[\text{n}] = s[\text{n}] - \mathfrak{P}\left\{\frac{s_{qd}[\text{n}-1]}{\alpha} + \tilde{s}[\text{n}-1]\right\}. \tag{61}$$

The previous equation shows that the recursive process takes into account all the previous predictions. $\mathfrak{P}$ represent the prediction block, i.e. the signal in the parenthesis is reconstructed by means, in turn, of the linear combination of the N previous samples.

In reception the prediction process is replicated identically, as shown in Figure 21. Here the input signal is decoded from the quantization operation, and rescaled to the original dynamic of $s[\text{n}]$ by means of a division by the same α coefficient. The resulting difference is added to the prediction generated from the identical prediction block employed for encoding in transmission.
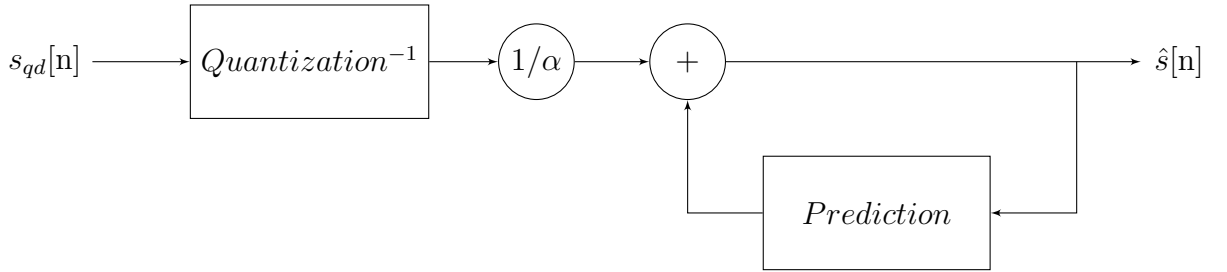
Figure 21: Predictive quantization decoding flow scheme.

The quantization error is injected in the prediction during the transmission process since it is the quantized difference that is used for the prediction. Considering the real (i.e., not quantized) difference $s_d[\text{n}]$ instead of $s_{qd}[\text{n}]$ will remove the quantization error in the prediction, but in decoding stage it will be impossible to revert the process since only the quantized version of the difference is available. $\hat{s}[\text{n}]$ is the reconstructed value of $s[\text{n}]$ with higher accuracy with respect to an ADC with the same number of bits.

5.1.1 Weights derivation

Weights definition is done during the design stage, since they will be stored onboard in registers and recalled by the predictor every time a new estimation is done. In order to minimize the standard deviation of $s_d[\text{n}]$ (i.e. the signal dynamic), it is necessary to define the best set of weights which allow to minimize the resulting error between the original and the predicted signal. The variance of the difference signal is known as

$$\begin{aligned}\sigma_d^2 &= E\left[s_d^2[\text{n}]\right] = E\left[(s[\text{n}] - \tilde{s}[\text{n}])^2\right]\\ &= E\left[\left(s[\text{n}] - \sum_{i=1}^{N}\beta_i \cdot s[\text{n}-i] - \sum_{i=1}^{N}\beta_i \cdot e[\text{n}-i]\right)^2\right],\end{aligned} \tag{62}$$

where $e[\text{n}-i]$ is the error contribution from the quantizer and is also weighted by the corresponding β_i. The minimization process aims at minimizing the Mean Square Errorr (MMSE), as it is possible to notice in (62). Thus, the next step is to minimize the variance of the difference signal by performing a differentiation (63), considering β_j with $1 \leq j \leq N$

a set of weights that optimize the MSE [7].

$$\frac{d\sigma_d^2}{d\beta_j} = -2E\left[s[\mathrm{n}] - \sum_{i=1}^{N}\beta_i(s[\mathrm{n}-i]+e[\mathrm{n}-i])\cdot(s[\mathrm{n}-j]+e[\mathrm{n}-j])\right] \stackrel{!}{=} 0 \qquad (63)$$

The upper equation can be rewritten in a much compact form, defined as

$$E\left[(s[\mathrm{n}]-\tilde{s}[\mathrm{n}])\,\hat{s}[\mathrm{n}-j]\right] = E\left[s_d[\mathrm{n}]\cdot\hat{s}[\mathrm{n}-j]\right] = 0, \;\; 1 \le j \le N. \qquad (64)$$

By expanding (64) and substituting (60), the solution can be simplified to (65), by considering that the error $e[\mathrm{n}]$ is uncorrelated to $s[\mathrm{n}]$.

$$\phi[j] = \sum_{i=1}^{N}\beta_i\left(\phi[j-k]+\sigma_e^2\delta[j-i]\right), \;\; 1 \le j \le N \qquad (65)$$

where $\phi[j]$ is the autocorrelation of $s[\mathrm{n}]$, defined for each discrete time unit as

$$\rho[j] = \frac{\phi[j]}{\sigma_x^2} = \sum_{i=1}^{N}\beta_i\left(\rho[j-k]+\frac{\sigma_e^2}{\sigma_x^2}\delta[j-i]\right), \;\; 1 \le j \le N. \qquad (66)$$

Equation (66) can be rewritten in matricial form as

$$\boldsymbol{\rho} = \boldsymbol{C\beta} \qquad (67)$$

where the matrices ρ, C and β are defined as

$$\boldsymbol{\rho} = \begin{bmatrix} \rho[1] \\ \rho[2] \\ \rho[3] \\ \vdots \\ \rho[N] \end{bmatrix}, \boldsymbol{\beta} = \begin{bmatrix} \beta[1] \\ \beta[2] \\ \beta[3] \\ \vdots \\ \beta[N] \end{bmatrix}, \boldsymbol{C} = \begin{bmatrix} 1+\frac{1}{\mathrm{SNR}} & \rho[1] & \rho[2] & \cdots & \rho[N-1] \\ \rho[1] & 1+\frac{1}{\mathrm{SNR}} & \rho[1] & \cdots & \rho[N-2] \\ \rho[2] & \rho[1] & 1+\frac{1}{\mathrm{SNR}} & \cdots & \rho[N-3] \\ \vdots & \vdots & \vdots & \ddots & \vdots \\ \rho[N-1] & \rho[N-2] & \rho[N-3] & \cdots & 1+\frac{1}{\mathrm{SNR}} \end{bmatrix}. \;(68)$$

The ρ vector represents the correlation values between the sample to be estimated and the samples used for the prediction, while the β vector is composed of the prediction weights. Finally, the matrix C takes into account the relationship between the samples used in the prediction, they are also correlated between them. The SNR value on the diagonal depends on the performance of the quantizer, which also depends on the quality of the estimation. Being difficult to define the real impact of SNR in weight calculations, it is possible to neglect it, i.e. to se it equal to ∞. This simplification has also been verified by means of Monte Carlo simulations showing no considerable impact on the $\boldsymbol{C}$ matrix as

$$\boldsymbol{C} = \begin{bmatrix} 1 & \rho[1] & \rho[2] & \cdots & \rho[N-1] \\ \rho[1] & 1 & \rho[1] & \cdots & \rho[N-2] \\ \rho[2] & \rho[1] & 1 & \cdots & \rho[N-3] \\ \vdots & \vdots & \vdots & \ddots & \vdots \\ \rho[N-1] & \rho[N-2] & \rho[N-3] & \cdots & 1 \end{bmatrix}. \tag{69}$$

Hence, by knowing the autocorrelation of the input signal (i.e. the correlation between samples), it is possible to derive the weights from (67), as

$$\boldsymbol{\beta} = \boldsymbol{C}^{-1}\boldsymbol{\rho}. \tag{70}$$

5.2 The Tandem-L System: Autocorrelation Analysis

As briefly introduced in Section 3.2, Tandem-L mission will inevitably introduce an over-sampling along the azimuth dimension (by a factor of about 250% with respect to the final processed bandwidth B_d=780 Hz). In order to exploit this important feature to perform data reduction, the autocorrelation of raw data is investigated. Although the mission will employ a reflector antenna, in this thesis we have considered the antenna as a planar array with azimuth length L=10 m, which allows for a well approximation for the estimation of the antenna pattern. The simulated backscatter SAR data along the azimuth domain is considered as a normal distributed random process function of the antenna pattern both in transmission and in reception. Thus, the square of the antenna pattern is taken into account. The normal distributed random process is a well approximation for a distributed target, and is defined as a complex circular process with mean equal to zero and variance equal to σ^2. Complex circularity is translated in a separated generation of the process for real and imaginary part, since they can be considered independent random variables. The raw data in the azimuth dimension can be then defined as

$$r = |G(\Phi_{az})|^2 e^{-4\pi j \frac{R}{\lambda}} * s \qquad \text{where} \qquad \begin{array}{l} \Re\{s\} \sim \mathcal{N}(0, \sigma^2) \\ \Im\{s\} \sim \mathcal{N}(0, \sigma^2). \end{array} \tag{71}$$

In the upper equation $G(\Phi_{az})$ is the antenna pattern defined in (4) and depicted in Figure 22. It has been calculated considering an antenna length of 10 m, while the complex exponent represent the doppler history of the echo, calculated considering a wavelength λ equal to 23 cm (Tandem-L carrier frequency $f_0 = c/\lambda =$1.2 GHz). In order to evaluate the impact of the oversampling, the autocorrelation function of the raw data is considered. Considering (71), the autocorrelation can be expressed as the inverse Fourier transform of the power spectral density of the raw data (72), and defined as ρ_τ where f is the Doppler frequency, L is the azimuth antenna length and v_s is the satellite velocity (defined in Section 2.1.1), whereas τ defines the time delay between the two functions.

$$\rho_\tau = \mathfrak{F}^{-1}\left\{ \sin^4\left(\pi\frac{L}{2v_s}f\right) \Big/ \left(\pi\frac{L}{2v_s}f\right)^4 \right\}. \tag{72}$$
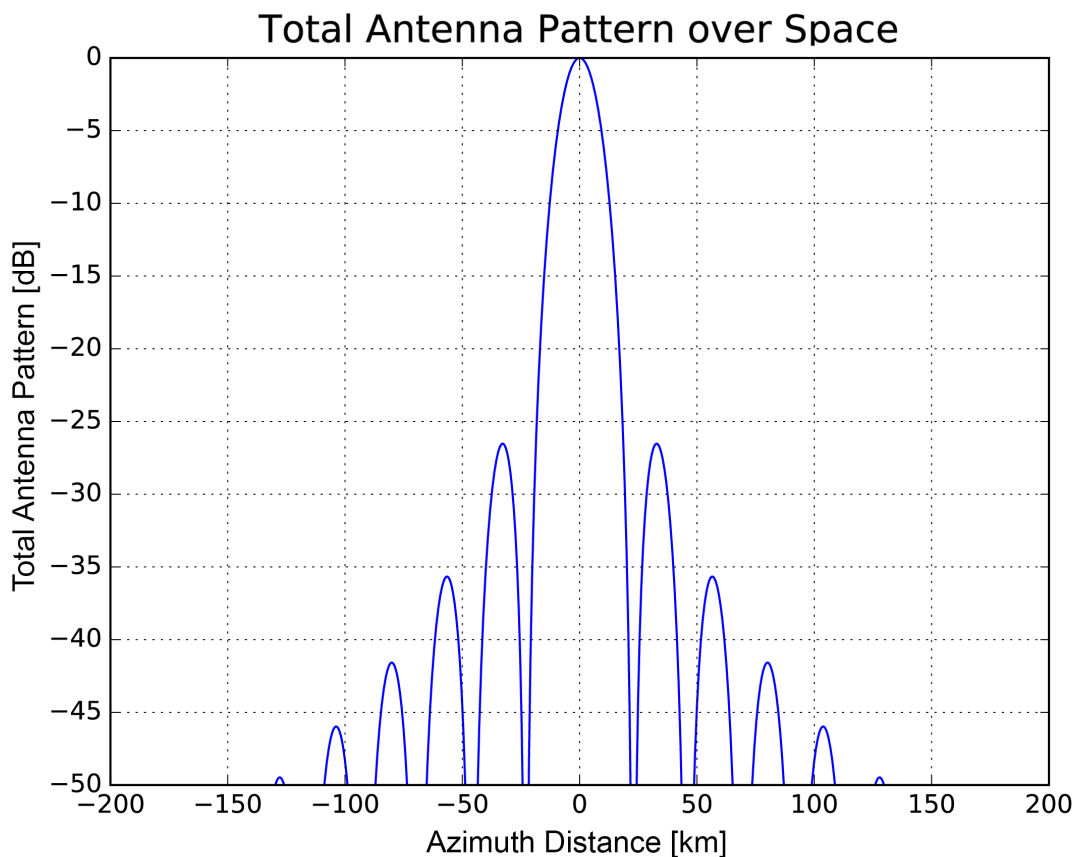
Figure 22: Azimuth antenna pattern as function of azimuth distance considering the Tandem-L system characteristics.

Performing separately the inverse Fourier transform for each sinc^2, the result is a convolution between two triangular functions in time domain, being the triangular function the inverse Fourier transform of a sinc^2 pattern [2][21]. By calculating the convolution according to (11), the result can be expressed as

$$\rho_\tau = \begin{cases} \dfrac{1}{2}(\tau^3) - 3\tau + 2) + \dfrac{1}{4}\tau(\tau^2 - 6\tau + 6) & 0 < \tau < B_w \\[2ex] -\dfrac{1}{4}(\tau - 2)^3 & B_w < \tau < 2B_w \\[2ex] 0 & \text{elsewhere.} \end{cases} \tag{73}$$

In (73), B_w is the bandwidth of the sinc^2 function and is defined as

$$B_w = \frac{L}{2v_s}, \tag{74}$$

being L the antenna length and v_s the speed of the satellite. From this equation it is clear that the higher the bandwidth, the lower the decrease of the autocorrelation function. A larger antenna gives a more directive beam, which can be intended as a narrower low-pass filter in the Doppler domain. In the same manner, a slower satellite speed gives a

higher correlation if we consider that a larger number of azimuth samples will be recorded. Figure 23a shows a graphical representation of (73), in which is possible to see that the greater the time shift, the lower the autocorrelation value. The retrieved theoretical result has been confirmed also by calculating the autocorrelation of a simulated azimuth line, showing the identical behaviour of Figure 23a. Considering as a time shift unit the PRI, which represent the SAR sampling period, the autocorrelation function has been consider as function of the PRF (Figure 23b). This second representation describes the autocorrelation between two subsequent samples at a given PRF, known as ρ_1. It is interesting to notice that the $\overline{\mathrm{PRF}}$ of Tandem-L mission equals to 2700 Hz shows to have an autocorrelation value ρ_1 greater than 0.6. If oversampling was not be present (e.g. PRF$\sim$1000 Hz), the autocorrelation value will be significantly lower. From this, it is understandable that in the Tandem-L specific scenario it is possible to take advantage of azimuth correlation between samples for reducing the signal and ultimately to achieve effective data reduction. The theoretical derivation for ρ_1 in Figure 23b can be also applied for retrieving the correlation between non subsequent samples. Considering a time lag of PRI for every sample, the correlation for second, third and other samples can be retrieved in the same manner. An example for different values of PRF can be seen in Figure 24, where the autocorrelations curves up to 6 PRI distance are plotted. Considering the typical Tandem-L PRF, it is possible to observe that the correlation is not negligible up to the third sample, while from the fourth is still equal to zero. As logical, the higher the sampling frequency (PRF), the higher the correlation between samples.
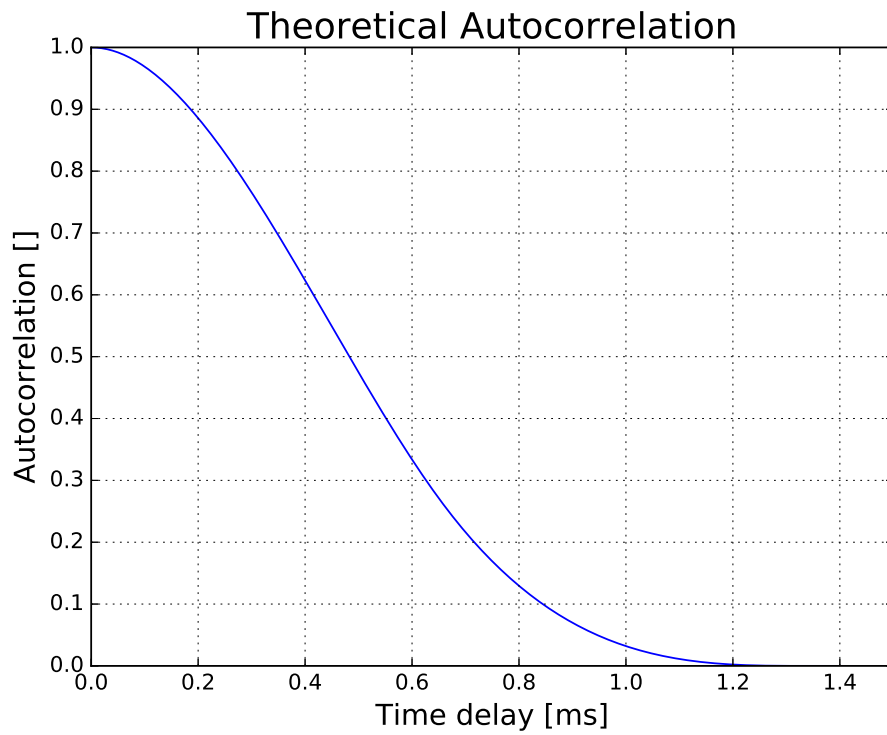
(a)
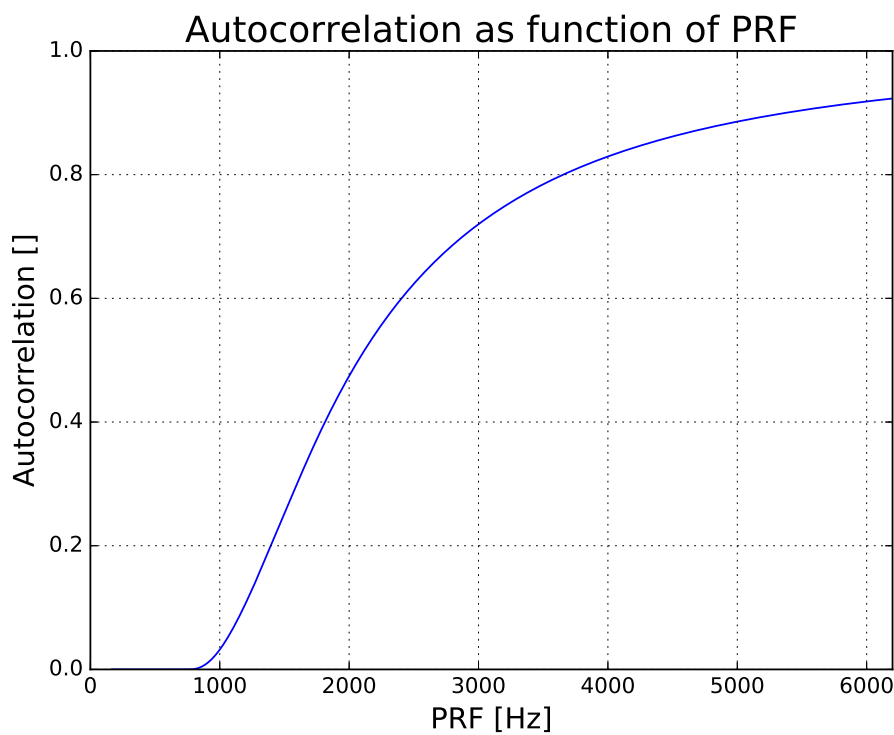
(b)

Figure 23: Theoretical autocorrelation of raw SAR data as function of time shift (a) and PRF (b).
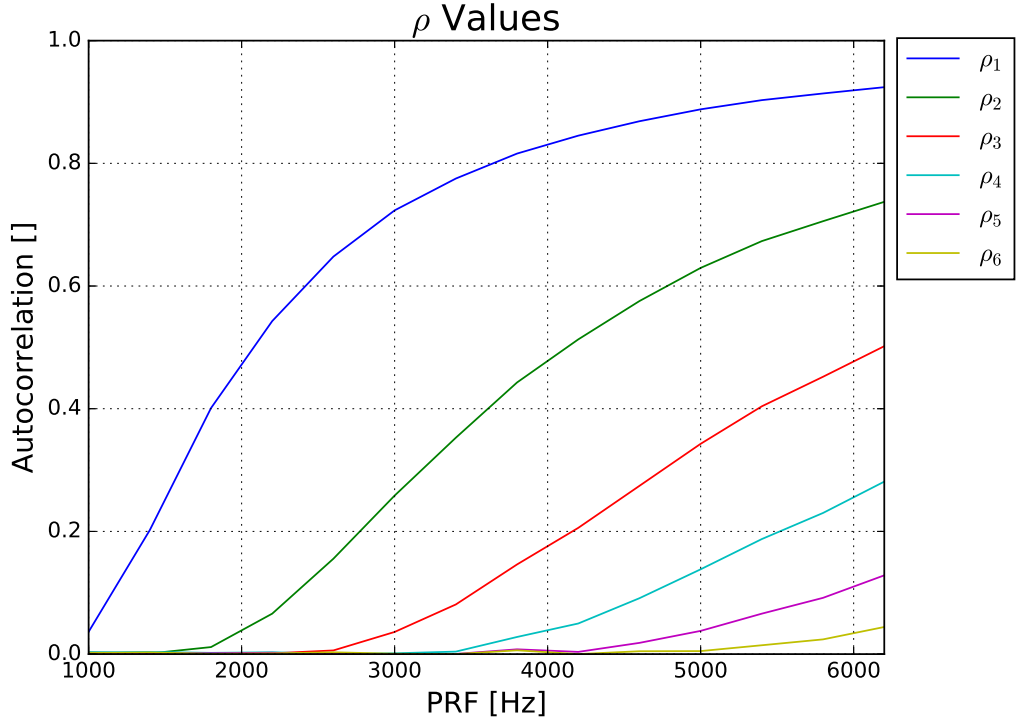
Figure 24: Autocorrelation up to 6 samples (i.e. PRI intervals) as function of PRF.

5.3   Coding Gain

Linear Predictive Coding introduces complexity in the system, but on the other hand introduces also a gain in terms of quantization performance. The discretization of gain can be expressed as the ratio between the dynamic of the input signal (s) and the prediction difference (s_d) (77). Further theoretical analyses exploiting the statistics of the input signal are reported in Section 5.3.1. The Signal-to-Noise ratio of the LPC system can be expressed as the ratio between the signal power and the power of the introduced error

$$SNR = \frac{E[s^2[\mathrm{n}]]}{E[e^2[\mathrm{n}]]} = \frac{\sigma_x^2}{\sigma_e^2}. \tag{75}$$

The upper equation can be rewritten by considering that the error is related to the dynamic of the differential signal [5], giving

$$SNR = \frac{\sigma_x^2}{\sigma_d^2} \cdot \frac{\sigma_d^2}{\sigma_e^2} = G_P \cdot SNR_Q. \tag{76}$$

In (76), the second factor σ_d^2/σ_e^2 represents the SNR of the quantizer, since it is related to the difference signal and the quantization error from the quantization process. The first factor, instead, represents the gain introduced by the LPC, i.e.

$$G_P = \frac{\sigma_x^2}{\sigma_d^2} \tag{77}$$

41

Figure 25: Theoretical gain in dB for LPC up to the 6-th order as function of PRF.

As it appears evident from the above equation, the gain in the quantization performance is related to the reduction of dynamic [5]. Since the differential signal will have a lower dynamic with respect to the input signal, the amount of information, and hence the number of bits required for coding it for a given performance, will be lower. In Figure 25 are reported the theoretical gain curves derived in the following Subsections as function of PRF.

5.3.1 Analytical Derivation for Gaussian Inputs

Assuming that the input signal is normally distributed (as it is the case for distributed target in SAR) allows the derivation of the variance of the difference signal in closed form, and thus the gain of the LPC according to (78).

$$\mathcal{D} \triangleq \mathcal{X} - \mathcal{Y} \sim \mathcal{N}(0, \sigma_x^2 + \sigma_y^2 - 2\sigma_{xy}) \quad where \quad \begin{aligned} \mathcal{X} &\sim \mathcal{N}(0, \sigma_x^2) \\ \mathcal{Y} &\sim \mathcal{N}(0, \sigma_y^2) \\ \sigma_{xy} &= \sigma_x \sigma_y \rho \end{aligned} \tag{78}$$

The upper equation represents the variance of a difference between two normal distributed random processes as the sum of the two variance minus two time the covariance, which can be expressed as the multiplication of the two standard deviation and the correlation values between the two variables (ρ). The only value known by previous derivation is the correlation between the two variables, while the variance of the two process it is only known to be equal since they are related to the same process ($\sigma_x = \sigma_y$, i.e. stationarity hypothesis hold). The graphical behaviour of the theoretical gain up to the 6-th order is pictured in Figure 25, which has been derived from (70). The detailed mathematical

derivation for the first four orders prediction is given in the following. The gain behaviour for lower order of prediction is generally monotonically increasing, while for the highest orders pictured, it follows an oscillatory trend. This is due to the inversion of the C inversion (according to (70)), which may lead to instability since many ρ values are still equal to zero, as shown in Figure 24.

First-Order Predictor

The application of (78) to the first-order predictor (i.e. $N=1$), thus considering only the previous sample to perform the prediction, allows to derive the gain for this case. Being the two variables dependent from the same process, the variances are initially equal, but as defined in (67), the previous sample is weighted by β_1, leading the definition of the variance of the previous sample to $\sigma_y = \beta_1 \sigma_x$. The weight changes the equation of the differential variance giving

$$\sigma_{d1}^2 = \sigma_x^2 + \sigma_y^2 - 2\sigma_x\sigma_y\rho_1 = \sigma_x^2 + \beta_1^2\sigma_x^2 - 2\sigma_x^2\beta_1\rho_1. \tag{79}$$

Considering from (67), the β_1 value that minimize the MMSE for the first order of prediction is given by the following calculation

$$\boldsymbol{\beta} = \boldsymbol{C^{-1}\rho} \quad \rightarrow \quad \beta_1 = [1]^{-1}\rho_1 = \rho_1. \tag{80}$$

By substituting (80) in (79), the definition of variance for the first order predictor is given by

$$\sigma_{d1}^2 = \sigma_x^2 + \rho_1^2\sigma_x^2 - 2\sigma_x^2\rho_1^2 = \sigma_x^2(1 - \rho_1^2). \tag{81}$$

From the upper equation it is possible to see that any value of $\rho_1 > 0$ will cause a reduction of σ_{d1}^2 with respect to σ_x^2, as the weight is the optimal. An example of reduction of dynamic for this case is pictured in Figure 26, where the left graph (Figure 26a) shows the Probability Density Function (PDF) for the real part of the input signal. As PRF
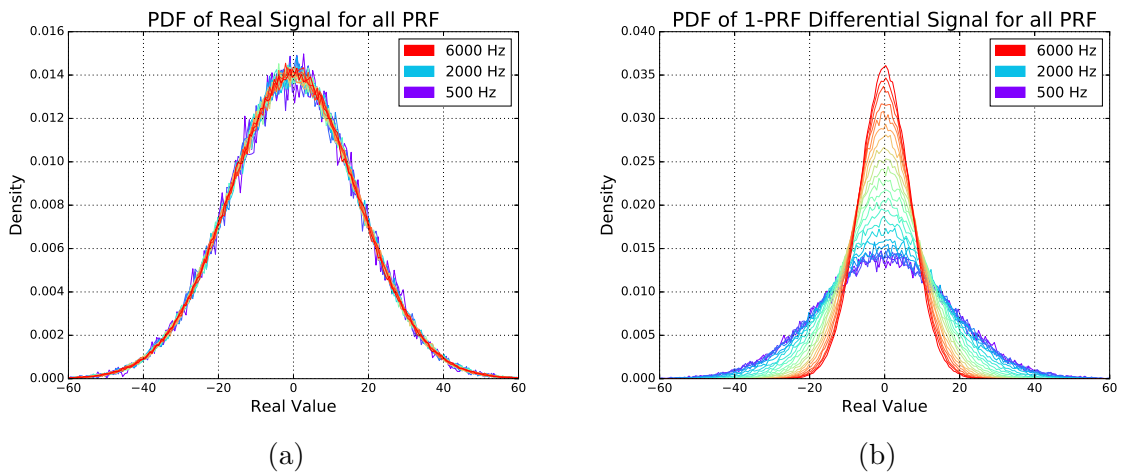

Figure 26: Probability density function of the real values of the original signal (a) and the differential coming from the weighted 1 sample subtraction (b).

increases, the variance (i.e. the dispersion of the curves from the mean value) remains

constant, as expected. On the right graph (26b), which shows the variance (81) calculated for different values of PRF, it is possible to see that the higher the PRF (i.e. the value of ρ_1), the narrower the resulting distribution (i.e. the smaller the standard deviation). Knowing the weight (80) and the dynamic of the differential signal (81), it is possible to define in closed form the gain for the first order predictor applying (77), giving

$$G_1 = \frac{\sigma_x^2}{\sigma_x^2(1 - \rho_1^2)} = \frac{1}{1 - \rho_1^2}. \tag{82}$$

Second-Order Predictor

The second-order predictor considers the two previous samples to perform the prediction. As for the previous Section, both β and σ_{d2}^2 are necessary to retrieve the gain in close form. Assuming that the variables are normal distributed (78), the second order implies that the two previous samples are weighted for the corresponding β_i calculated as

$$\boldsymbol{\beta} = \boldsymbol{C}^{-1}\boldsymbol{\rho} \quad \rightarrow \quad \begin{bmatrix} \beta_1 \\ \beta_2 \end{bmatrix} = \begin{bmatrix} 1 & \rho_1 \\ \rho_1 & 1 \end{bmatrix}^{-1} \begin{bmatrix} \rho_1 \\ \rho_2 \end{bmatrix}, \tag{83}$$

weighting also the related variance of each variable. Applying (78) to this case, follows that

$$\mathcal{X} \sim \mathcal{N}(0, \sigma_x^2), \quad \mathcal{Y} \sim \mathcal{N}(0, \sigma_y^2) = \mathcal{N}(0, \beta_1^2\sigma_x^2), \quad \mathcal{Z} \sim \mathcal{N}(0, \sigma_z^2) = \mathcal{N}(0, \beta_2^2\sigma_x^2) \tag{84}$$

and the variance of the difference is then equal to

$$\mathcal{D} \triangleq \mathcal{X} - \mathcal{Y} - \mathcal{Z} \sim \mathcal{N}(0, \sigma_x^2 + \sigma_y^2 + \sigma_z^2 - 2\sigma_{xy} - 2\sigma_{xz} + 2\sigma_{yz}), \tag{85}$$

while the calculation of the covariances between the variables is done in the same manner ($\sigma_{xy} = \sigma_x\sigma_y\rho_1$, $\sigma_{xz} = \sigma_x\sigma_z\rho_2$ and $\sigma_{yz} = \sigma_x\sigma_z\rho_1$). By expanding (85), the variance of the differential signal for the second order predictor is defined as

$$\sigma_{d2}^2 = \sigma_x^2(1 + \beta_1^2 + \beta_2^2 + 2\rho_1\beta_1 - 2\rho_2\beta_2 + 2\beta_1\beta_2), \tag{86}$$

while the prediction gain is equal to

$$G_2 = \frac{1}{1 + \beta_1^2 + \beta_2^2 + 2\rho_1\beta_1 - 2\rho_2\beta_2 + 2\beta_1\beta_2}. \tag{87}$$

Third-Order Predictor

The third-order differential signal is defined as

$$\mathcal{D} \triangleq \mathcal{X} - \mathcal{Y} - \mathcal{Z} - \mathcal{W} \sim \mathcal{N}(0, \sigma_{d3}^2), \tag{88}$$

44

the considered weights are calculated from

$$
\boldsymbol{\beta} = \boldsymbol{C}^{-1}\boldsymbol{\rho} \quad \rightarrow \quad
\begin{bmatrix} \beta_1 \\ \beta_2 \\ \beta_3 \end{bmatrix} =
\begin{bmatrix} 1 & \rho_1 & \rho_2 \\ \rho_1 & 1 & \rho_1 \\ \rho_2 & \rho_1 & 1 \end{bmatrix}^{-1}
\begin{bmatrix} \rho_1 \\ \rho_2 \\ \rho_3 \end{bmatrix}.
\tag{89}
$$

The variables to be considered are four, and as the previous case known as

$$
\begin{aligned}
\mathcal{X} &\sim \mathcal{N}(0,\sigma_x^2), & \mathcal{Y} &\sim \mathcal{N}(0,\sigma_y^2) = \mathcal{N}(0,\beta_1^2\sigma_x^2), \\
\mathcal{Z} &\sim \mathcal{N}(0,\sigma_z^2) = \mathcal{N}(0,\beta_2^2\sigma_x^2), & \mathcal{W} &\sim \mathcal{N}(0,\sigma_w^2) = \mathcal{N}(0,\beta_3^2\sigma_x^2).
\end{aligned}
\tag{90}
$$

The calculation of the variance of the difference signal $\mathcal{D}$ is performed again exploiting the weights applied to the variance of the variables ($\sigma_{xy} = \sigma_x\sigma_y\rho_1, \sigma_{xz} = \sigma_x\sigma_z\rho_2, \sigma_{xw} = \sigma_x\sigma_w\beta_3, \sigma_{yz} = \sigma_x\sigma_z\rho_1, \sigma_{yw} = \sigma_y\sigma_w\rho_2$ and $\sigma_{zw} = \sigma_z\sigma_w\rho_1$), and defined as

$$
\sigma_{d3}^2 = \sigma_x^2[1 + \beta_1^2 + \beta_2^2 + \beta_3^2 + 2\rho_1(-\beta_1 + \beta_1\beta_2 + \beta_2\beta_3) + 2\rho_2(-\beta_2 + \beta_1\beta_3) - 3\rho_3\beta_3].
\tag{91}
$$

The gain is then retrieved as

$$
G_3 = [1 + \beta_1^2 + \beta_2^2 + \beta_3^2 + 2\rho_1(-\beta_1 + \beta_1\beta_2 + \beta_2\beta_3) + 2\rho_2(-\beta_2 + \beta_1\beta_3) - 3\rho_3\beta_3]^{-1}
\tag{92}
$$

Fourth-Order Predictor

By increasing the prediction to the fourth-order, the differential signal is given by

$$
\mathcal{D} \triangleq \mathcal{X} - \mathcal{Y} - \mathcal{Z} - \mathcal{W} - \mathcal{V} \sim \mathcal{N}(0,\sigma_{d4}^2),
\tag{93}
$$

where the considered weights are calculated from

$$
\boldsymbol{\beta} = \boldsymbol{C}^{-1}\boldsymbol{\rho} \quad \rightarrow \quad
\begin{bmatrix} \beta_1 \\ \beta_2 \\ \beta_3 \\ \beta_4 \end{bmatrix} =
\begin{bmatrix} 1 & \rho_1 & \rho_2 & \rho_3 \\ \rho_1 & 1 & \rho_1 & \rho_2 \\ \rho_2 & \rho_1 & 1 & \rho_1 \\ \rho_3 & \rho_2 & \rho_1 & 1 \end{bmatrix}^{-1}
\begin{bmatrix} \rho_1 \\ \rho_2 \\ \rho_3 \\ \rho_4 \end{bmatrix}.
\tag{94}
$$

The variables to be considered are four and defined as

$$
\begin{aligned}
\mathcal{X} &\sim \mathcal{N}(0,\sigma_x^2), & \mathcal{Y} &\sim \mathcal{N}(0,\sigma_y^2) = \mathcal{N}(0,\beta_1^2\sigma_x^2), & \mathcal{Z} &\sim \mathcal{N}(0,\sigma_z^2) = \mathcal{N}(0,\beta_2^2\sigma_x^2), \\
& & \mathcal{W} &\sim \mathcal{N}(0,\sigma_w^2) = \mathcal{N}(0,\beta_3^2\sigma_x^2), & \mathcal{V} &\sim \mathcal{N}(0,\sigma_v^2) = \mathcal{N}(0,\beta_4^2\sigma_x^2).
\end{aligned}
\tag{95}
$$

Applying the weights the covariances are defined as

$$
\begin{aligned}
\sigma_{xy} &= \sigma_x\sigma_y\rho_1, & \sigma_{xz} &= \sigma_x\sigma_z\rho_2, & \sigma_{xw} &= \sigma_x\sigma_w\rho_3, & \sigma_{xv} &= \sigma_x\sigma_v\rho_4, \\
\sigma_{yz} &= \sigma_x\sigma_z\rho_1, & \sigma_{yw} &= \sigma_y\sigma_w\rho_2, & \sigma_{yv} &= \sigma_y\sigma_v\rho_3, \\
\sigma_{zw} &= \sigma_z\sigma_w\rho_1, & \sigma_{zv} &= \sigma_z\sigma_v\rho_2, \\
\sigma_{wv} &= \sigma_w\sigma_v\rho_1.
\end{aligned}
\tag{96}
$$

The variance of the differential signal for the fourth-order predictor is derived as

$$
\begin{aligned}
\sigma_{d4}^2 =\sigma_x^2[&1 + \beta_1^2 + \beta_2^2 + \beta_3^2 + \beta_4^2 + \\
&+ 2\rho_1(-\beta_1 + \beta_1\beta_2 + \beta_2\beta_3 + 2\beta_3\beta_4) + \\
&+ 2\rho_2(-\beta_2 + \beta_1\beta_3 + \beta_2\beta_4) + \\
&+ 2\rho_3(-\beta_3 + \beta_2\beta_4)]
\end{aligned}
\tag{97}
$$

The gain calculation comes after the application of the ratio as in (75), resulting in

$$
\begin{aligned}
G_4 =[&1 + \beta_1^2 + \beta_2^2 + \beta_3^2 + \beta_4^2 + \\
&+ 2\rho_1(-\beta_1 + \beta_1\beta_2 + \beta_2\beta_3 + 2\beta_3\beta_4) + \\
&+ 2\rho_2(-\beta_2 + \beta_1\beta_3 + \beta_2\beta_4) + \\
&+ 2\rho_3(-\beta_3 + \beta_2\beta_4)]^{-1}
\end{aligned}
\tag{98}
$$

6 Simulation Results

In order to evaluate the theoretical performance of the joint use of Linear Predictive Coding applied to SAR data, a set of Monte Carlo simulations have been performed. The Tandem-L system parameters (i.e. wavelength, antenna length, orbit height...) as defined in Chapter 3,have been assumed for the present investigations starting from the verification of the technique on a single azimuth line in uniform PRI domain and the use of a uniform ADC as quantizer, a focusing has also been implemented for considering the performance on the whole processing chain. Moving to non-uniform PRI domain, a general case has been conducted performing interpolation and successively the focusing. As a final result, the application on the real Tandem-L mission scenario has been considered, which represents a specific case where the non-uniform PRI is employed (see Section 3.1) with the addition of gaps. This last simulation has been conducted in a 2D domain (i.e., considering range and azimuth dimensions) applying together Linear Predictive Coding and Block Adaptive Quantization (BAQ, see Section 4.1.2).

6.1 Uniform Sampling

As first investigation, the coding scheme defined in Figure 20 has been applied on a single raw azimuth line generated as in (71). The selected parameters for the quantization are a V_{clip}=127.5 and γ_{clip}=-10 dB for this analysis as well as for all the results presented in the following Sections. The encoding process has been carried out separately on both real and imaginary part of the signal as we are considering a cartesian quantizer. Moreover, the two components are assumed to be uncorrelated between each other (20) for a distributed target. The decoding process is then applied to the encoded and quantized data, giving as output the reconstructed signal. The same processing chain has been considered for three prediction order and also to the direct quantizer as benchmark performance. For the evaluation of the reconstruction performance the SQNR is calculated for each output signal, considering as the original signal the non-quantized raw data as in (52) for a complex signal calculated over all the available N pixels,

$$\text{SQNR}_{\text{dB}} = 10 \cdot \log_{10} \left(\frac{\sum_{i=1}^{N} |s_i|^2}{\sum_{i=1}^{N} |e_i|^2} \right) \quad \text{where} \quad e_i = s_i - s_{q,i} \tag{99}$$

being in this equation s the non-quantized signal and s_q the quantized version of s. The performance evaluation on raw data is considered between the original signal s, the output of the direct quantization s_q and the reconstructed signal after encoding and decoding processes at three different orders of prediction: s_{1q}, s_{2q} and s_{3q}. The SQNR evaluated on those signals is pictured in Figure 28, 29 and 30. As it is possible to see in Figure 28, the SQNR of the direct quantizer (bullets), is constant as the PRF increases for all bitrates. Moreover, the difference in terms of SQNR from one bitrate to the upper one is equal to 6 dB, as introduced in (54). The SQNR related to the predictive quantizer
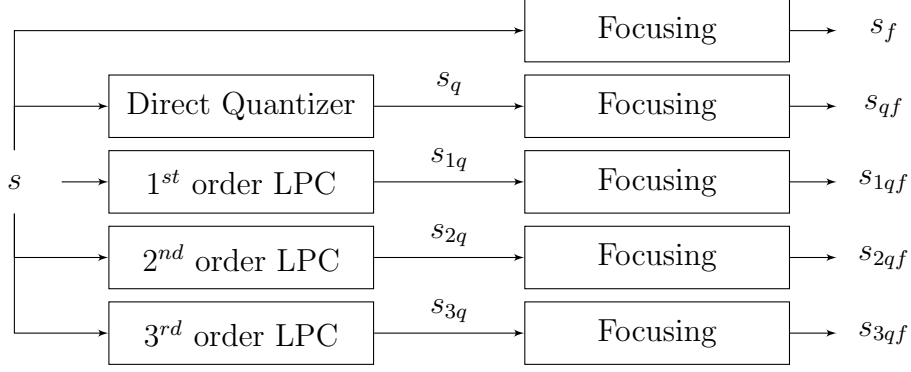
Focusing $\rightarrow s_f$

Direct Quantizer $\quad s_q \quad$ Focusing $\rightarrow s_{qf}$

$s \rightarrow$ 1st order LPC $\quad s_{1q} \quad$ Focusing $\rightarrow s_{1qf}$

2nd order LPC $\quad s_{2q} \quad$ Focusing $\rightarrow s_{2qf}$

3rd order LPC $\quad s_{3q} \quad$ Focusing $\rightarrow s_{3qf}$

Figure 27: Processing chain for uniform PRI investigation.

(triangles) is instead increasing as the PRF increase, maintaining the same behaviour for all the bitrates. Second and third order predictor shows the same trend but with a further increase of SQNR (gain), as pictured in Figure 29 and Figure 30. In order to evaluate correctly the gain introduced by the predictive quantization in raw data, it is necessary to define the difference between the predictive SQNR and the direct SQNR, named Δ_{SQNR} (100).

$$\Delta_{\mathrm{SQNR}} = \mathrm{SQNR}_{\mathrm{pred,dB}} - \mathrm{SQNR}_{\mathrm{dir,dB}} \tag{100}$$

The result for the prediction gain for first second and third order predictors are pictured in Figure 31, 32 and 33 respectively. The theoretical gain curves derived in (82), (87) and (92) are overplotted on the respective gain graph. For all the three predictors, the retrieved gain from the simulations is coherent with the expected theoretical value for all the bitrates except the 2 bps. For this last case, the gain is around two dB more than expected, this is because the uniform ADC can be more sensitive to the reduction of dynamic, having more impact in the reduction of the quantization error. After performing the focusing operation described in Section 2.2.2, the SQNR is calculated again in order to evaluate the quality of the encoding after the whole processing chain. For azimuth focusing, a processing bandwidth $B_d = 780$ Hz has been considered, which leads to an azimuth resolution of around 10 m. For this, the original non quantized focused signal (s_f) has been considered as a reference, while each version of the quantized signal has been focused as well giving s_{qf}, s_{1qf}, s_{2qf} and s_{qf}, as pictured in Figure 27. The resulting SQNR is reported in Figure 34, 35 and 36. It can be noticed that also on the focused signal, the predictive quantization introduces the same coherent gain. One interesting fact is the small amount of gain which affects the entire system as the PRF increases, thus also the direct quantizer. An explanation for this behavior comes from the consideration of sampling and quantizing as the two sides of the same coin, in the sense that a larger PRF (i.e. a finer sampling) can be applied in order to recover a certain amount of information which has been lost in the quantization process (of course, both sampling and quantization rates directly impact the final system data rate) [8]. The gain for the focused analysis for the different orders of prediction and for the standard bitrate of Tandem-L system (i.e. 4 bits/samples) is depicted in Figure 37. Hence, it can be concluded that the proposed technique has shown results coherent with the theory expectation, also after the focusing operation. If considering the typical Tandem-L PRF (i.e. 2700 Hz), this simulation suggest that 2.5, 3 and 4 dB of gain are introduced by the first, second and third orders

of prediction. Taking into account (54), the boundary of 1 bit per sample in terms of data reduction is not achievable. Further analysis on this argument are faced in the final result on the specific Tandem-L simulation (see Section 6.3.1).
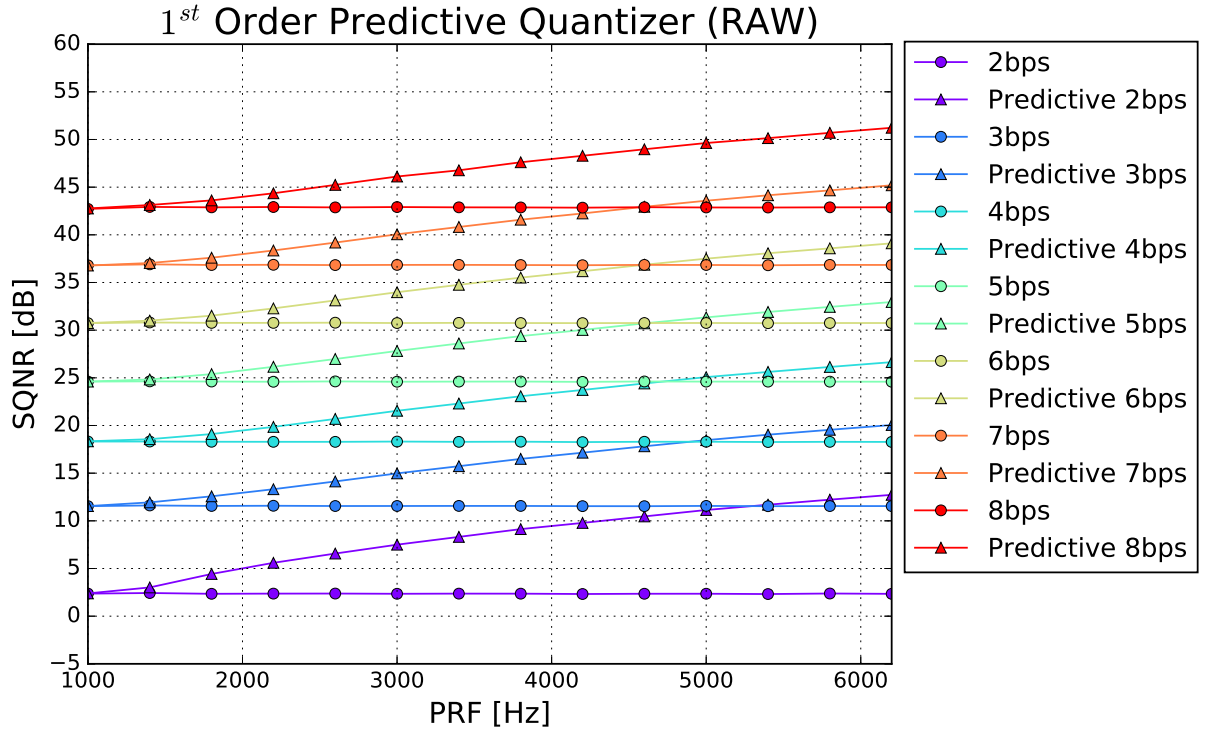

Figure 28: SQNR evaluated on raw data with uniform PRI for the direct and first-order predictive quantizers as function of PRF at different bitrates.
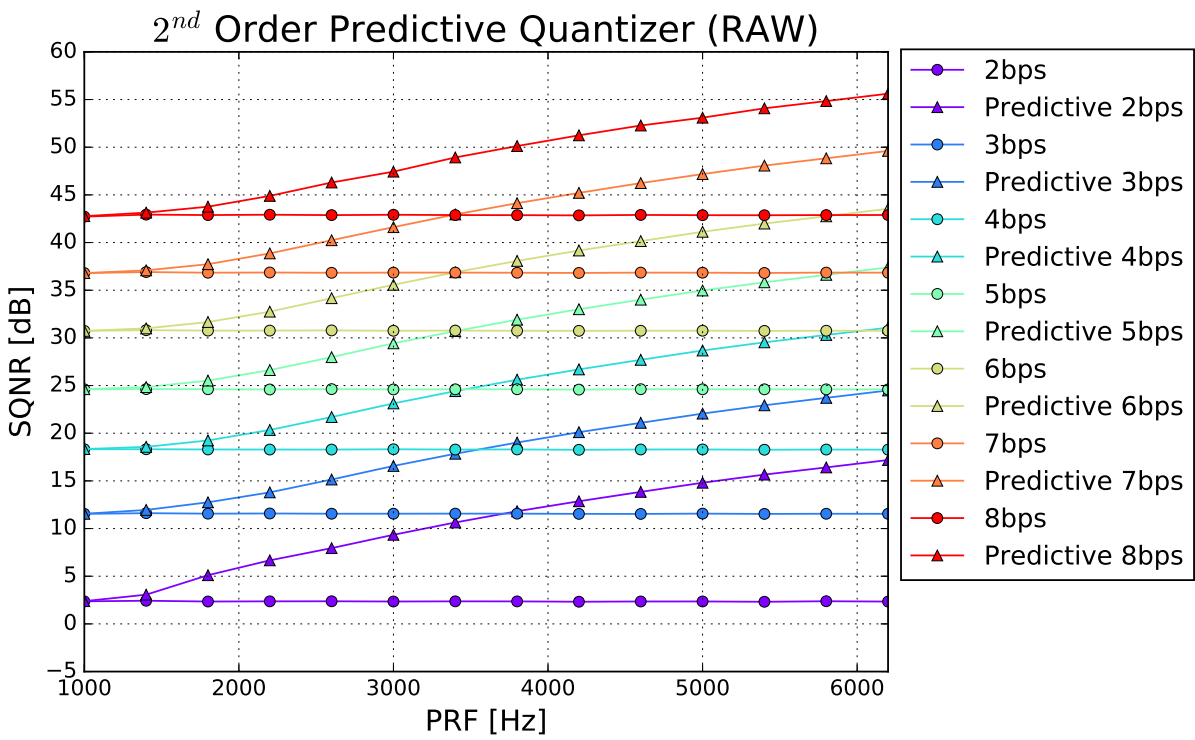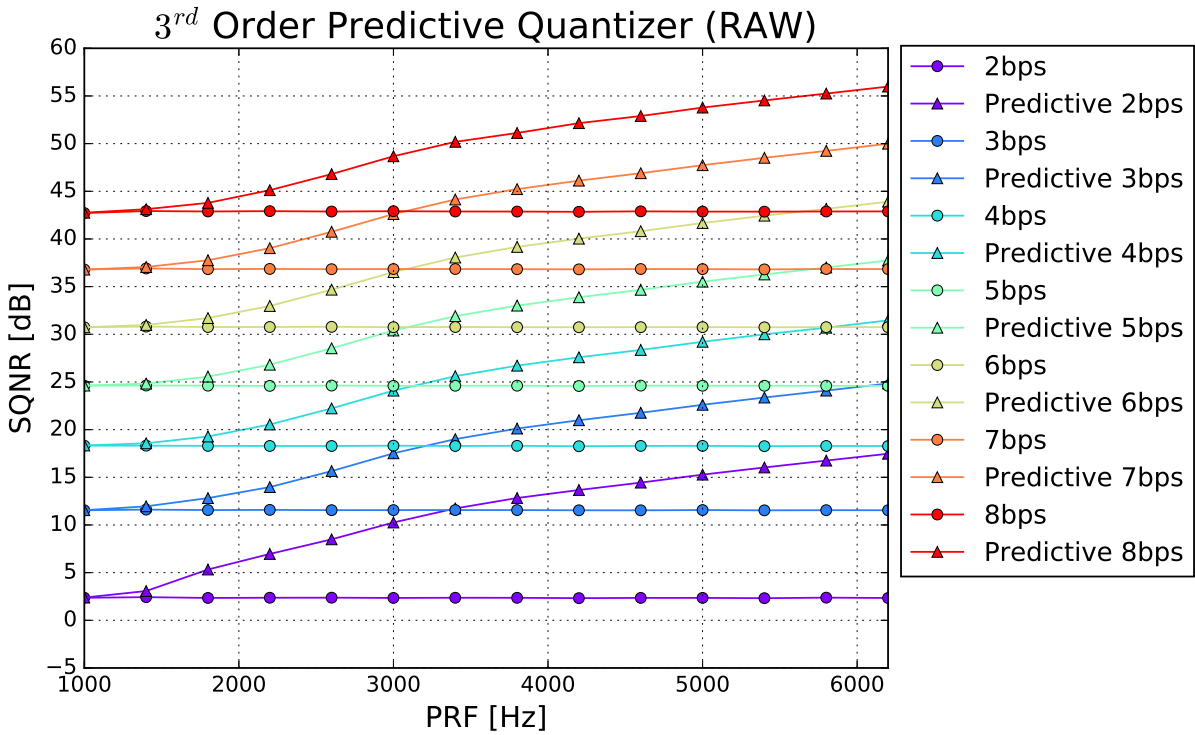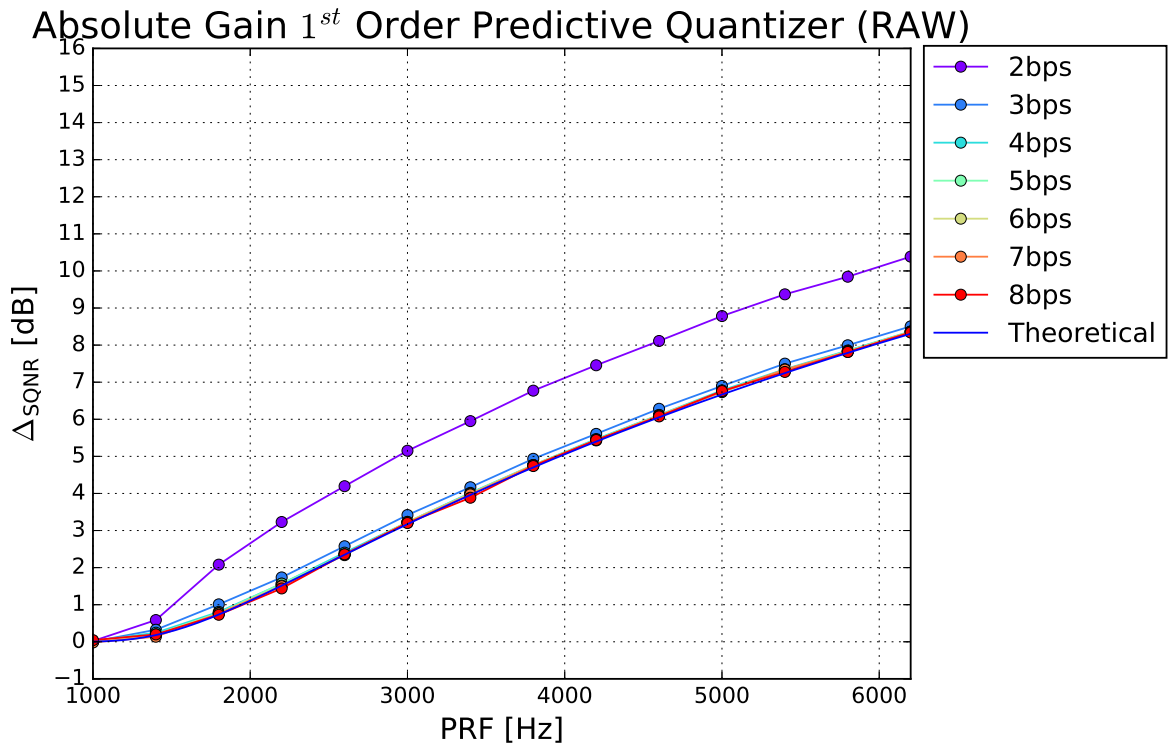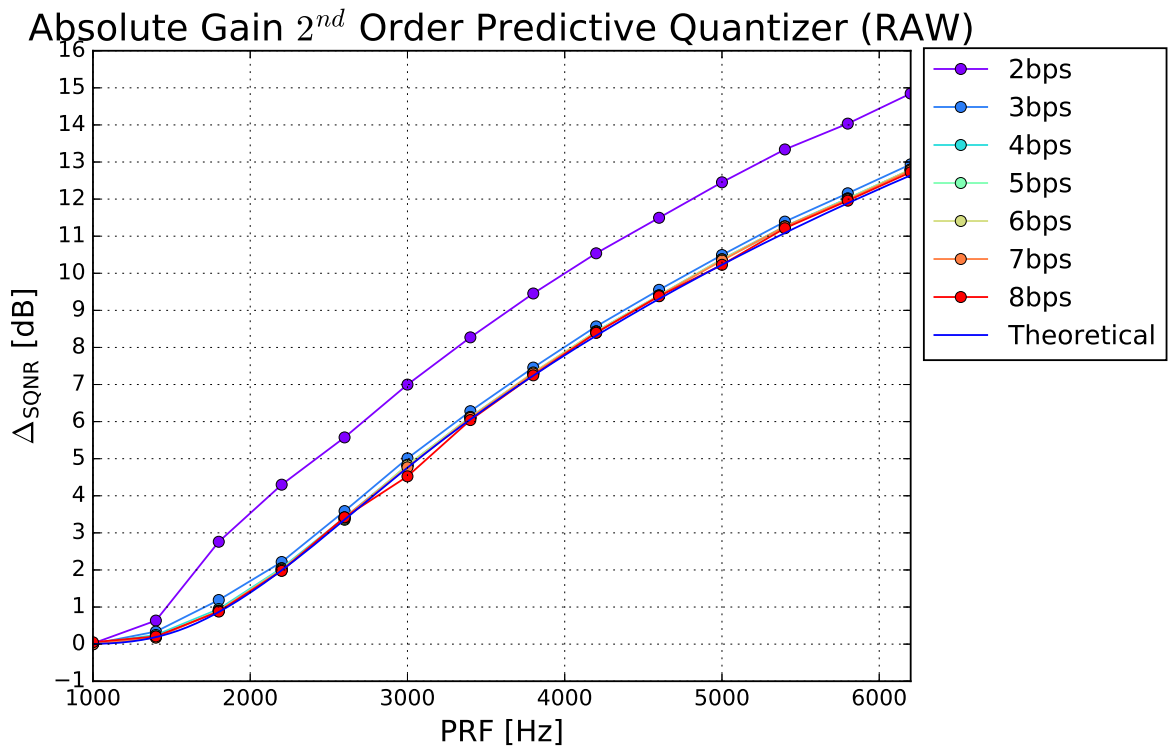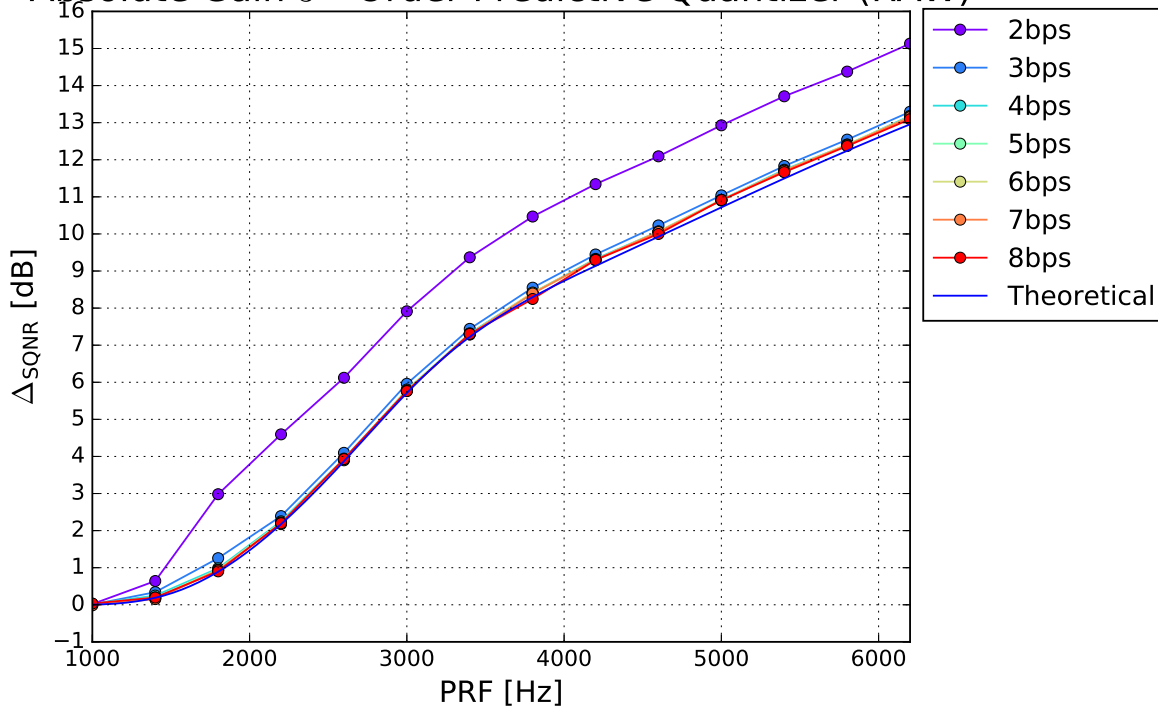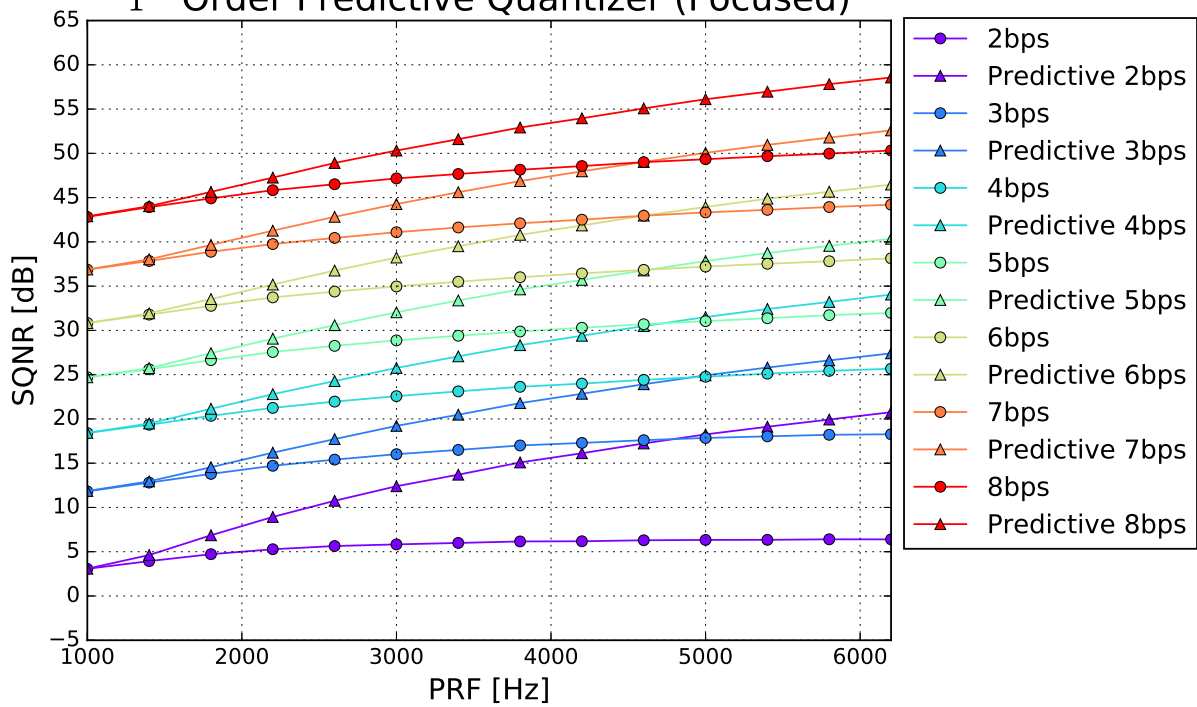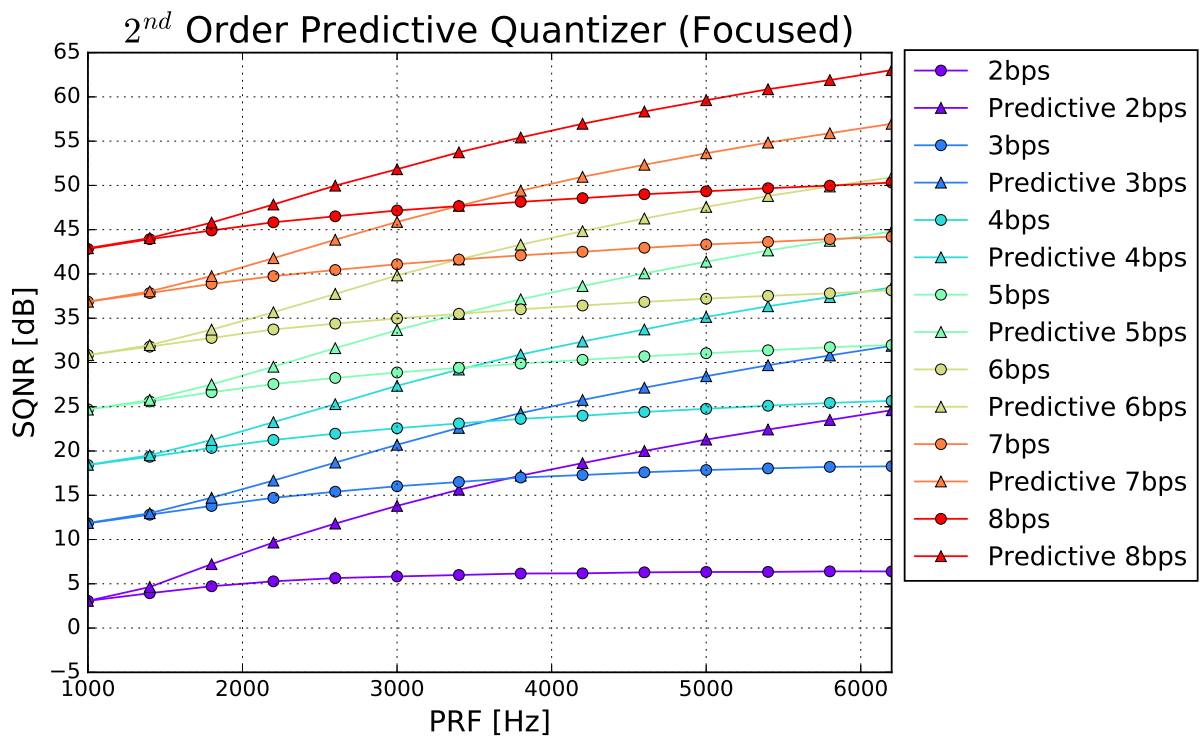
Figure 29: SQNR evaluated on raw data with uniform PRI for the direct and second-order predictive quantizers as function of PRF at different bitrates.
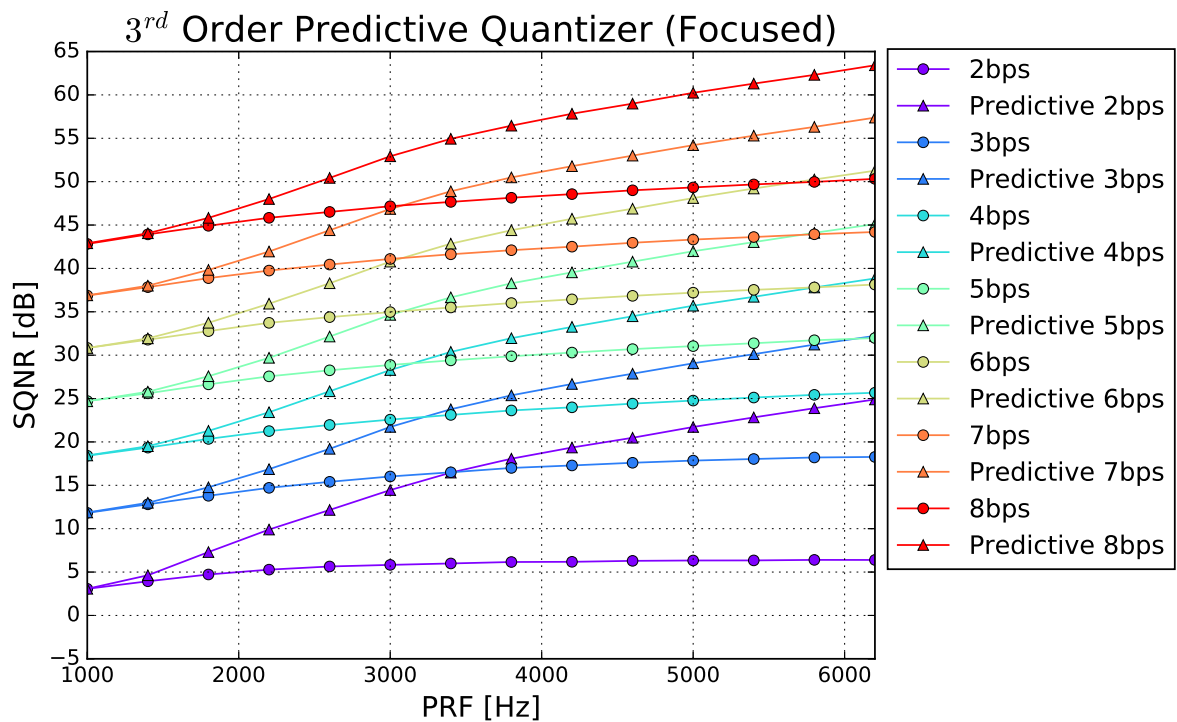

Figure 30: SQNR evaluated on raw data with uniform PRI for the direct and third-order predictive quantizers as function of PRF at different bitrates.

Figure 31: Gain evaluated on raw data with uniform PRI for the direct and first-order predictive quantizers as function of PRF at different bitrates.

Figure 32: Gain evaluated on raw data with uniform PRI for the direct and second-order predictive quantizers as function of PRF at different bitrates.

Figure 33: Gain evaluated on raw data with uniform PRI for the direct and third-order predictive quantizers as function of PRF at different bitrates.

Figure 34: SQNR evaluated on focused data with uniform PRI for the direct and first order predictive quantizers as function of PRF at different bitrates.
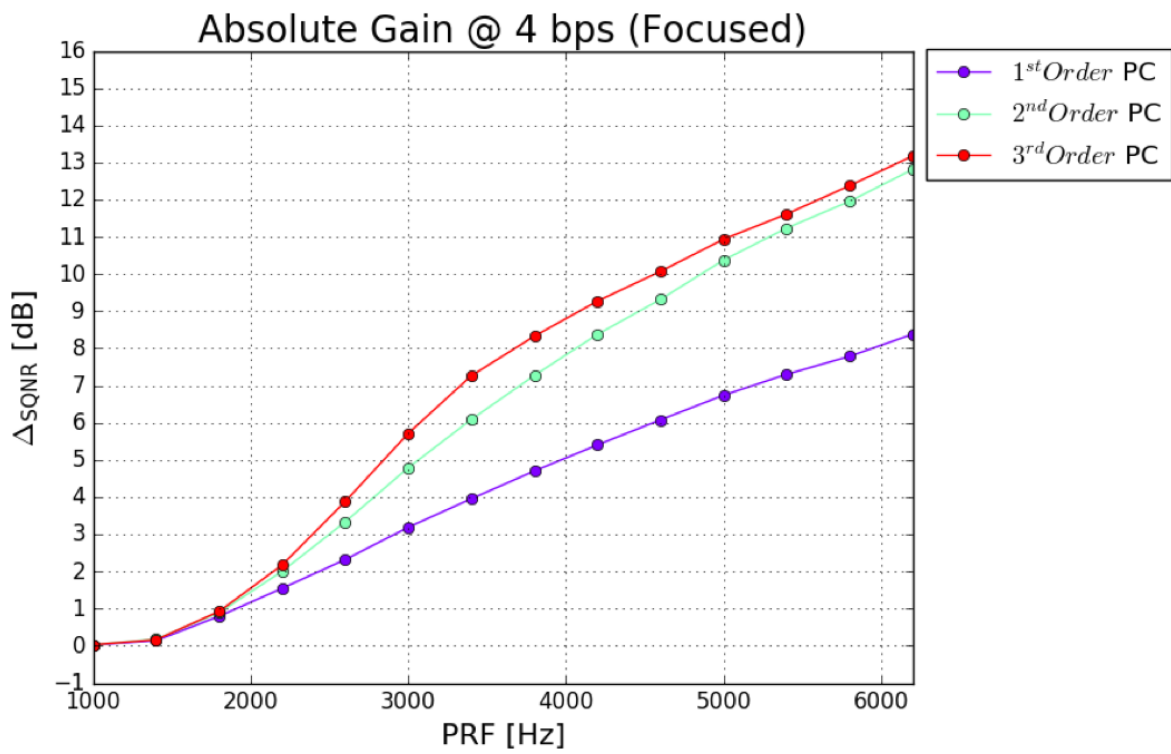
Figure 35: SQNR evaluated on focused data with uniform PRI for the direct and second order predictive quantizers as function of PRF at different bitrates.

Figure 36: SQNR evaluated on focused data with uniform PRI for the direct and third-order predictive quantizers as function of PRF at different bitrates.

Figure 37: Gain evaluated on focused data with uniform PRI for the first, second and third-order predictive quantizers as function of PRF at 4 bits/samples (which is the standard bitrate employed for Tandem-L mission).

6.1.1 TanDEM-X case study

The results presented in the previous case are promising, although it is important to take into account that the characteristics of the simulated systems are referred to Tandem-L. By considering to apply the proposed technique of Linear Predictive Coding and quantization on existent systems, a special case has been investigated in this section. The German Aerospace Center (DLR) developed under a public–private partnership between and Astrium GmbH the TanDEM-X (the TerraSAR-X add-on for Digital Elevation Measurement) mission, an X-band bistatic SAR interferometer composed by two twin satellites, TerraSAR-X (launched in 2007) [24] and TanDEM-X (launched in 2010) [10][26], which opened a new era in spaceborne radar remote sensing. According to the parameters listed in Table 3 the investigation has been tuned to its system characteristics. In

Parameter	Value
Orbit height	514 km
Local time	18 h
Inclination	97.44°
Revisit time	11 days
Frequency	X-Band
Range bandwidth	100 MHz
Azimuth resolution	1 m … 16 m
Swath width	10 km … 100 km
Antenna length	4.8 m
Antenna width	0.8 m
PRF	∼3 kHz (single-pol)

Table 3: TanDEM-X system parameters.

particular, the PRF for the system is uniform and the antenna length is different from the previous case as well as geometric parameters such as the orbit height (see Table 1 for comparison). As the antenna pattern is different and the antenna length is smaller than the Tandem-L case, according to (74) a faster decrease of correlation between samples as the PRI increases is expected. As pictured in Figure 38 and 39, the expected results have been confirmed by simulation. Hence, this analysis proves that applying predictive quantization in the context of the TanDEM-X mission, as shown in Figure 40 and 41, would lead to a negligible performance gain (less than 0.5 dB) for typical PRF values in the order of 3 kHz.
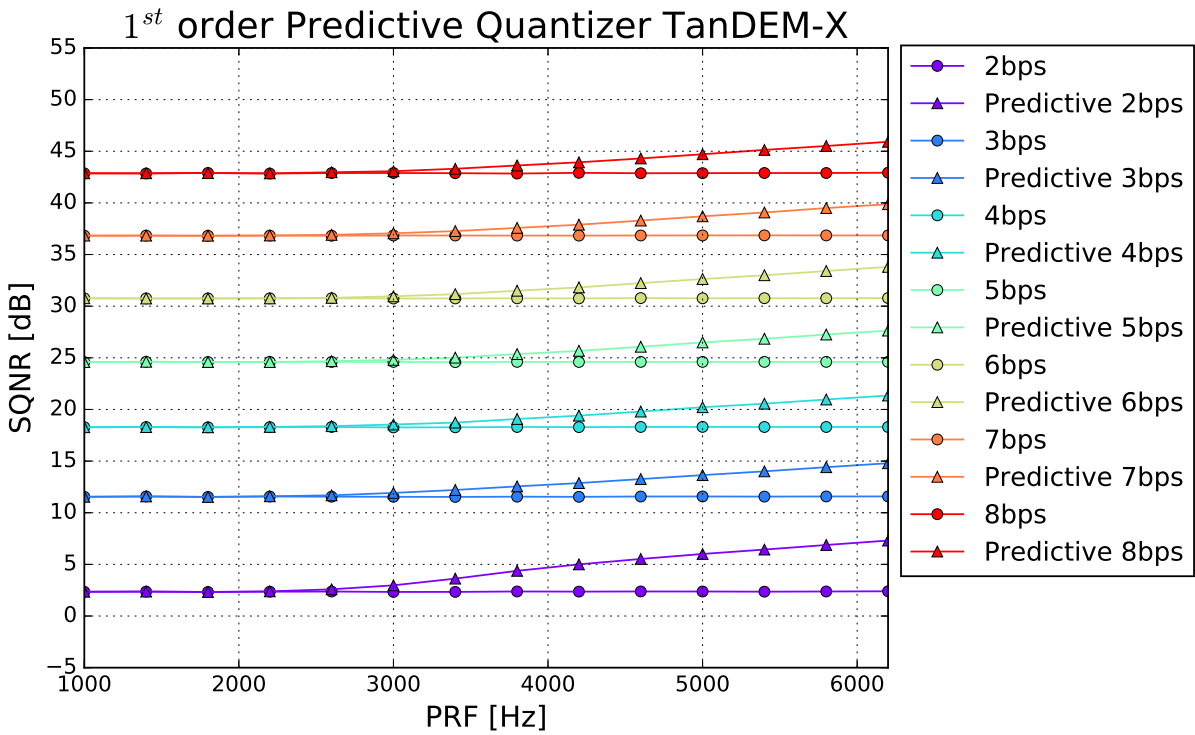
Figure 38: SQNR evaluated on raw data for 1st order Predictive Quantizer as function of PRF at different bitrate applied on TanDEM-X system parameters.
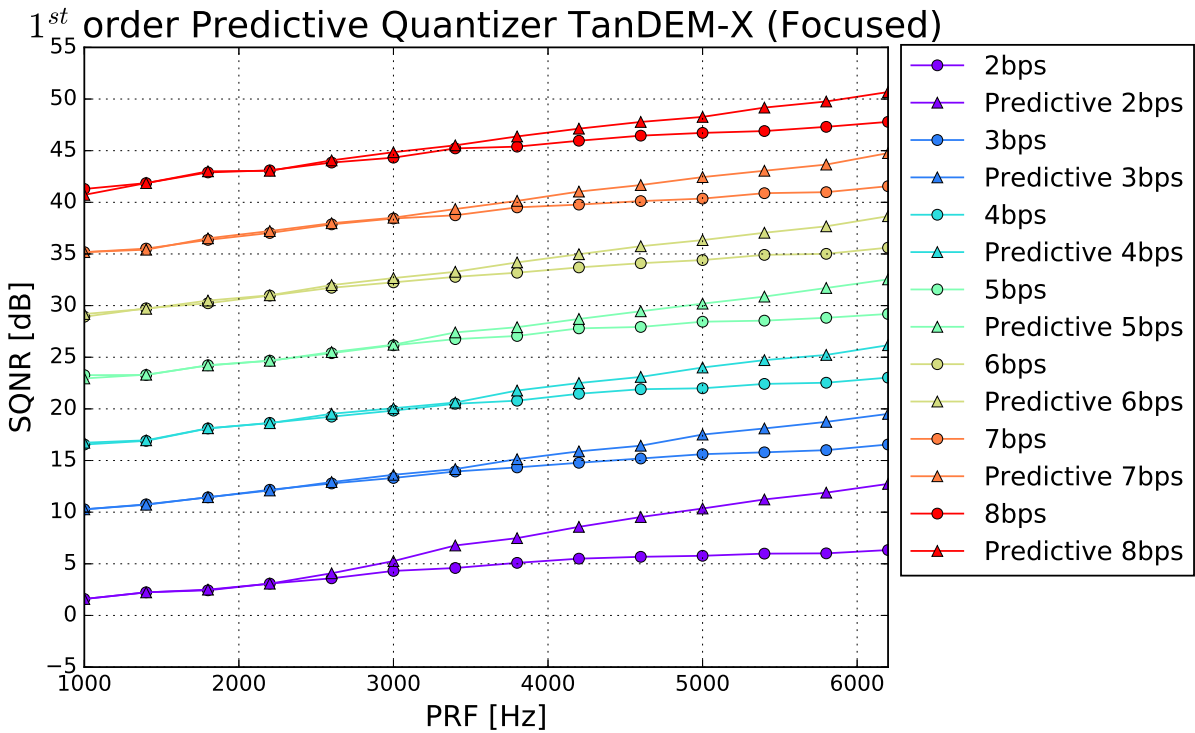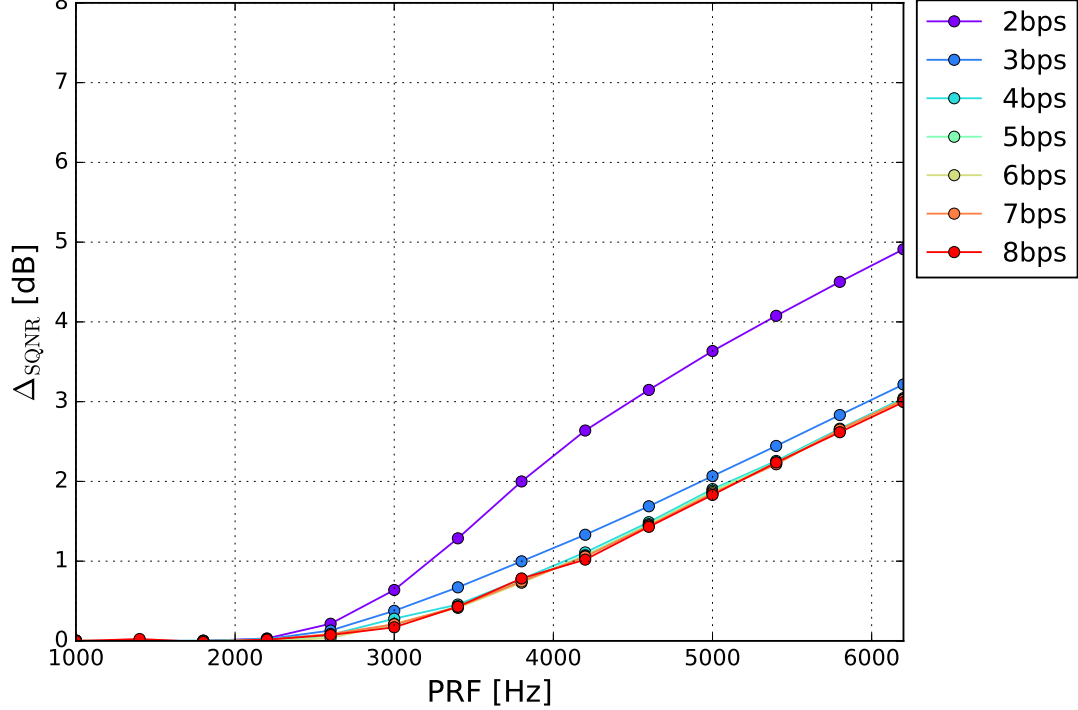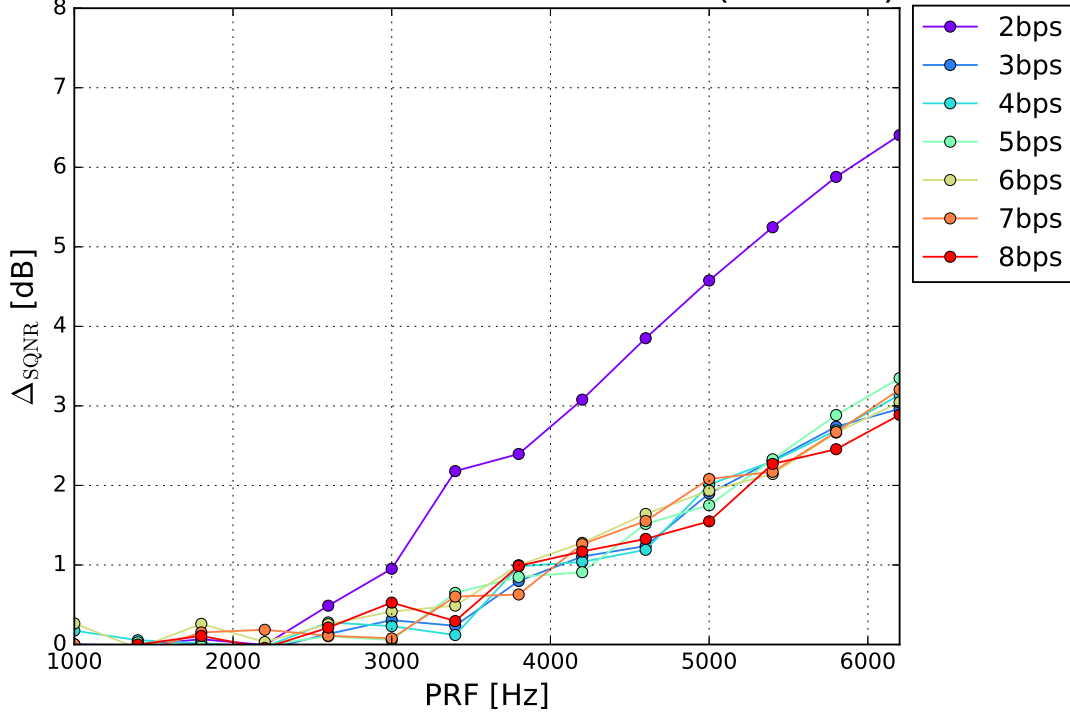

Figure 39: SQNR evaluated on focused data for 1st order Predictive Quantizer as function of PRF at different bitrate applied on TanDEM-X system parameters.

Figure 40: SQNR evaluated on raw data for 1st order Predictive Quantizer as function of PRF at different bitrate applied on TanDEM-X system parameters.

Figure 41: SQNR evaluated on raw data for 1st order Predictive Quantizer as function of PRF at different bitrate applied on TanDEM-X system parameters.

6.2 Non-Uniform Sampling

A non-uniform PRI is considered, i.e. a PRI which is varying during the azimuth (slow) time, the raw data generation is not anymore possible in the same way as done for of the uniform domain. The chosen technique for generating the non-uniform raw data is pictured in Figure 42, where n represents the normal distributed random process which is convoluted with an antenna pattern generated at a very high PRI (1 MHz). Up to
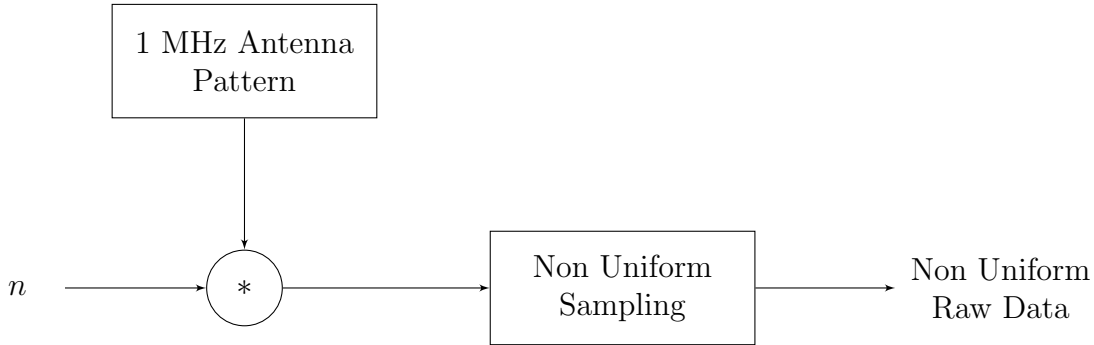

Figure 42: Generation of non-uniform PRI raw data.

this point the process is equal as for the uniform domain (71). The raw 1 MHz signal is then sampled according a proper PRI variation, . For the considered scenario, a variation of $\pm 20\%$ with respect to the mean PRF, $\overline{\text{PRF}}$, has been considered. Hence, for this analysis the PRI varies linearly from -20% to $+20\%$ with 20 cyclic variations. Considering the variation of PRI among subsequent samples, it is obvious that also the correlation between them varies. In order to evaluate the performance by properly taking into account the resulting variation of correlation, three different configurations for the first order of prediction have been tested:

1. The weight associated to the $\overline{\text{PRF}}$ is employed for for all the samples. This is expected to be the worst solution in terms of performance but, at the same time, the less complex, since only one coefficient would be necessary to use and route for on-board implementation.

2. The correct weight (i.e. the one resulting from the correlation estimated for each PRI value) for each PRI value. This solution should be the best in terms of performance but, on the other hand, the most complex since a different weight for each value must be stored and correctly applied.

3. As a trade-off between the two previous solutions, an intermediate solution is considered where only three weights are considered. They are selected as follows: the weight associated to the 3$^{\text{rd}}$ PRI variation for characterizing the first 7 samples, the weight related to the 10$^{\text{th}}$ PRI for characterize the second 7 samples and the weight related to the 17$^{\text{th}}$ PRI for characterizing the last 6 samples (i.e. the correlation value associated to the mean PRI of each sub-interval.

The described approaches are referred to as 1β, 20β and 3β in the following graphs, respectively. As it has already been pointed out, the variation of dynamic in the present scenario represents an extreme case with respect to the staggered SAR case for Tandem-L
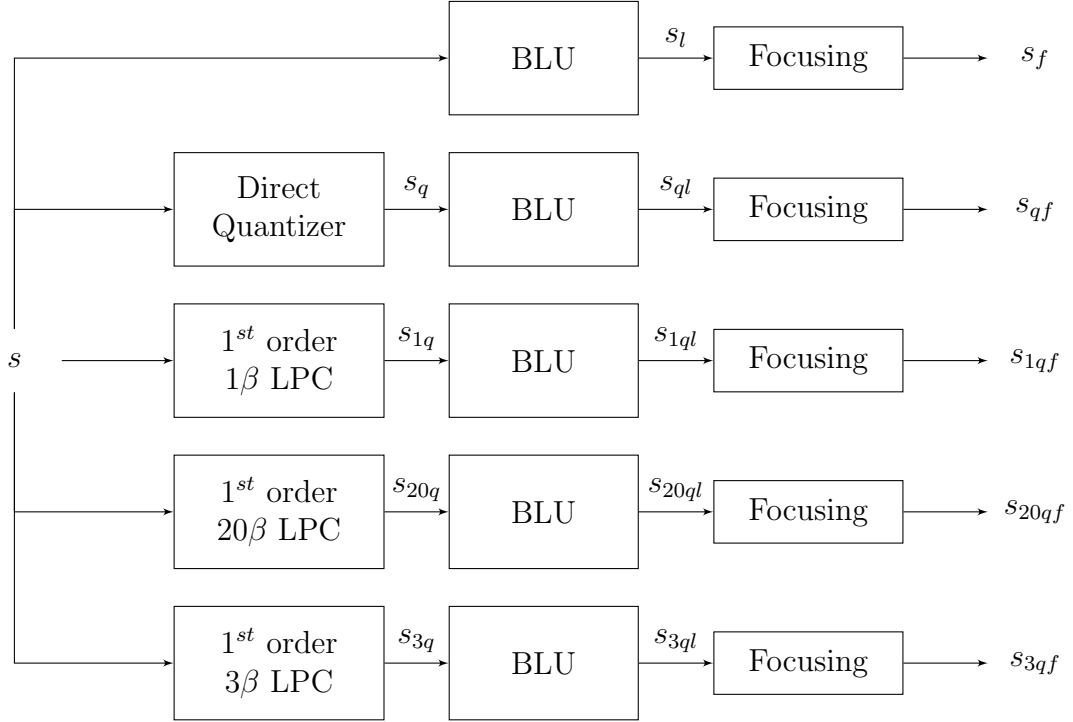
BLU $\;s_l\;$ Focusing $\;\longrightarrow\; s_f$

Direct Quantizer $\;s_q\;$ BLU $\;s_{ql}\;$ Focusing $\;\longrightarrow\; s_{qf}$

1st order 1β LPC $\;s_{1q}\;$ BLU $\;s_{1ql}\;$ Focusing $\;\longrightarrow\; s_{1qf}$

s

1st order 20β LPC $\;s_{20q}\;$ BLU $\;s_{20ql}\;$ Focusing $\;\longrightarrow\; s_{20qf}$

1st order 3β LPC $\;s_{3q}\;$ BLU $\;s_{3ql}\;$ Focusing $\;\longrightarrow\; s_{3qf}$

Figure 43: Processing chain for uniform PRI investigation.

(which normally considers a variation of less than $\pm 10\%$). Together with the prediction weights, the correct set of α implemented in the quantizer has been considered for rescaling the sample related to the corresponding PRI. Thus all the 20 values of α have been taken into account for a proper and fair performance comparison. The flowchart of the processing chain for this analysis is sketched in Figure 43. In order to evaluate the performance after the focusing, an interpolation to a uniform grid of samples is mandatory to perform the convolution operation. This is done trough the Best Linear Unbiased (BLU) interpolation [1]. After this interpolation step (which has obviously been applied also to the original signal), the performance has been evaluated after the focused operation. Considering the non-uniform domain, the SQNR for the three possible approaches are reported in Figure 44, 45 and 46. By looking at the results it is possible to notice that the gain introduced by predictive is almost the same for the three considered strategies, namely 1β, 20β and 3β. In order to evaluate the difference between the three approaches, it is necessary to consider the SQNR gain, defined as (100), which is reported in Figure 47 the gain for the 1β case with respect to the direct quantizer and shows the same comparable result already obtained for the uniform domain (Figure 31). Figure 48 and 49 show the difference of SQNR between the 20β and 1β, and 3β and 1β, respectively. Even though the 1β approach leads to the most inaccurate estimation of the prediction, there is no significant loss with respect to the other investigated cases, which on the other hand require a larger complexity (i.e. a larger number of coefficient to be routed on board) for their implementation. It is then possible to conclude that for the non-uniform PRI case and assuming a variation up to $\pm 20\%$ from the $\overline{\mathrm{PRF}}$, the performance on raw data that obtained for equivalent to that obtained for the uniform domain PRI case by using only one weight for all the samples (i.e. the 1β case). Moving on to the interpolation section,

the performance has been evaluated in the same way by considering as reference signal the interpolated version of s on an uniform grid where the sampling period is determined by the inverse of the mean PRF. The result from this analysis are pictured in figure 50, 51 and 52. As expected, the performance are consistent after the whole processing chain, thus after the focusing operation. The SQNR on the focused data are reported in figure 53, 54 and 55 for the 1β, 20β and 3β respectively. As for the case of raw data, the gain is also reported for the focused signals in Figure 56, 57 and 58. This analysis applied on a general case of non-uniform domain with a large PRI variation (with respect to the staggered SAR case assumed for Tandem-L) shows a coherent gain. Three different solutions have been tested showing no reason to increase the complexity by considering the related autocorrelation value, and thus the weight, for each PRI variation. The equivalent performance for the uniform domain case has been achieved exploiting only the weight related to the mean value of the PRF.
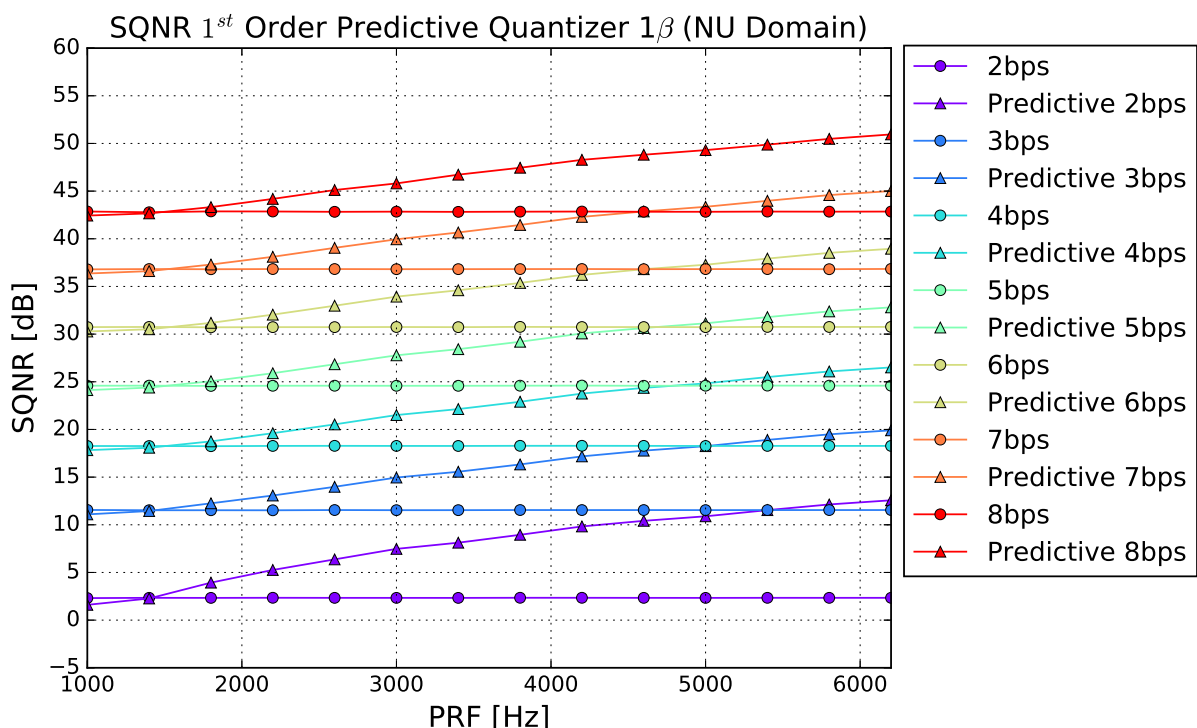
Figure 44: SQNR evaluated on raw data with non-uniform PRI for the direct and first order predictive quantizers with 1β as function of PRF for different uniform ADC rates.
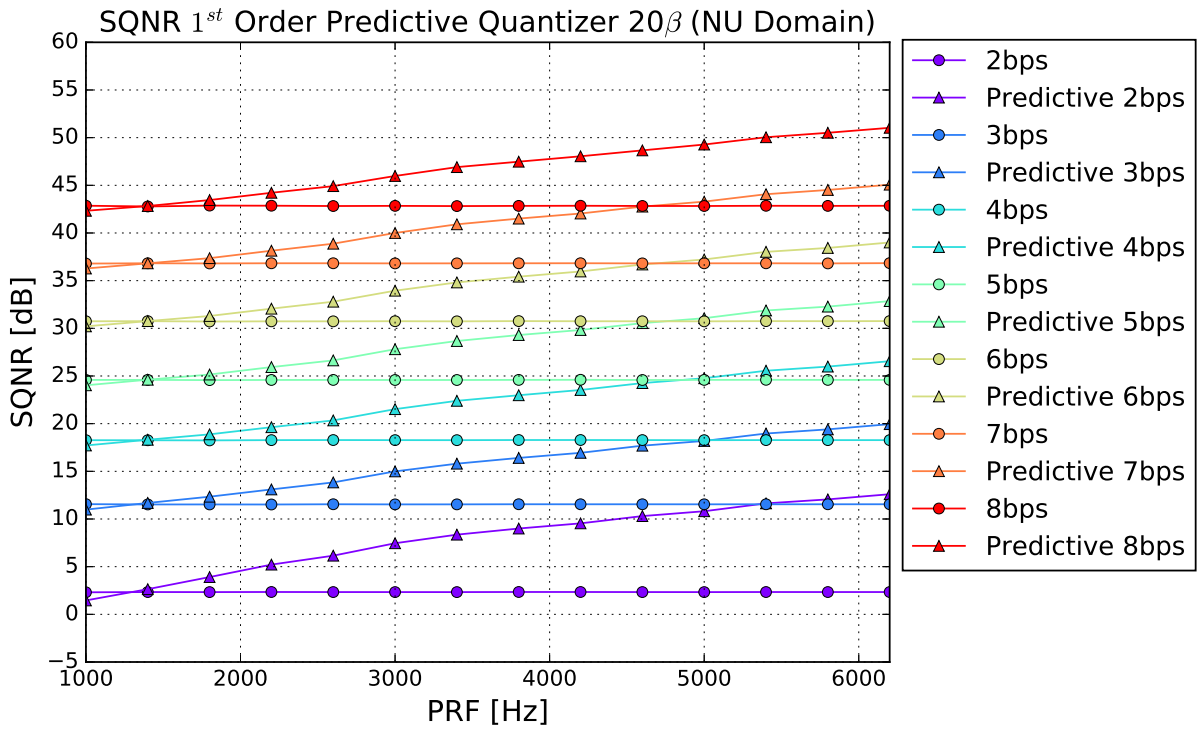
Figure 45: SQNR evaluated on raw data with non-uniform PRI for the direct and first order predictive quantizers with 20β as function of PRF for different uniform ADC rates.
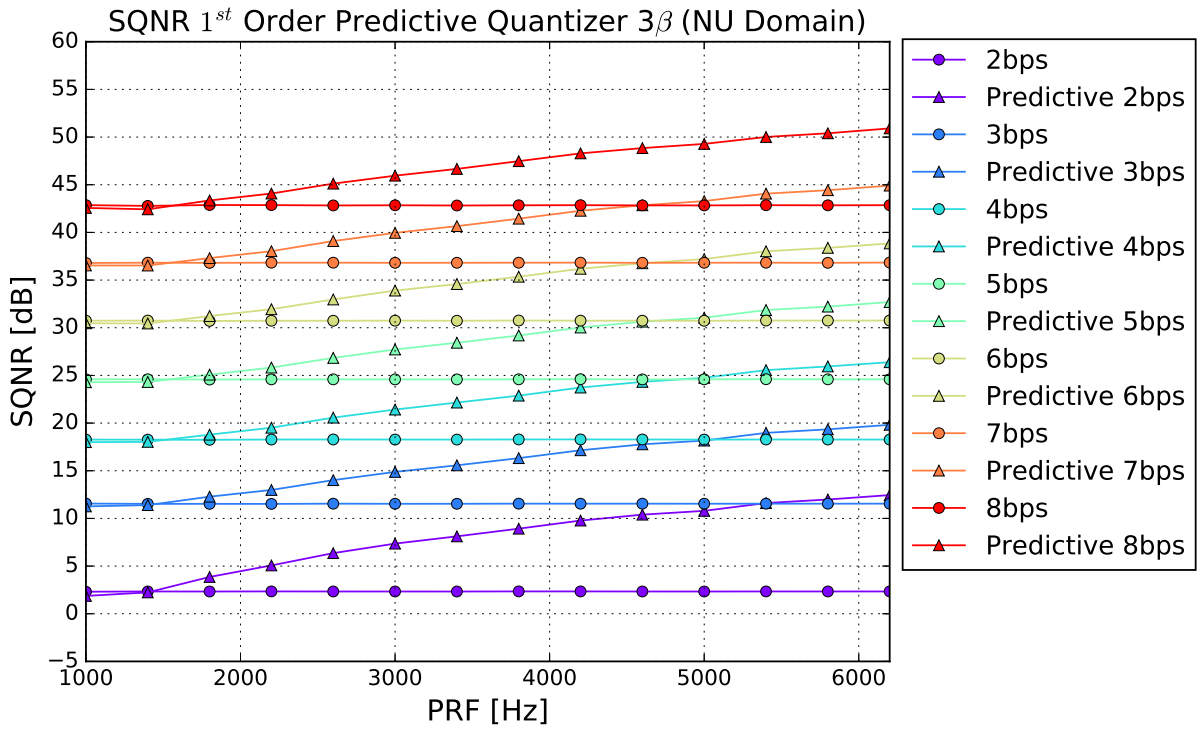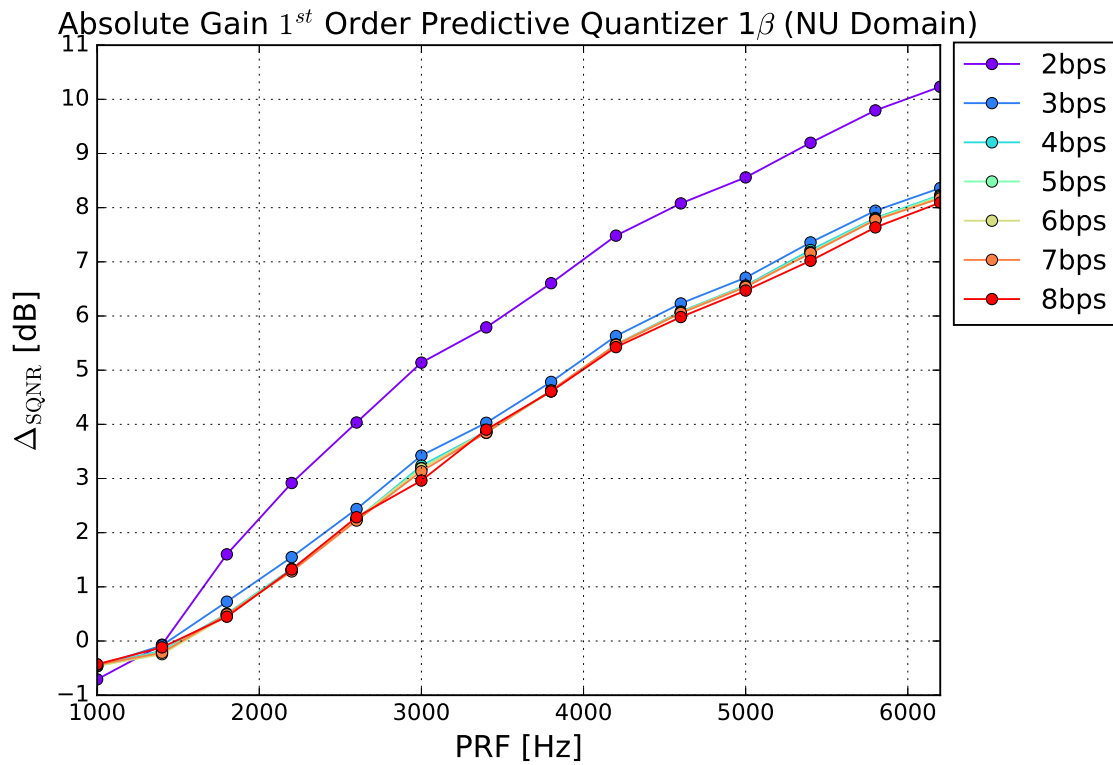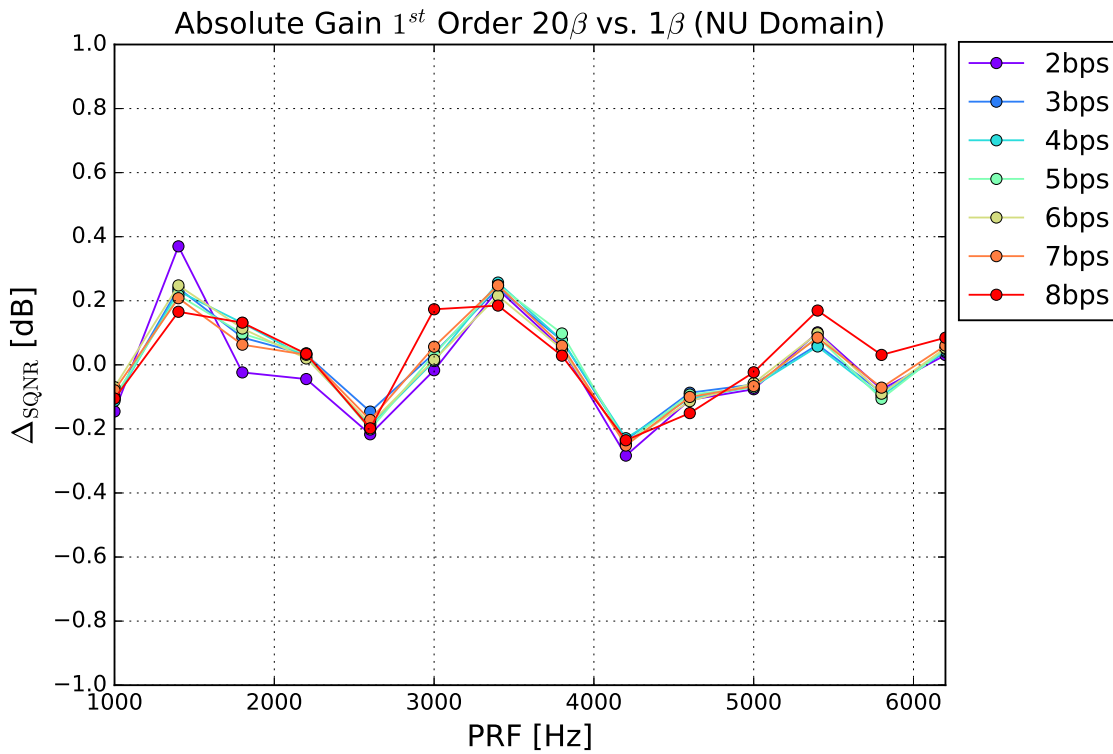

Figure 46: SQNR evaluated on raw data with non-uniform PRI for the direct and first order predictive quantizers with 3β as function of PRF for different uniform ADC rates.
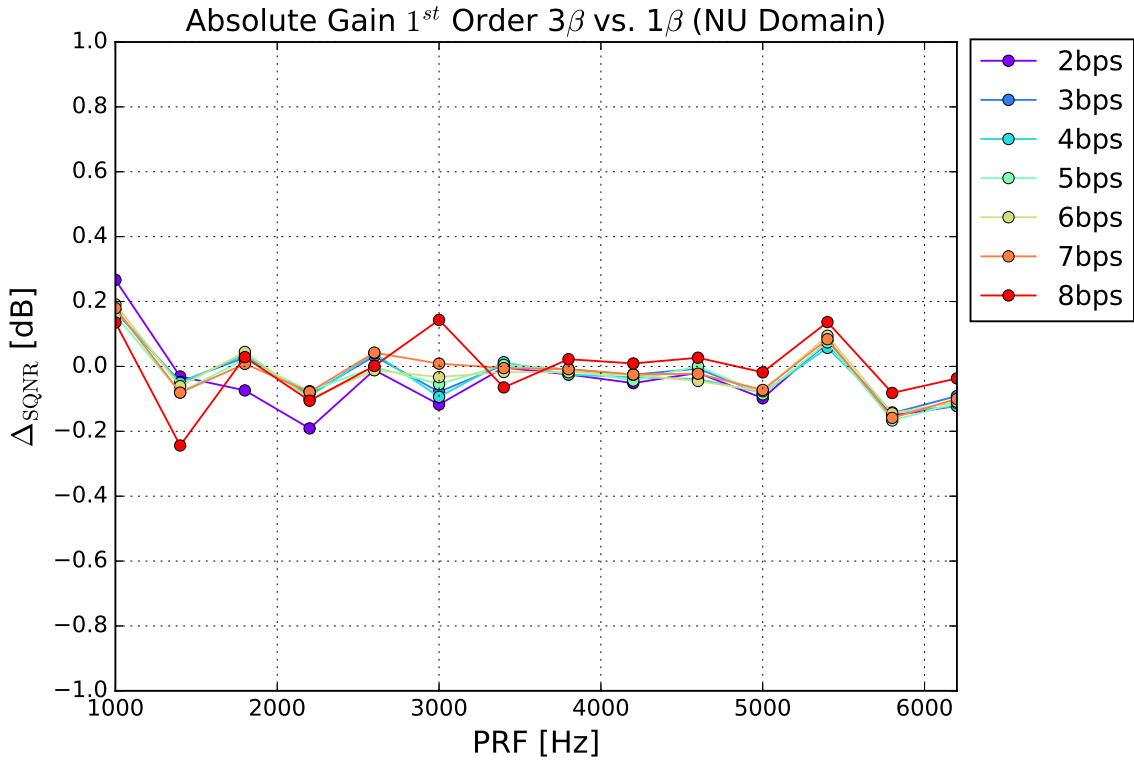
Figure 47: Gain evaluated on raw data with non-uniform PRI for the direct and first order predictive quantizers as function of PRF for different uniform ADC rates.
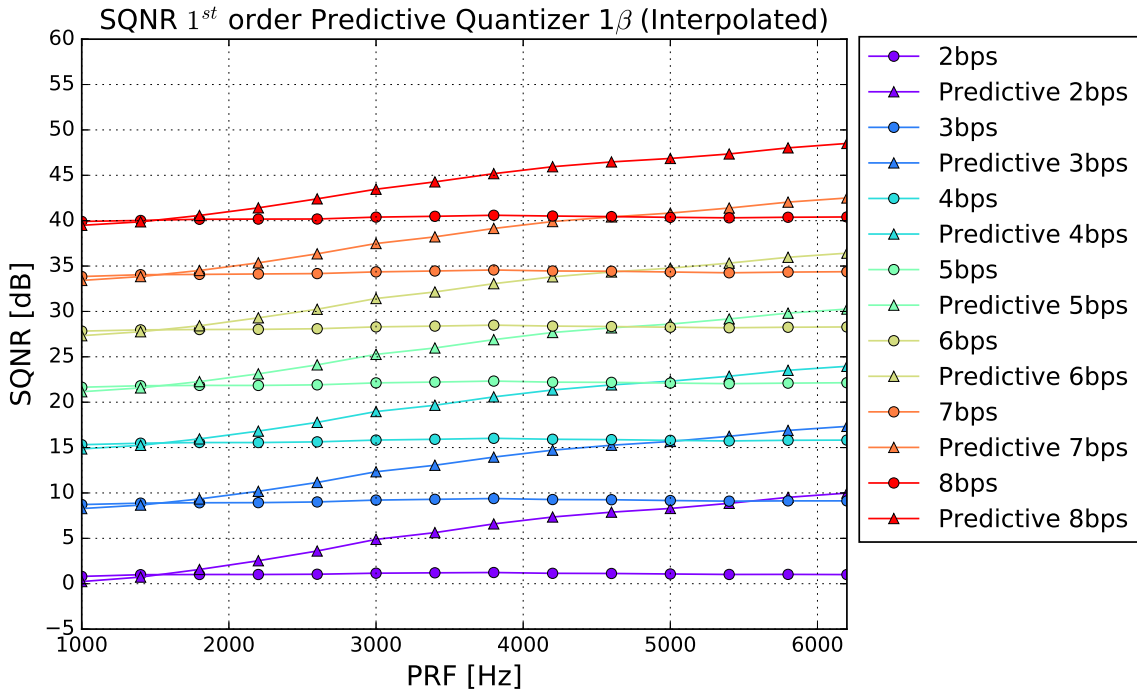

Figure 48: Gain evaluated on raw data with non-uniform PRI for the 20β and 1β first order predictive quantizers as function of PRF for different uniform ADC rates.

Figure 49: Gain evaluated on raw data with non-uniform PRI for the 3β and 1β first order predictive quantizers as function of PRF for different uniform ADC rates.

Figure 50: SQNR evaluated on interpolated data with non-uniform PRI for the direct and first order predictive quantizers with 1β as function of PRF for different uniform ADC rates.
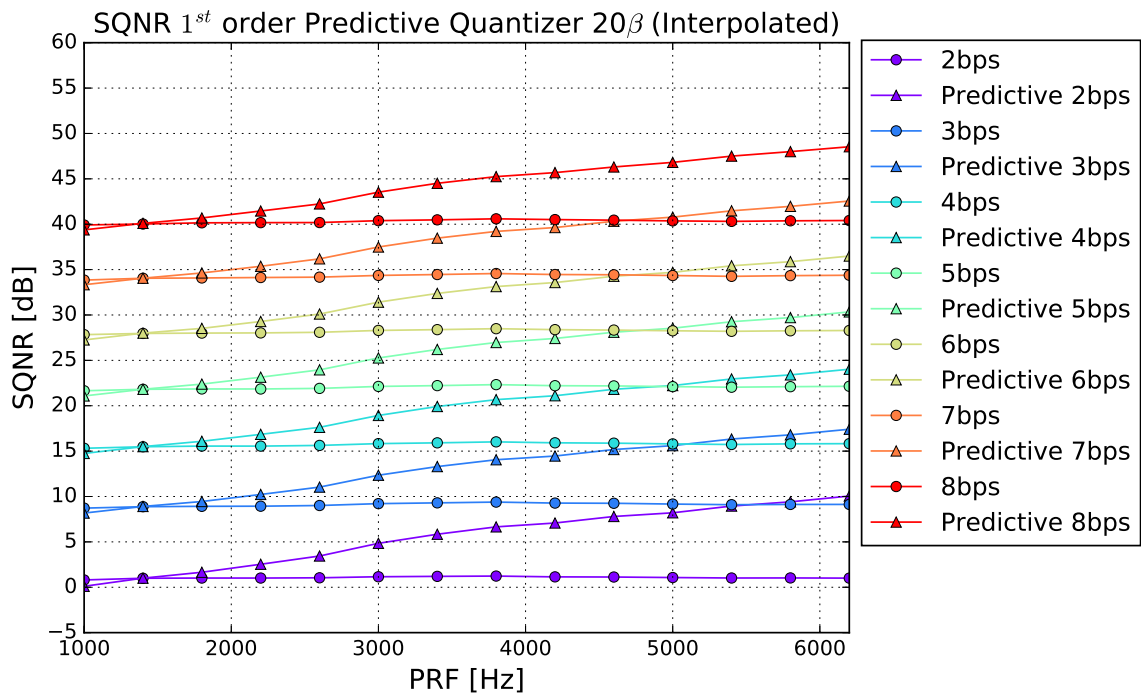
Figure 51: SQNR evaluated on interpolated data with non-uniform PRI for the direct and first order predictive quantizers with 20β as function of PRF for different uniform ADC rates.
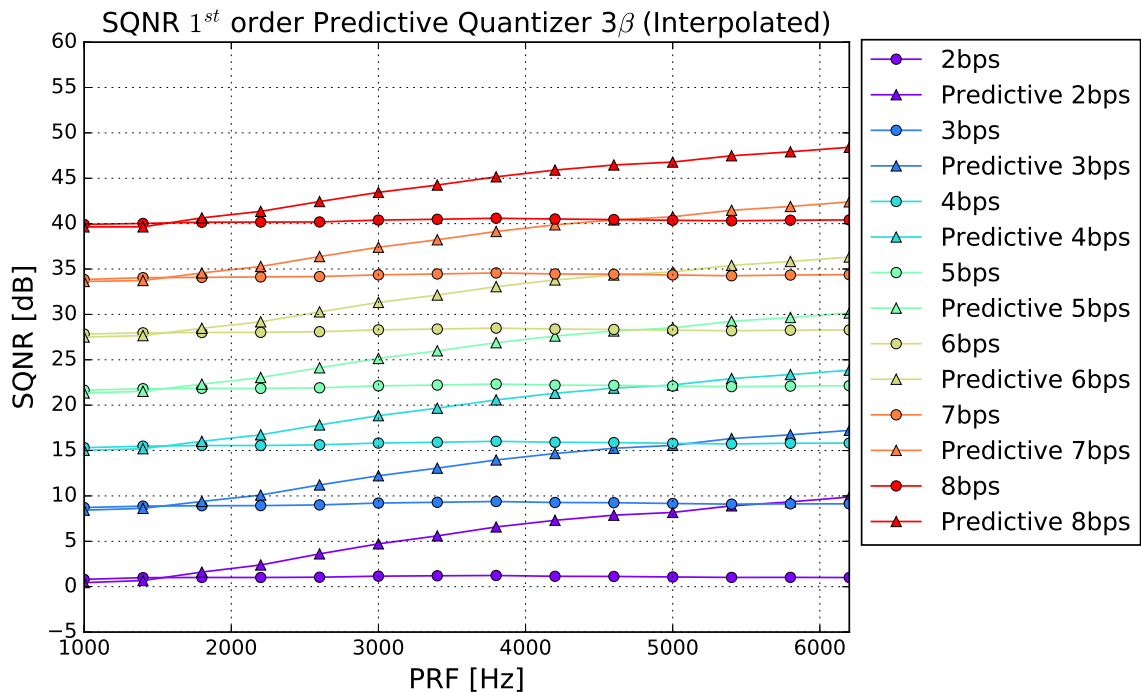

Figure 52: SQNR evaluated on the interpolated data with non-uniform PRI for the direct and first order predictive quantizers with 3β as function of PRF for different uniform ADC rates.
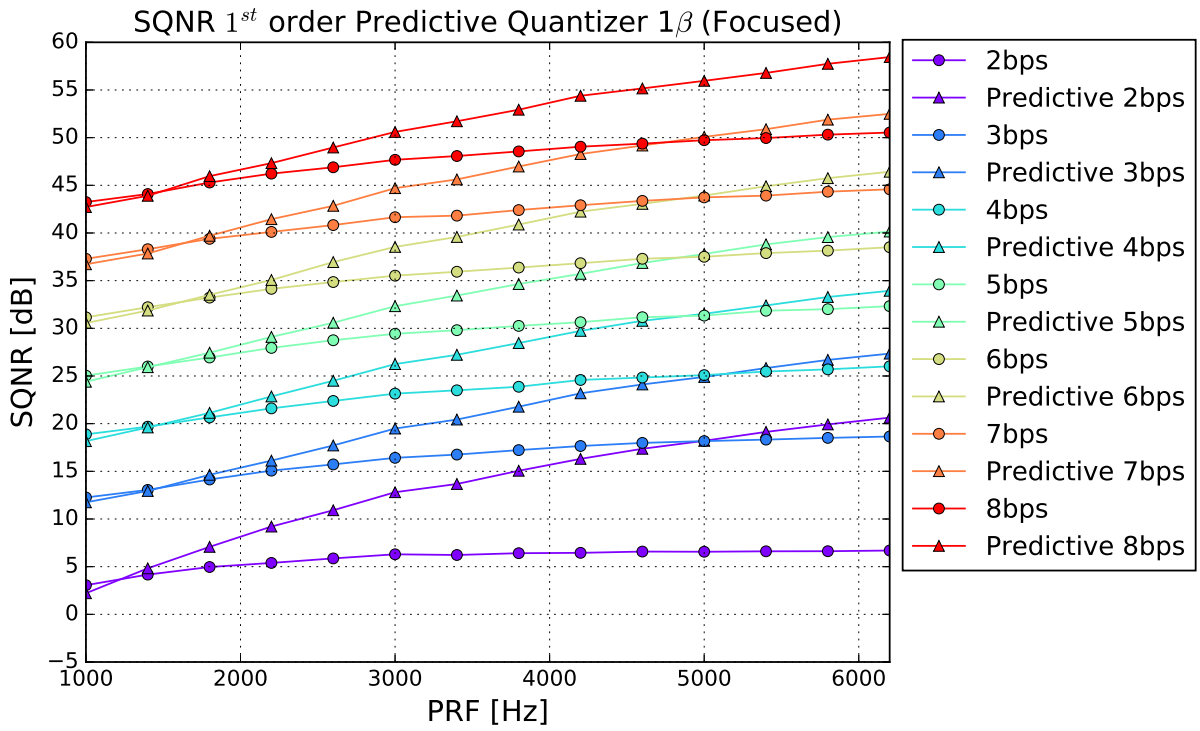
Figure 53: SQNR evaluated on focused data with non-uniform PRI for the direct and first order predictive quantizers with 1β as function of PRF for different uniform ADC rates.
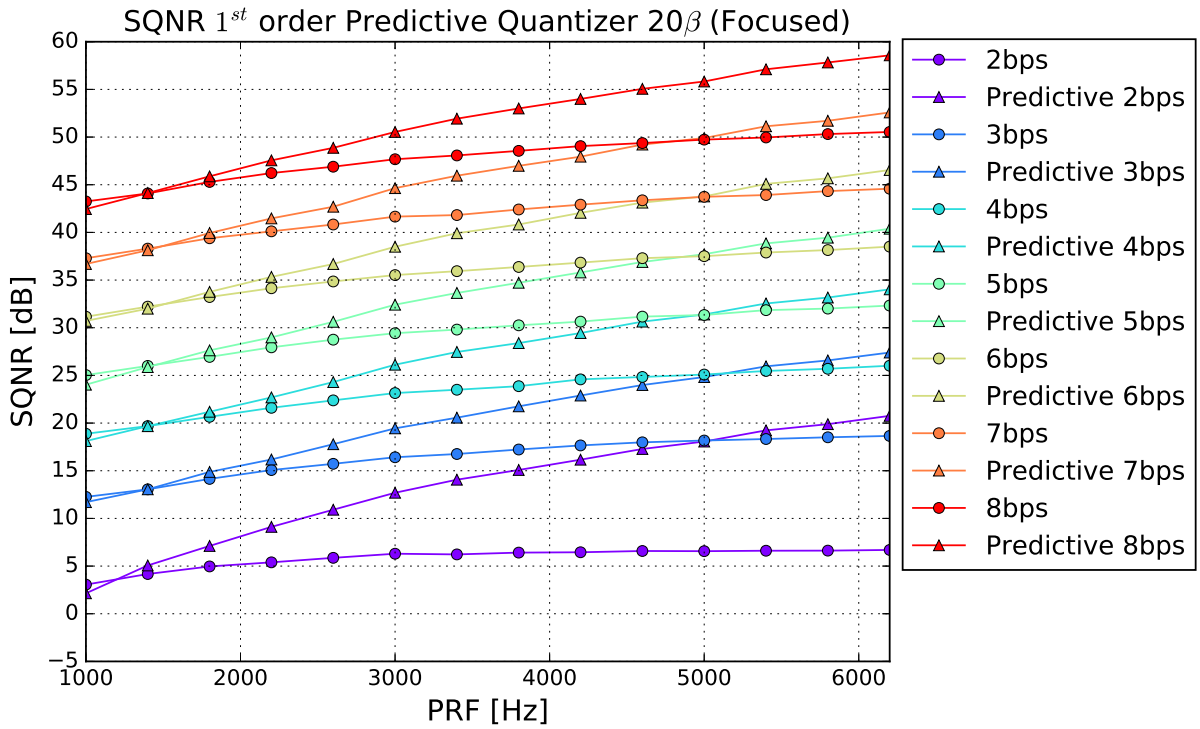

Figure 54: SQNR evaluated on focused data with non-uniform PRI for the direct and first order predictive quantizers with 20β as function of PRF for different uniform ADC rates.

Figure 55: SQNR evaluated on focused data with non-uniform PRI for the direct and first order predictive quantizers with 3β as function of PRF for different uniform ADC rates.

Figure 56: Gain evaluated on focused data with non-uniform PRI for the direct and first order predictive quantizers as function of PRF for different uniform ADC rates.
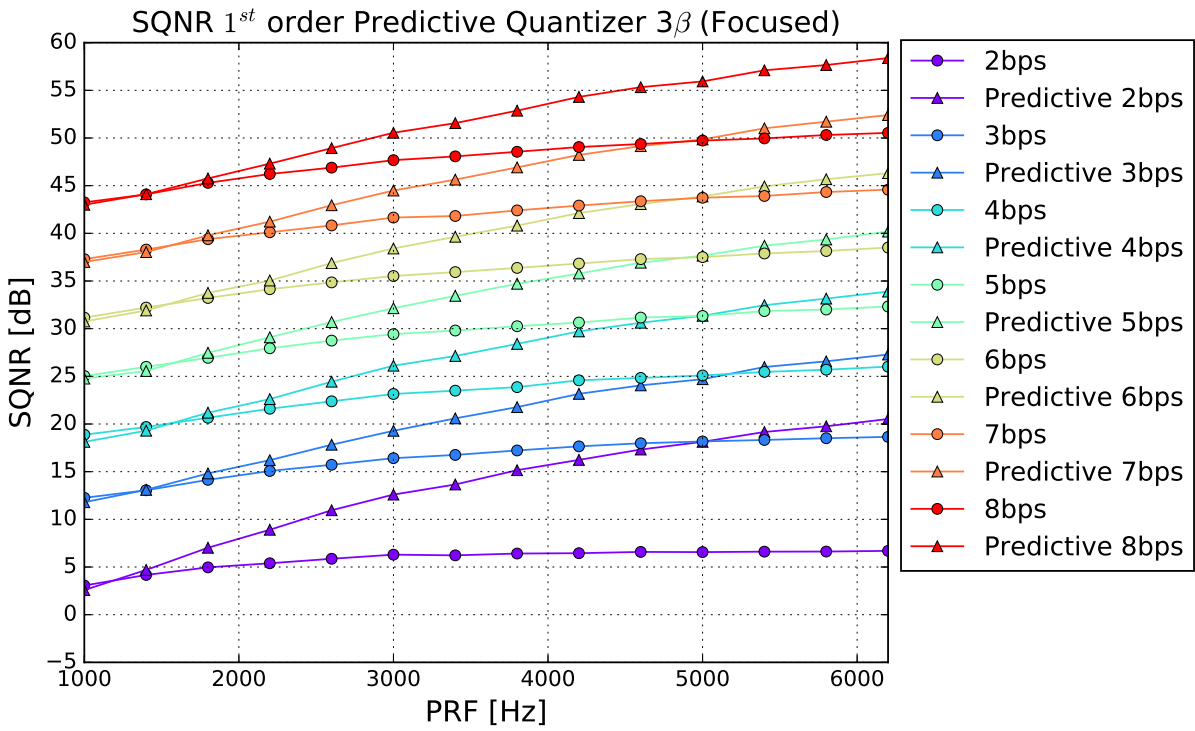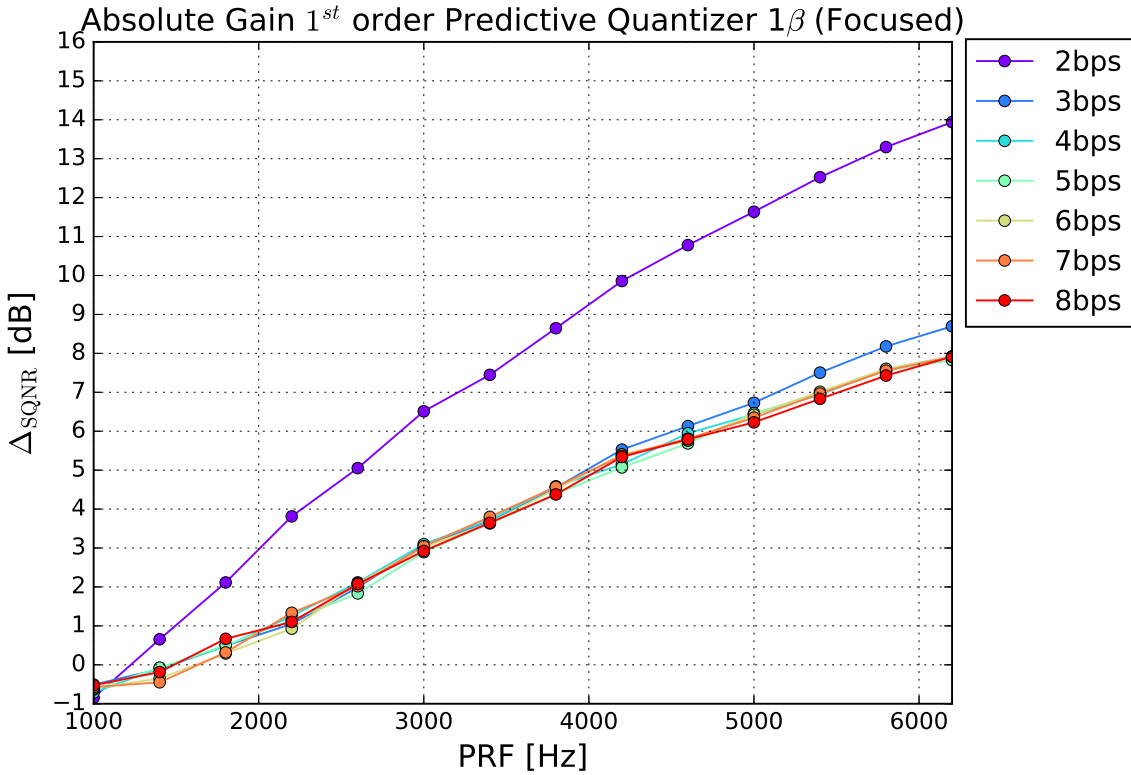
Figure 57: Gain evaluated on focused data with non-uniform PRI for the 20β and 1β first order predictive quantizers as function of PRF for different uniform ADC rates.

Figure 58: Gain evaluated on raw data with non-uniform PRI for the 3β and 1β first order predictive quantizers as function of PRF for different uniform ADC rates.
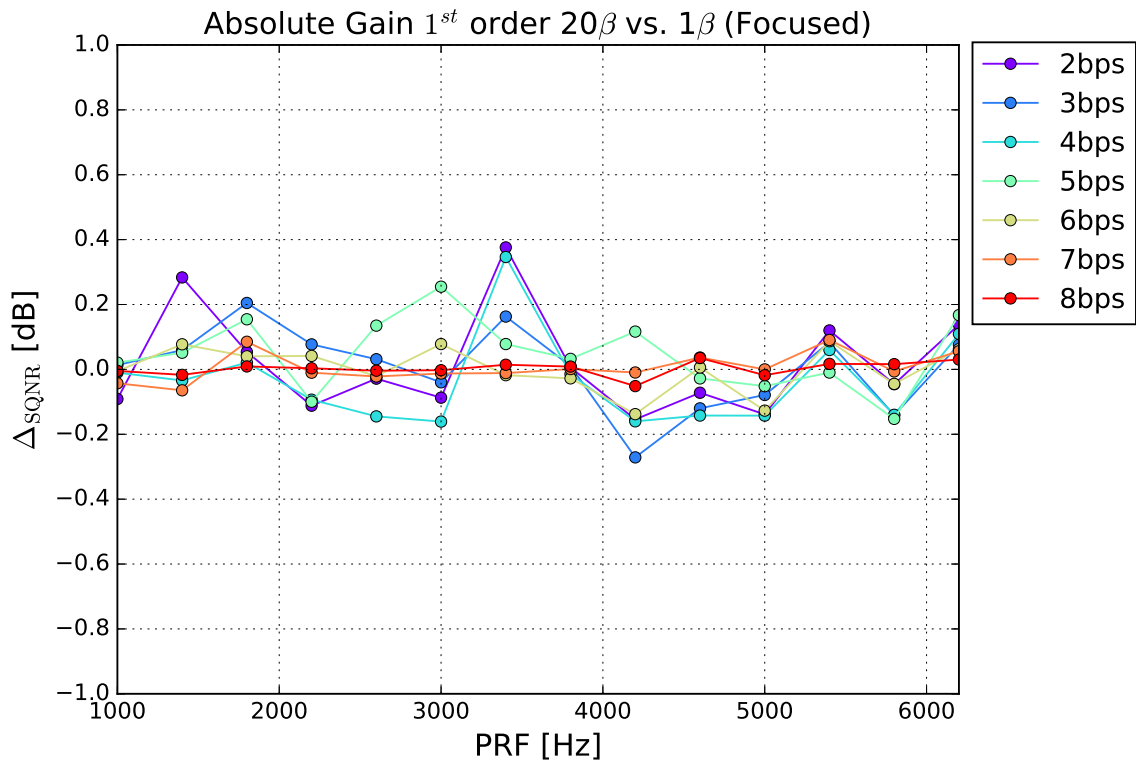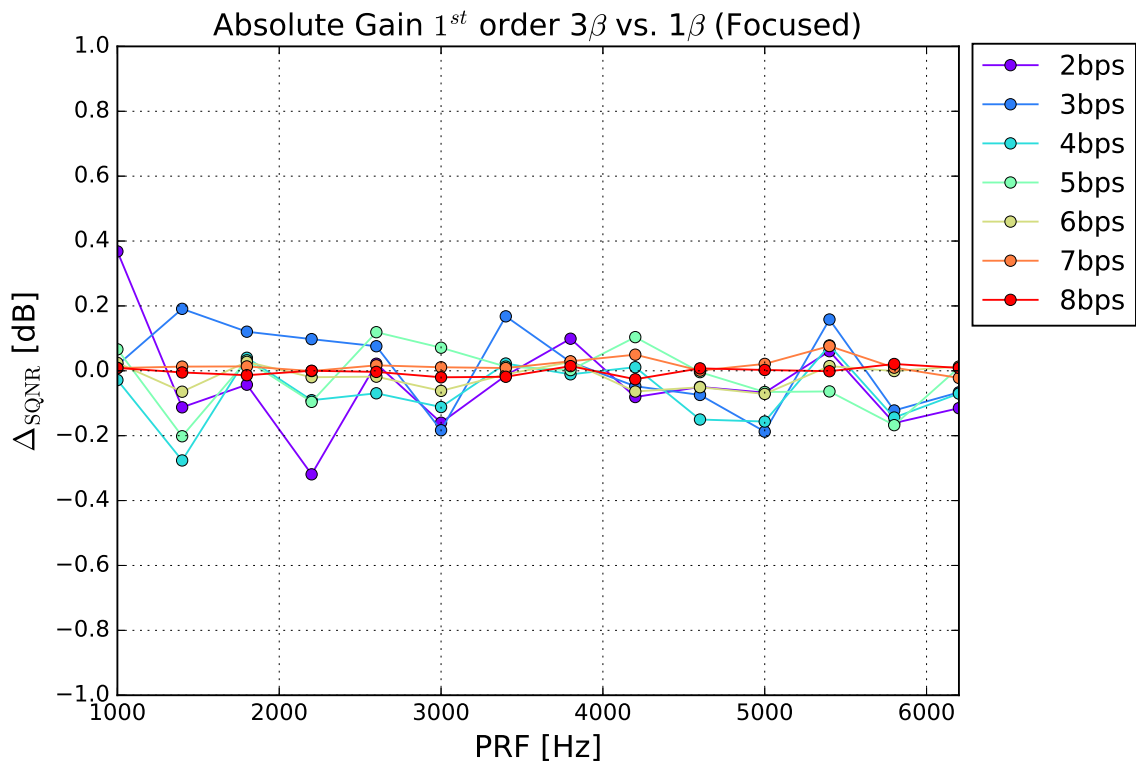
6.3 Staggered SAR for Tandem-L

In the previous section the proposed method to implement data reduction by means of linear predictive coding and quantization has been tested on a set of different PRFs and bitrates. Here we focus on the specific Tandem-L case, and for this the considered simulations have been carried out by considering the Tandem-L $\overline{PRF}$ only, which corresponds to 2700 Hz. As an example of PRI variation, the one pictured in Figure 59 has been considered. This PRI pattern is different from the one considered in the previous case both for variation boundary, which is now $\pm 8\%$ with respect to $\overline{PRF}$ and for number of variation per cycle, which for this case is of 233. The pattern of variation is specifically designed in order to have always a sample before and after a gap, in order to be able to recover the lost information by opportune interpolation [21]. Being the PRI variation different from the previous case, the same evaluation of the non-uniform case has been carried out for the first order predictor. The proposed solutions are again the less complex one defined as 1β, i.e. one single weight is employed for prediction for all the 233 PRI variations, and the more precise one defined as 233β. The variations with respect to the value related to the $\overline{PRF}$ is reported in figure 60a and are represented by the blue and red curves, respectively. Considering that the variation boundary is lower than the previous case, also the α values are part of the solution: while considering the 1β solution, also 1α has been considered; on the other option, 233 α have been considered. The α variation with respect to the one related to the $\overline{PRF}$ is pictured in Figure 60b, again in blue and red respectively, showing a noisy behaviour with respect to the β variation. This is because the α value is related to the standard deviation of the input signal, which in turn may show slightly varying values around the nominal one. The result of the evaluation between the two solutions is pictured in Figure 61, where it is possible to see that the 233β, 233α case performs better of the 1β, 1α by a minimal amount. This difference is in the order of 0.1 dB, leading to the confirmation of the result achieved in Section 6.2 also for the α value, hence allowing also for the specific Tandem-L configuration the use of a single coefficient for the complete set of considered PRI. Having proved the performance for the Tandem-L case to be comparable to those obtained for the uniform PRI case, the next step is to consider a BAQ in place of the uniform quantizer (ADC) which has been considered for the previous simulations. The prediction scheme for encoding is then considered as in Figure 62.

The only difference with the monodimensional case is that now $s[n]$ represents a range line. Since BAQ operates in blocks of 128 range samples, the pictured scheme is applied to 128 azimuth lines together. Once the difference from the block and its estimation is retrieved, the BAQ operates as described in Section 4.1.2, optimizing the quantization to the statistics of the block. It is worth highlighting that, being each raw data sample a realization of a normally distributed variable, the random variable resulting from the difference between the sample and a weighted sum of the N preceeding realizations (each one being normally distributed) has still a normal distribution, hence making a Max-Lloyd quantizer such as the BAQ suitable for the resulting raw data quantization. The joint operation of BAQ and LPC is a novel technique named Predictive-BAQ (PBAQ). The decoding process is done coherently as pictured in Figure 63. Having defined the prediction parameters and the BAQ implementation in the encoding and decoding process, it is necessary to generate the bidimensional non-uniform raw data. By proceeding azimuth line per azimuth line following the metodology reported in Figure 42, it is possible to
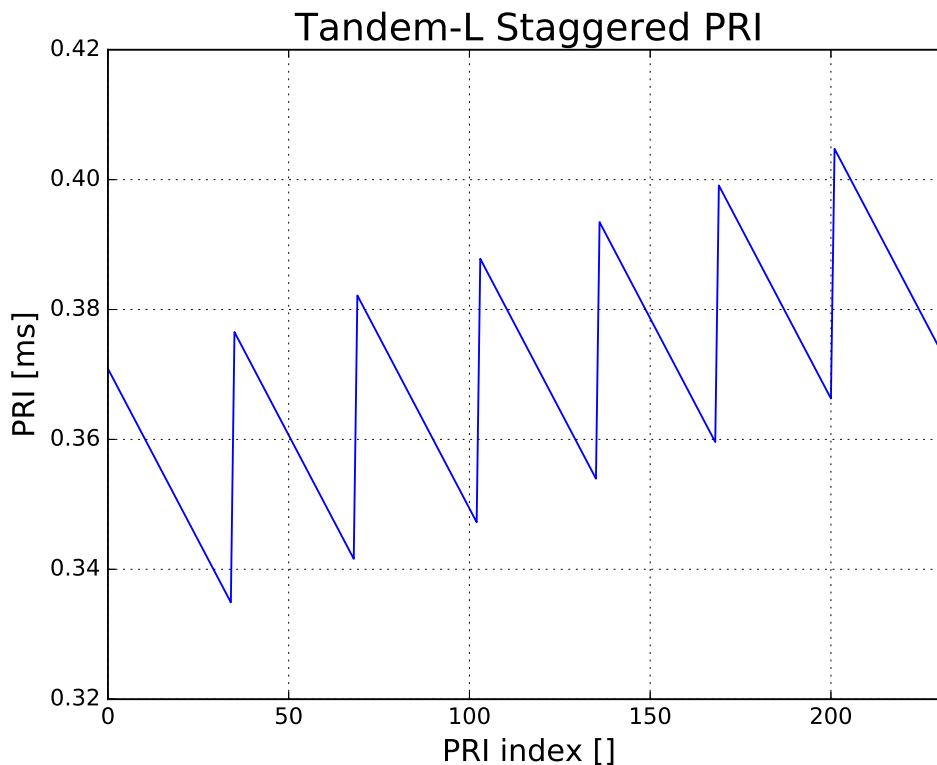
Figure 59: PRI variation for the selected case of Staggered PRI for Tandem-L.

obtain a non-uniform raw data which has been defocused only in the azimuth dimension. In order to have a coherent raw data generation, the (uniform) transmitted chirp is convoluted for each range line, giving the non-uniform azimuth compressed bidimensional raw data. Having defined all the parameters which must be taken into account, it is possible to summarize the processing chain, which is pictured in Figure 64. As for the previous investigations, the results calculated on the raw date are pictured in Figure 65, where the SQNR is shown as function of the order of prediction for different bitrates. For this case the "Direct" results refer to the application of BAQ on the uncompressed signal. This is done for having a fair comparison between the standard BAQ scheme and the proposed Predictive BAQ. After the interpolation operation, the SQNR has been calulated once again, showing no significative difference in terms of performance as pictured in Figure 66. The evaluation on the whole processing chain is finally reported in Figure 67. Here it is possible to see that as for the uniform case, the third order predictor gives a gain of 4 dB with respect to the direct BAQ quantizer. Having proved the gain for the Tandem-L specific case, the data reduction evaluation is performed in the following Section, where fractional bitrate is taken into account.
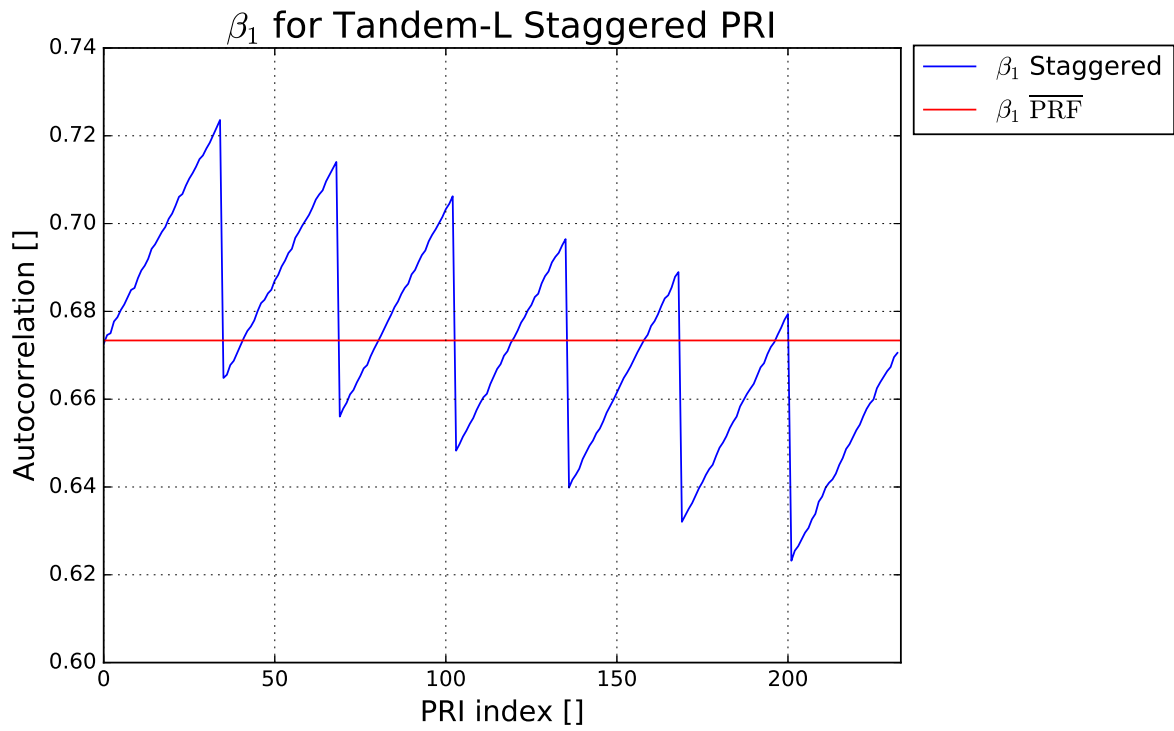
(a) Autocorrelation
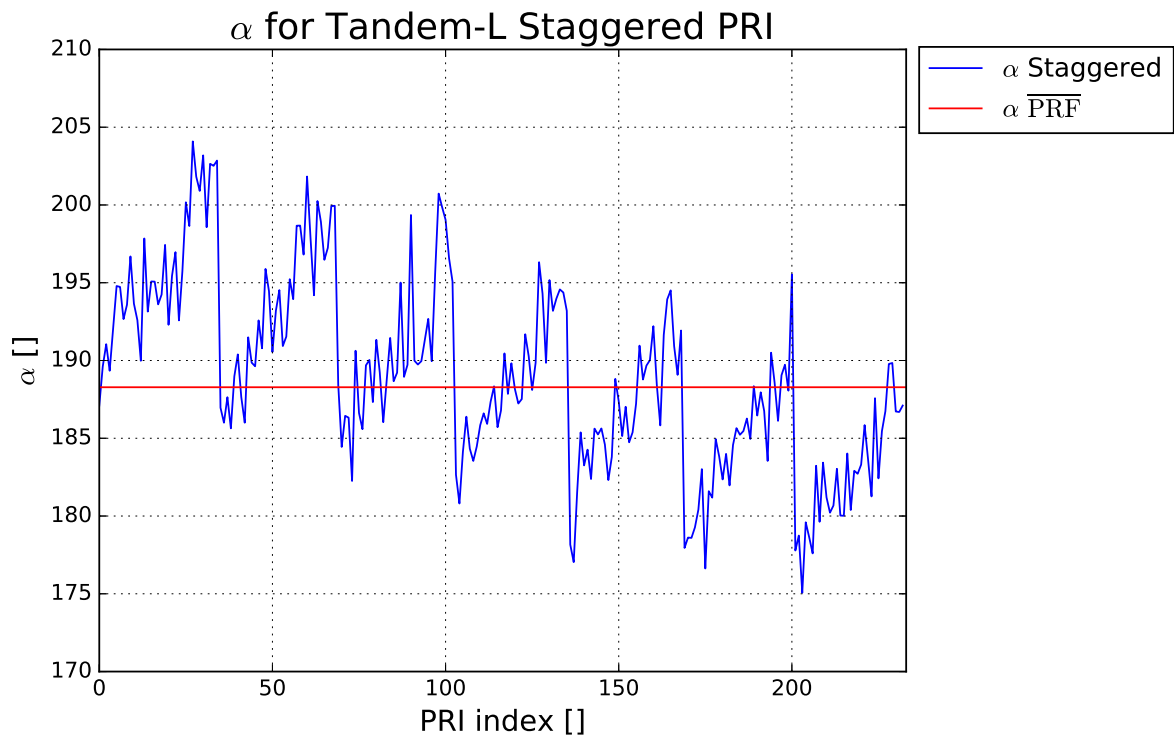
(b) Scaling Factor

Figure 60: Behaviour of predictive coding parameters for the considered case of staggered PRI for Tandem-L.
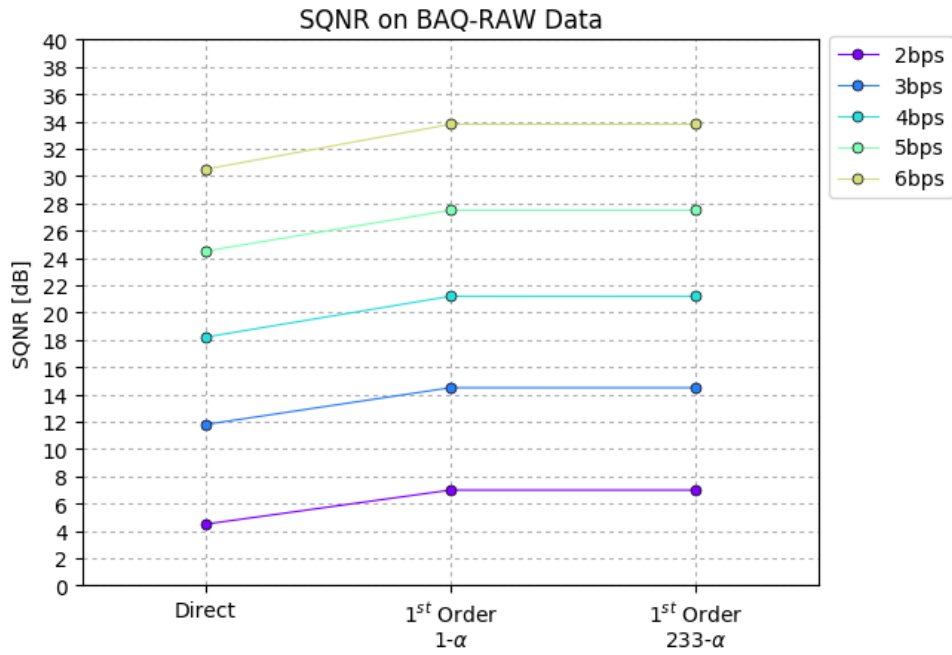
Figure 61: Comparison between the two approaches to the staggered PRI for Tandem-L: one exploiting a single coefficient for prediction (1β) and the other taking into account all the variations (233β).

Figure 62: Predictive quantization encoding flow scheme.
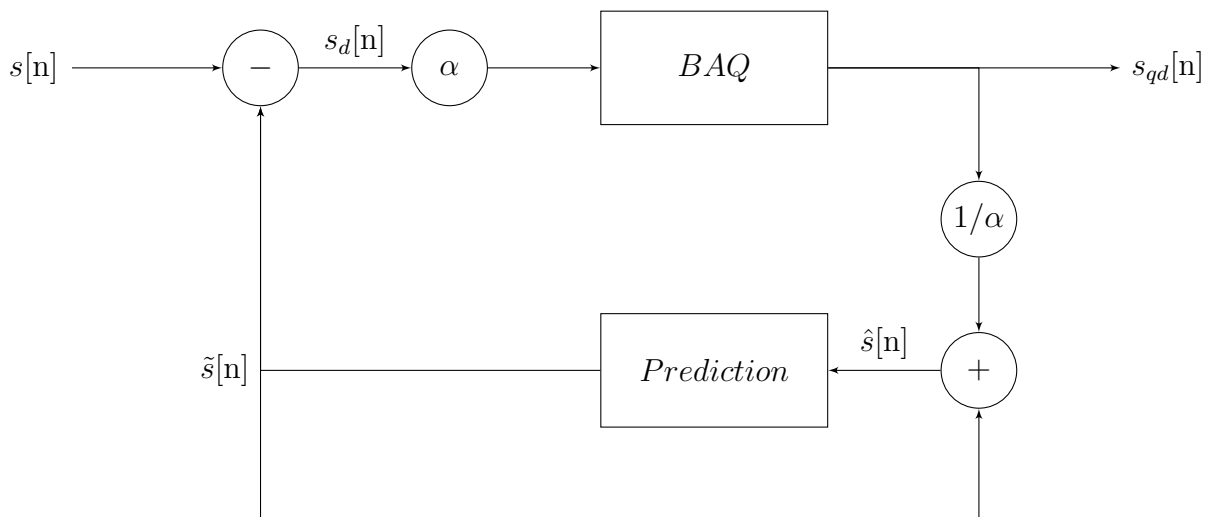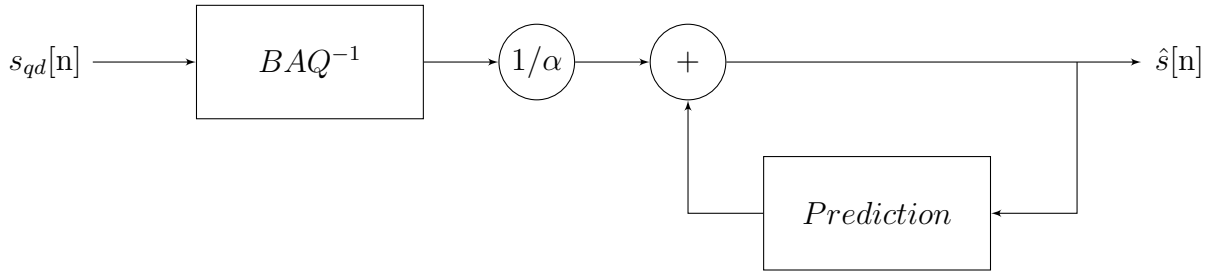
Figure 63: Predictive quantization decoding flow scheme.

Figure 64: Processing chain for 2-dimensional Tandem-L simulation scenes and their comparison.

Figure 65: SQNR calculated on raw data at different orders of Predictive BAQ on a distributed target.

Figure 66: SQNR calculated on interpolated data at different orders of Predictive BAQ on a distributed target.

Figure 67: SQNR calculated on focused data at different orders of Predictive BAQ on a distributed target.

6.3.1 Optimum Bit Allocation

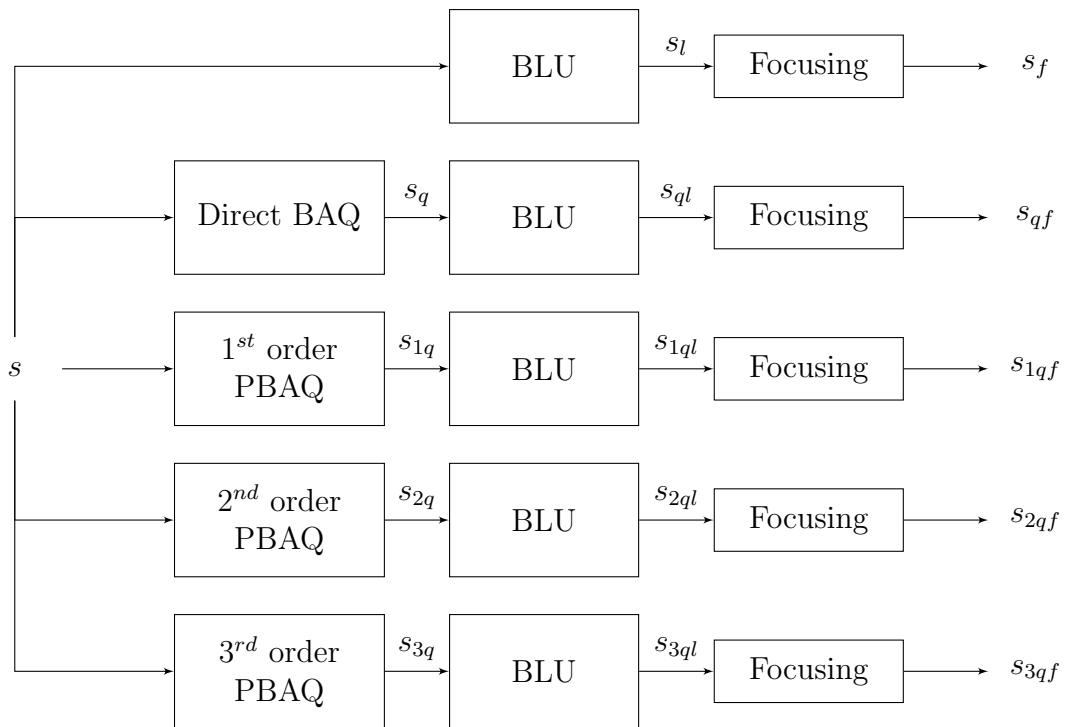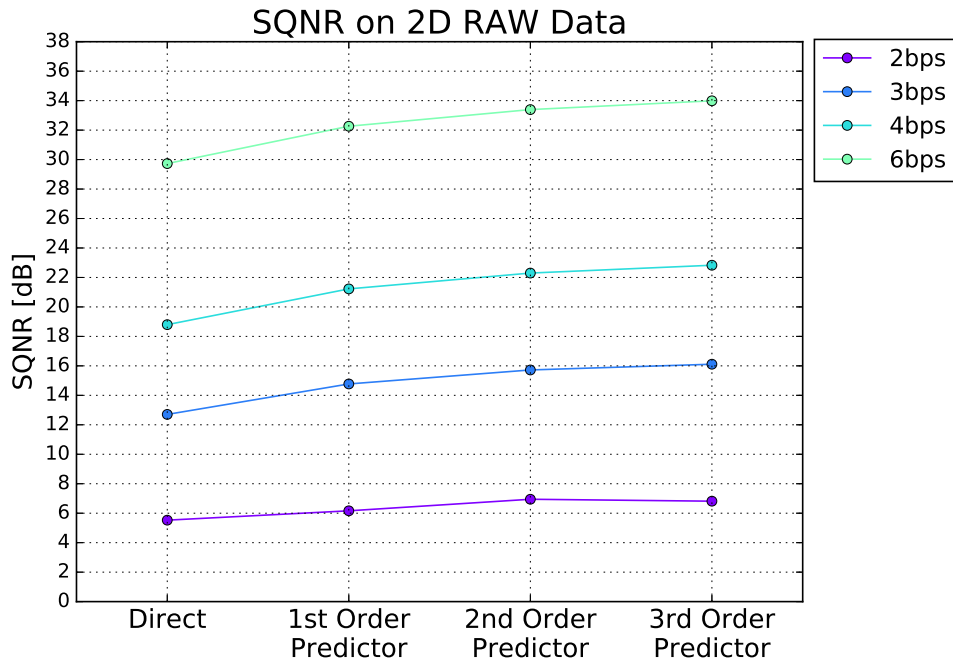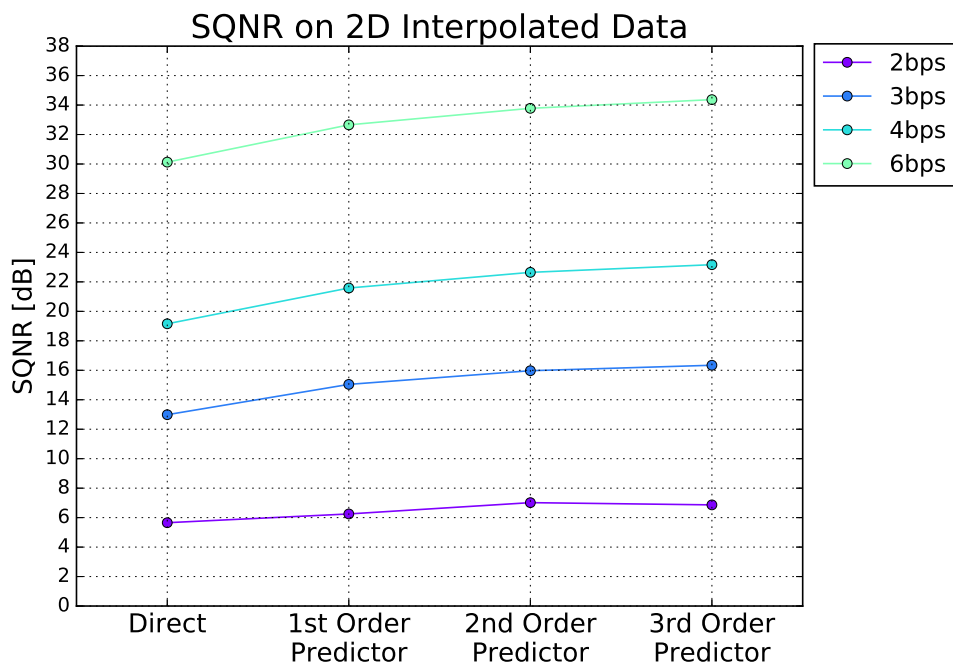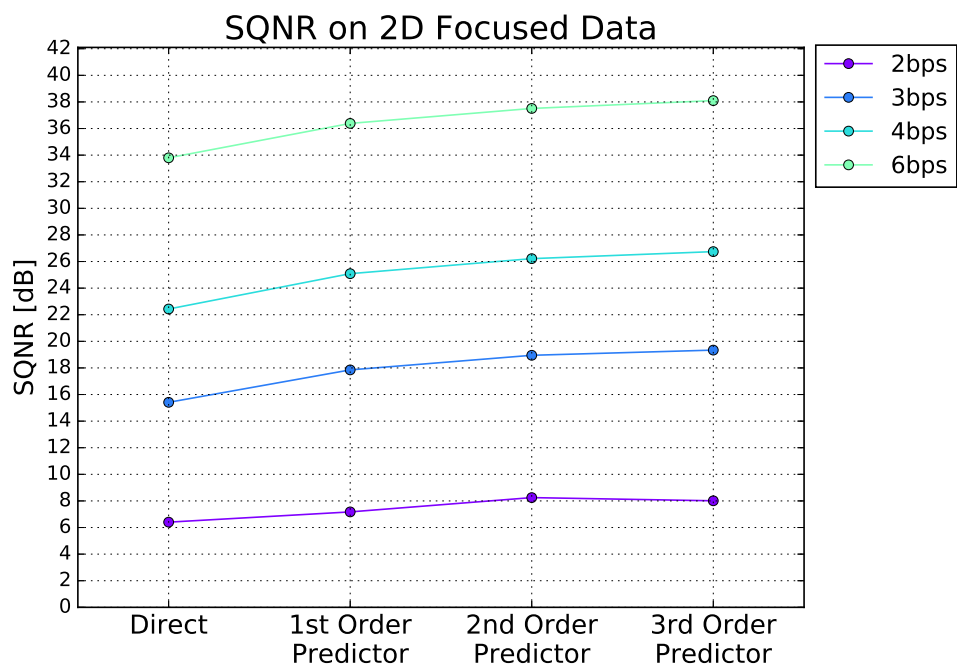The results presented in the previous Section confirm the theoretical expectation in the uniform case. The objective of the work is to present an onboard compression technique to reduce the data volume to be stored on board. As introduced in (54), as an example, a gain of 6 dB allows to achieve the same SQNR performance by employing one bit less. Since the presented results are showing a gain of 4 dB in the best case, it is not possible to use one bit less, since SQNR performance will be no longer in line with the system constraints. To achieve the performance of the 4 bits/sample direct BAQ, it is necessary to implement an azimuth-switched quantization (ASQ) [14], which allows to exploit fractional bitrates. ASQ operates varying the bitrate for each range line by coherently alternating 4 and 3 bits per samples (in this case), such as the overall mean is a fractional number between 3 and 4. After the focusing operation the different quality of representation between samples will be uniformly spread on the whole data, giving a uniform fractional bitrate for every sample. Four different fractional bitrates have been considered: 3.2, 3.4, 3.6 and 3.8. The application of azimuth-switched predictive block adaptive quantization is pictured in Figure 68. The present result shows that the SQNR
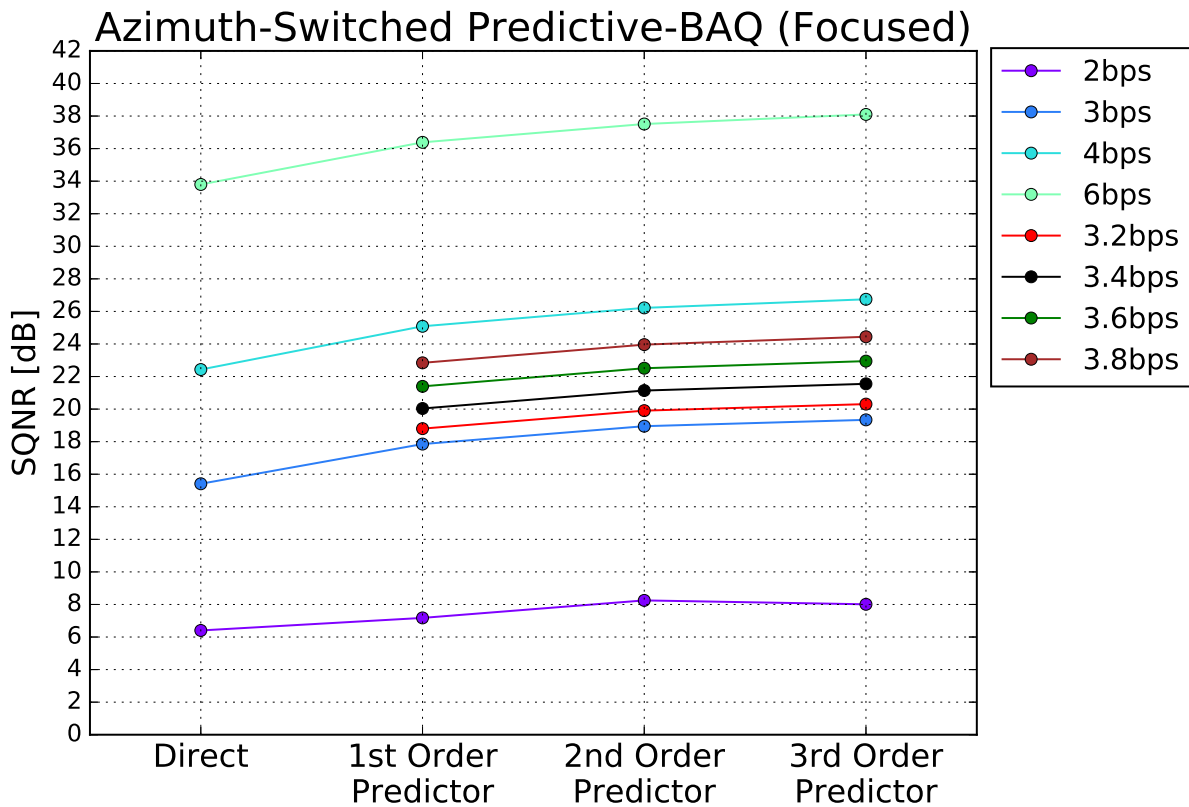
Figure 68: SQNR calculated on focused data at different orders of Predictive BAQ exploiting fractional bitrate on a distributed target.

for approximately 3.5 fractional bitrate is equivalent to the SQNR of the direct BAQ at 4 bits per sample. This means that the presented technique has the same performance of the direct BAQ using half a bit less. To evaluate the actual data reduction performance, the following equation shows the percentage of data reduced with the Predictive BAQ

quantization technique

$$\text{PBAQ}_{dr} = \frac{3.5}{4} = 12.5\% \tag{101}$$

i.e. a data reduction of about 12.5% (with respect to the BAQ direct case) can be achieved using the proposed method based on Predictive Quantization.

6.3.2 Analysis on a Space Varying Scene

All the previous analysis have been executed assuming a distributed target. What happens in real situations is the mixture of distributed and point scatterers hence showing a variation of backscatter intensity, causing clipping error in quantization step. BAQ adapts the quantization on the block statistics, limiting the impact of this errors. Moreover, the block-based approach limits the impact of high backscatter difference. In order to evaluate the performance of the proposed technique on a realistic scene, a specific case of lower scatterers suppression has been considered. The raw data generation has been performed with the same technique used in Section 6.3. To simulate a strong and a low scatterers in close vicinity, the normal distributed process along the azimuth domain is considered as the concatenation of two processes with different variance

$$n = \{v, w : v \in n_1, w \in n_2\} \quad where \quad \begin{aligned} \Re\{n_1\}, \Im\{n_1\} \sim \mathcal{N}(0, \sigma) \\ \Re\{n_2\}, \Im\{n_2\} \sim \mathcal{N}(0, \sigma\sqrt{10}) \end{aligned} \tag{102}$$

The $\sqrt{10}$ factor has been chosen to produce a 10 dB power difference between the two distributions. The energy of the process is pictured in Figure 69, where the plot is considered in the neighborhood of the middle of the azimuth dimension, where the response of the two, the strong and the low scatterer, sensitively overlap in the raw data domain. It is possible to notice the 10 dB "jump" in the transit sample from the high backscatter area to the lower one, which has been averaged along each azimuth line. In order to describe the performance of the system as the lower scatterer effect is introduced, the SQNR has been evaluated as a function of the range line (Figure 70). The decrease of performance is due to the quantization parameters, which are set on the higher backscatter profile. As the satellite moves, the BAQ adapts the quantization to the local dynamic of the signal, and this results in a better reconstruction of the stronger target, whereas the weak one is heavily distorted samples in the vicinity of the discontinuity [6][15]. This effect is peculiar of the SAR acquisitions, and visible only after processing. The proposed method shows the same behaviour of the direct BAQ. Even though the low scatterer suppression lowers the performance in the neighborhood of the "Jump", the overall SQNR is still coherent with the previous results (e.g. see Figure 71).

Figure 69: Backscatter profile averaged on the range line for the "Jump" target simulation.

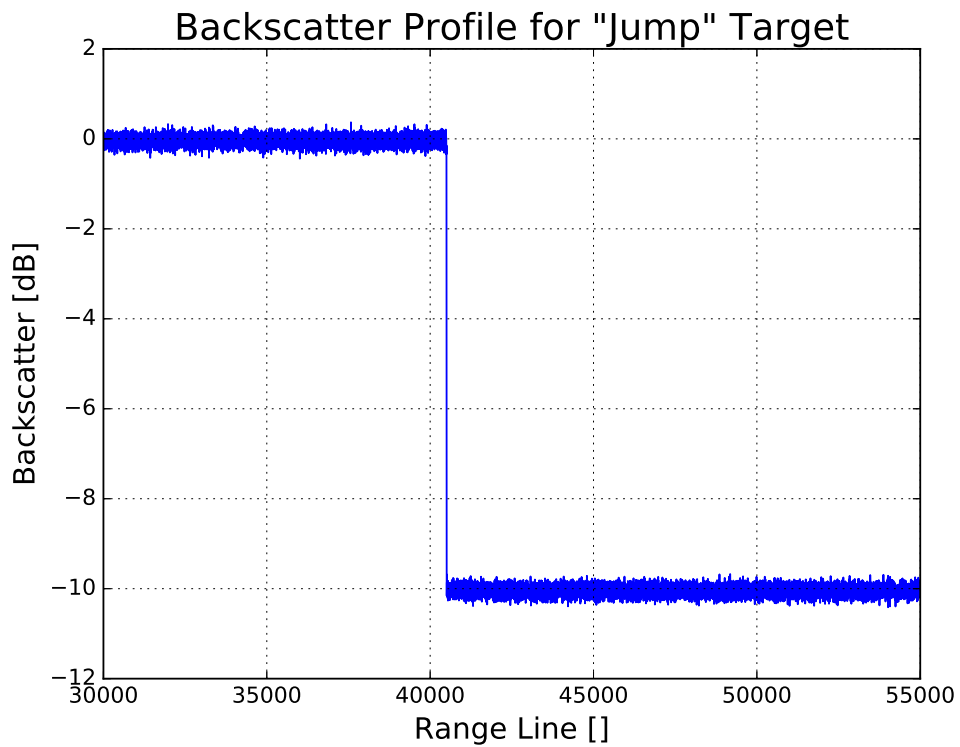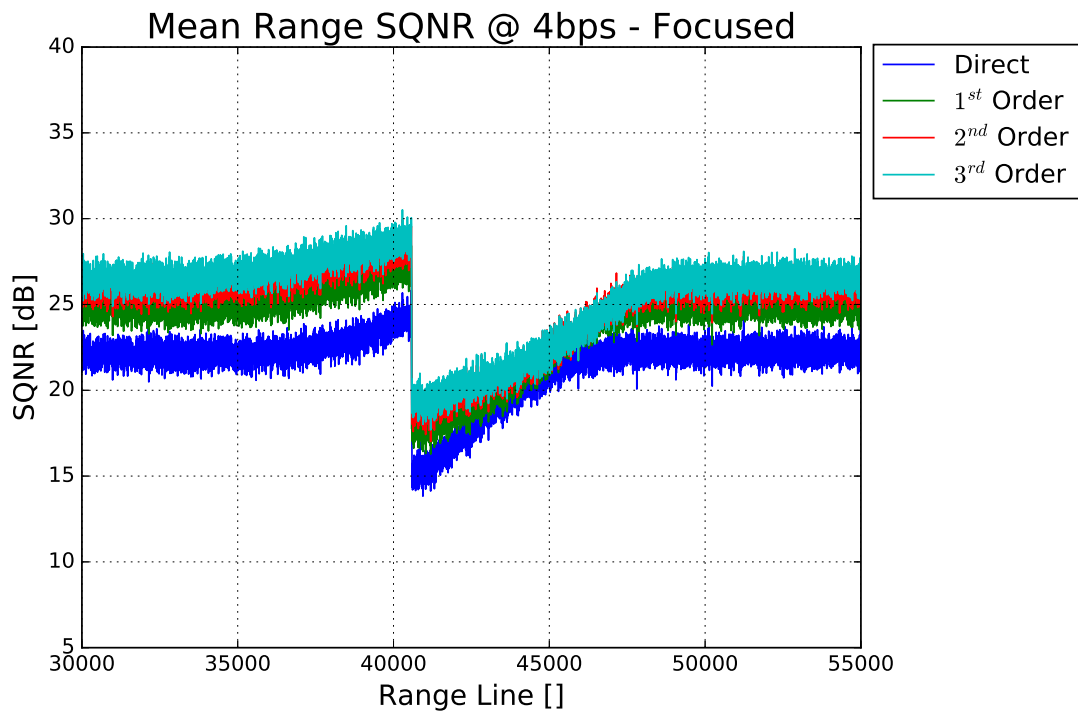

Figure 70: SQNR calculated on focused data at different orders of Predictive BAQ as function of range line on a "Jump" target. The SQNR has been averaged for each range line.
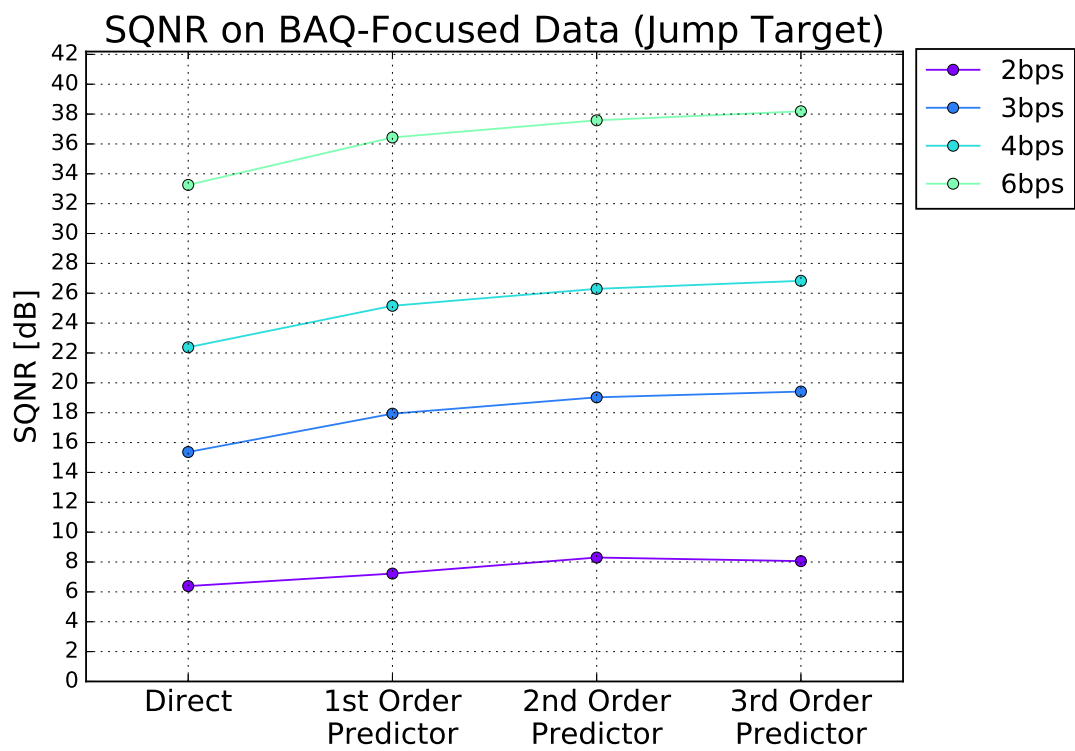
Figure 71: SQNR calculated on focused data at different orders of Predictive BAQ on a "Jump" target.

6.3.3 Gap Mitigation

As briefly introduced in Section 3.2, applying the beamforming in elevation (SCORE) in Tandem-L mission will inevitably introduce gaps. The PRI sequence shown in Figure 59 is designed to avoid two consecutive gaps in the azimuth domain [21]. Thus, the prediction needs to be adapted to this situation, taking into account that some samples will be missing. A novel approach wich applies predictive coding with missing samples is
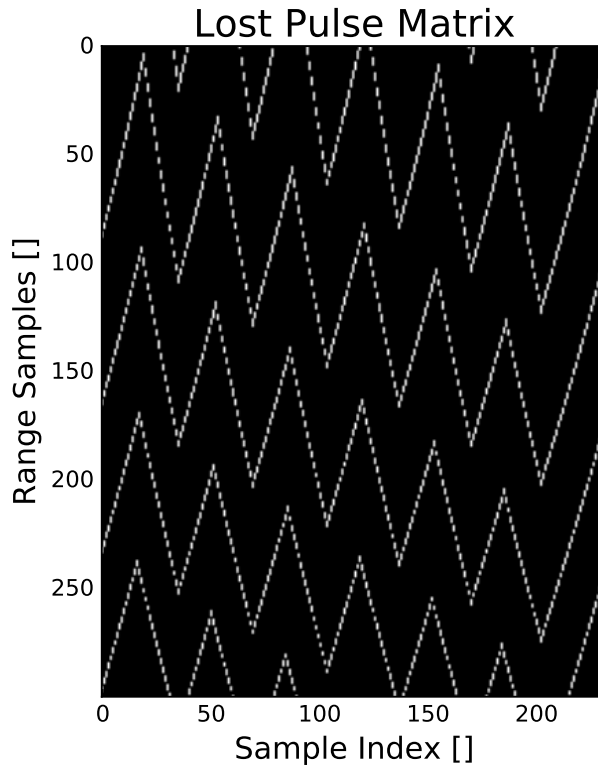

Figure 72: Example of gaps location (in white) along the acquired raw data matrix.

presented, named Predictive Coding Restart. The concept is to exploit a-priori knowledge on gap positions and modify the prediction for those samples. As the acquisition is performed, the presence of gaps is known onboard, making possible to flag those samples with 1 bit. When the prediction is estimating the value of a gap, a zero value is imposed by the restart technique. This allows the estimation of the following sample without the gap information, since the weight will be multiplied by the imposed zero. This of course is expecting to decrease the performance. The flag operation allows to discretize the gap with only 1 bit. In order to limiting the error near gaps, it is possible to exploit the N-1 bits which are not used for the gap sample. Two different approaches of bit reallocation have been presented, named "Post" and "Distributed". The first one assigns the gained bits from the gap to the subsequent samples: the idea is to have higher accuracy to quantize the difference which comes from a bad estimation, meaning that its dynamic will be larger than expected. The "Distributed" technique increases the encoding quality before and after the gap, having as main goal the increment of information in the gap neighborhood for a better interpolation. The rules and the examples of bit reallocation for the two strategy are reported in Table 4 and 5, respectively. A preliminary evaluation has been

"Post" bit allocation strategy			
bitrate	before gap	on gap	after gap
N	N	1	3N-N-1
2	2	1	3
3	3	1	5
4	4	1	7
5	5	1	9

Table 4: "Post" strategy bit allocation exploiting all the available bits.

"Distributed" bit allocation strategy			
bitrate	before gap	on gap	after gap
N	N+1	1	3N-N-2
2	2	1	3
3	4	1	4
4	5	1	6
5	6	1	8

Table 5: "Distributed" strategy bit allocation exploiting all the available bits.

done with a single azimuth line and an ADC quantizer. In addition, the analysis has been also performed by keeping a constant bitrate. In Figure 73 the SQNR on the entire raw signal including gaps is shown. As it is possible to notice, the proposed techniques seems to increase the performance of the constant bitrate case. By calculating the SQNR only on the samples after the gaps (Figure 74), clearly the "Post" strategy has higher accuracy in the estimation. However, in order to evaluate the performance of the two proposed methods, it is important to consider the signal after the interpolation. Especially, all the samples which are in the nearest position to a gaps have to be considered for SQNR evaluation, in this way, the actual impact of gaps to the final data is correctly characterized (Figure 75). From this last plot, the "Distributed" technique is clearly the best between the two, moreover the SQNR on the samples near the gap is the same of the SQNR on the whole signal. This means that the performance of the proposed technique is not subject to degradation due to gaps. Performing the same evaluation on the bidimensional scene, BAQ is employed to replace the ADC. As it is possible to notice, some bitrates are non applicable to BAQ method, as defined in Section 4.1.2. This is a limitation of the proposed method and needs to be adapted to BAQ constrains, which allows only 2, 3, 4, 6 and 8 (bypass) bits per sample. In Figure 76 and 77 the result for the "Distributed" strategy BAQ encoding at different orders of prediction is depicted. The degradated performance for the 6 bps case is due to the limitation of BAQ bitrate, which does not allow higher than 8 bps bitrates. As a confirmation result, Figure 78 shows the SQNR evaluated only in the nearest samples of gaps after the focusing operation. Also in this case the gap has no or negligible impact on the final result.

"Post" bit allocation strategy for BAQ				
bitrate	before gap	on gap	after gap	subsequent
2	2	1	3	2
3	3	1	4	4
4	4	1	6	4
6	6	1	8	8

Table 6: "Post" bit allocation strategy applied on BAQ compatible bitrates.

"Distributed" strategy bit allocation for BAQ					
bitrate	before gap	on gap	after gap	subsequent	subsequent
2	2	1	3	2	2
3	4	1	4	3	3
4	4	1	6	6	3
6	8	1	8	6	6

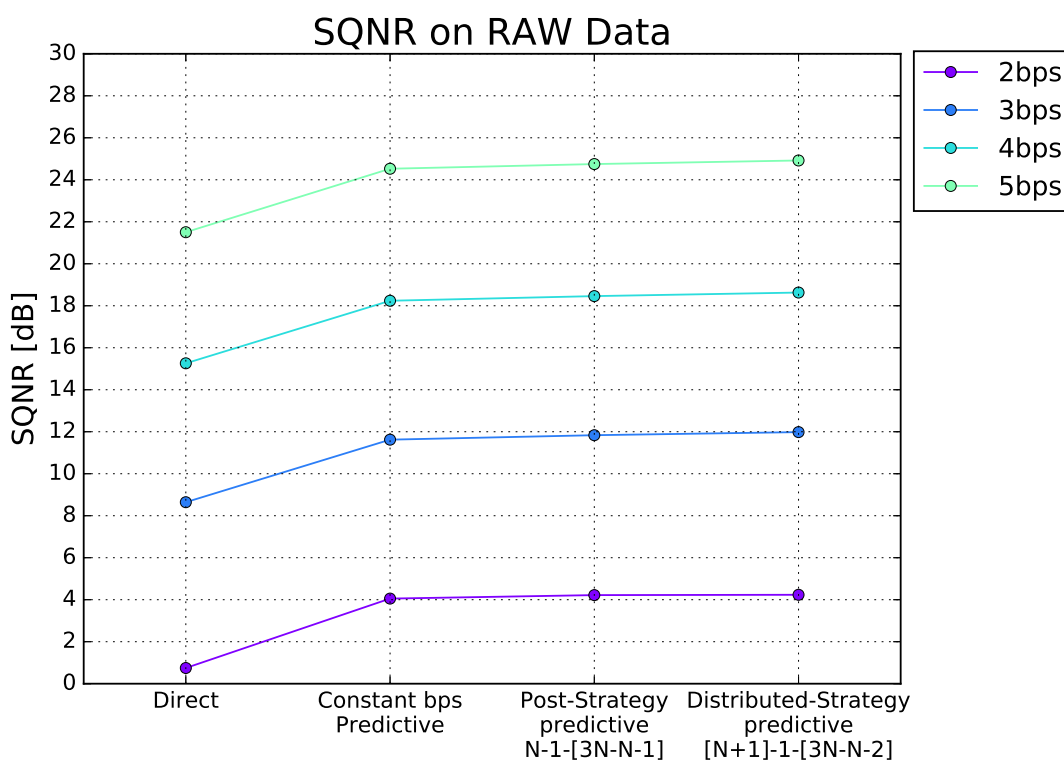Table 7: "Distributed" strategy bit allocation applied on BAQ compatible bitrates.

Figure 73: SQNR calculated on the whole raw data encoded with direct, "Post" and "Distributed" strategies.
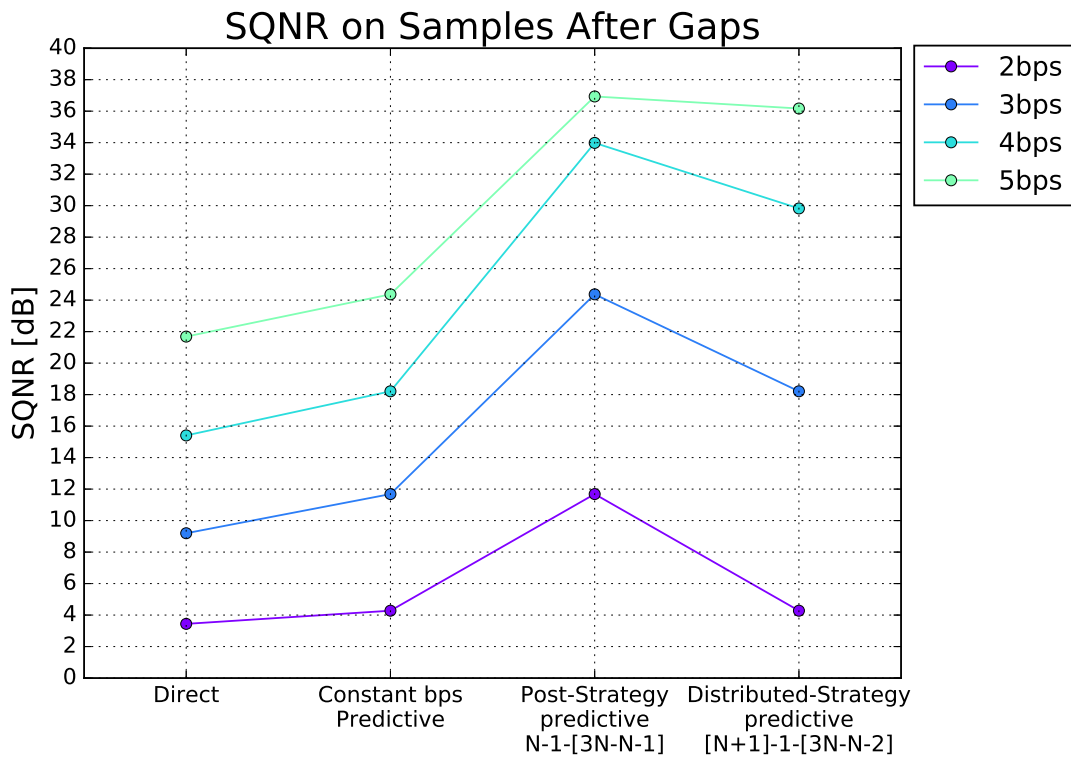
Figure 74: SQNR calculated on the samples after gaps encoded with direct, "Post" and "Distributed" strategies.
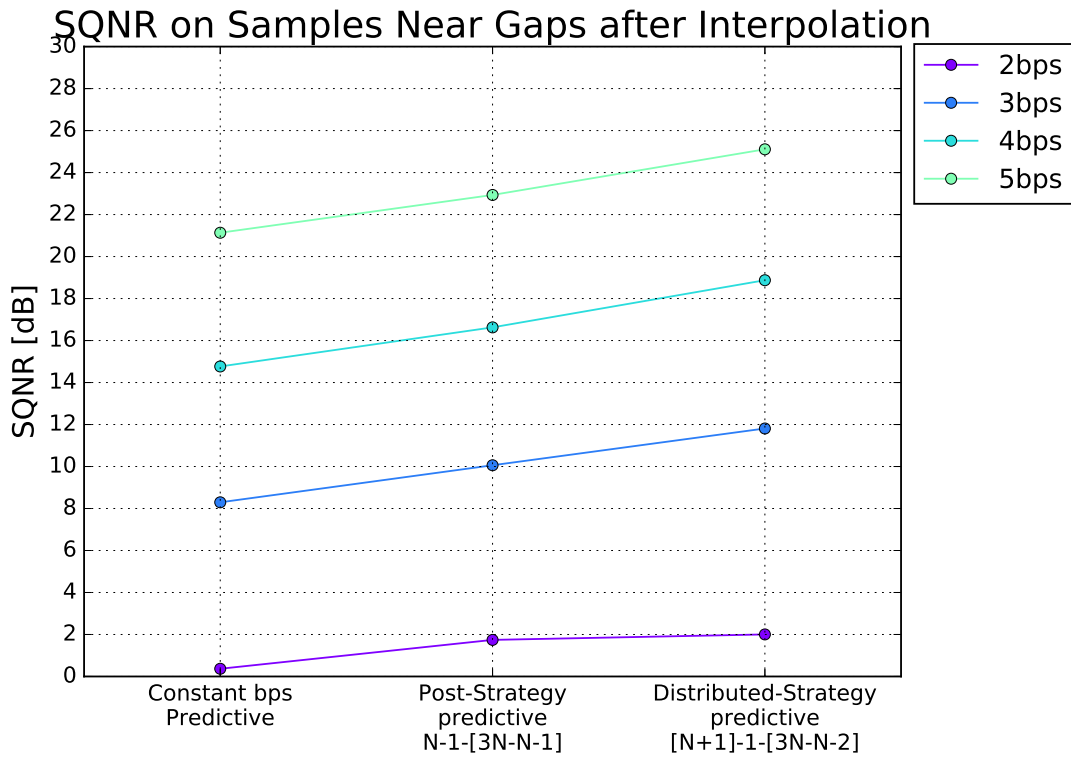
Figure 75: SQNR calculated on the samples near a gap after interpolation encoded with direct, "Post" and "Distributed" strategies.

Figure 76: SQNR calculated on the raw data encoded with "Distributed" strategy for different orders of prediction.

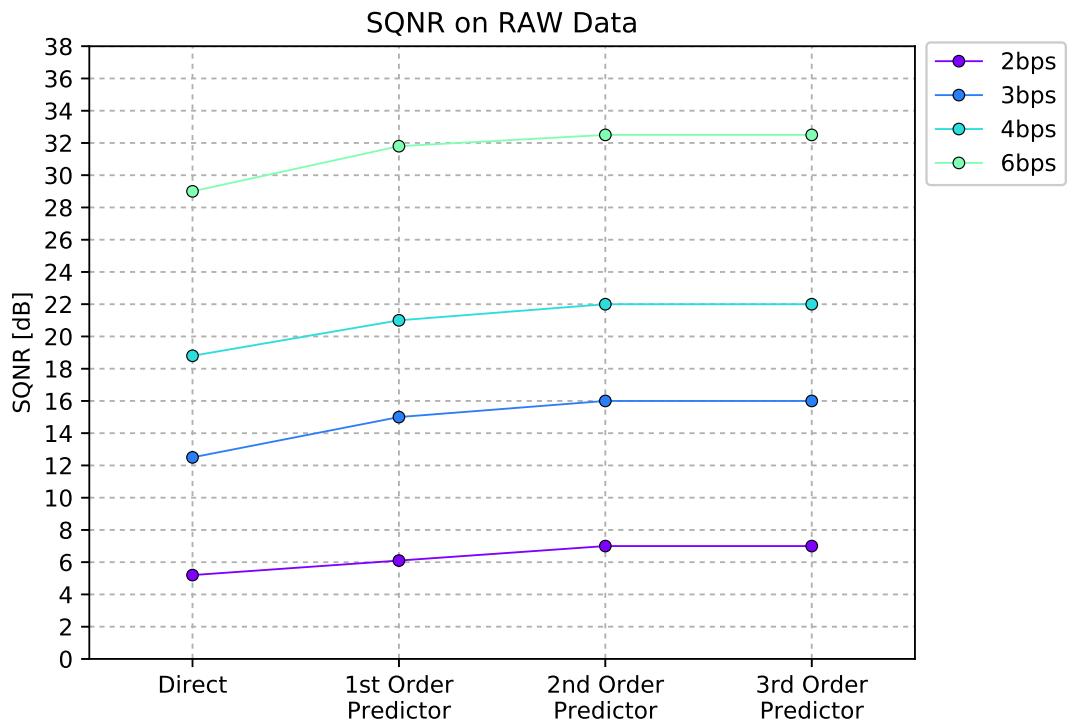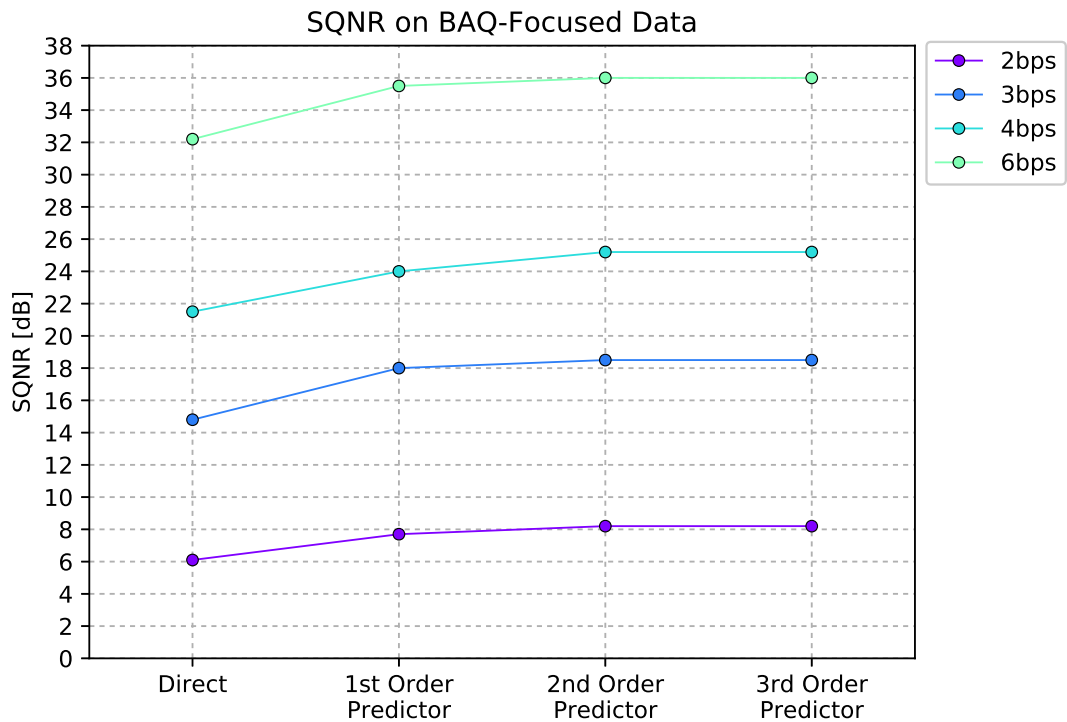Figure 77: SQNR calculated on the focused data encoded with "Distributed" strategy for different orders of prediction.
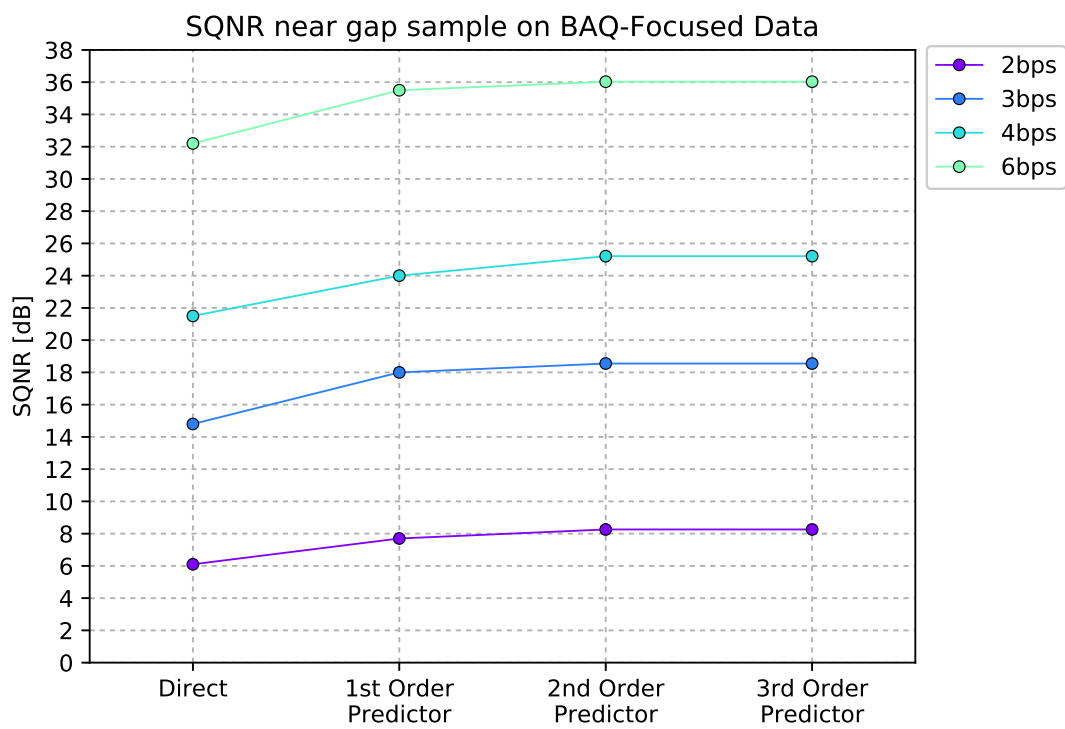
Figure 78: SQNR calculated on the samples near a gap after interpolation encoded with "Distributed" strategy for different orders of prediction.

7 Conclusion and Outlook

For present and future spaceborne SAR missions, an increasing amount of on-board data is going to be required, leading to hard requirements in terms of on-board memory and downlink capacity. In this context, SAR raw data quantization represents a critical aspect, since it affects both, the amount of data managed on board and transmitted to the ground, and the quality of the resulting SAR products. In this master thesis, data reduction for SAR systems by exploiting linear predictive quantization is addressed. The proposed novel data reduction approach is investigated in the context of the Tandem-L, a DLR L-band SAR mission proposal which employs staggered PRI which allows for a swath width up to 350 km, and resulting in a required data volume of about 8 Terabyte per day. The proposed technique takes advantage of the large azimuth oversampling needed for Tandem-L and exploits the resulting time variant autocorrelation properties of the non-uniform azimuth raw data stream in order to reduce the amount of data. To this purpose, Linear Predictive Coding and Block Adaptive Quantization are jointly exploited, and a novel quantization method is derived, named Predictive-Block Adaptive Quantization (P-BAQ). For this, different prediction orders are investigated by considering the trade-off between achievable performance and complexity. Monte Carlo simulations have been conducted on different target scenarios, showing that with the proposed technique an SQNR gain of about 4 dB can be achieved with a third-order linear predictor, which corresponds to a data reduction of about 10-15%. For this, a modest increase of the system complexity is required, since, for its implementation, up to three range lines and coefficients (weights) need to be stored and routed on board for prediction, for which a single FPGA should be sufficient. With respect to other suggested approaches, which implement a complex on-board processing in order to generate a decimated uniform data grid (leading to a data reduction of about 50%), the proposed method allows the availability of the non uniform data stream on ground, making possible future developments for advanced processing techniques with the oversampled data. Moreover, the presented solution is not dependent on the variable PRI of the system and the presence of gaps which occur due to the staggered SAR acquisition mode. The application on LPC to SAR data has been theoretically characterized according to a specific modelling of the autocorrelation function of the system along the azimuth domain. The reduction of the dynamic of the data is the crucial factor that allows to increase the performance, as the quantization error is proportional to it. The effective reduction of dynamic has been proved for different values of PRF. By deriving the theoretical gain and expressing it as function of the PRF, it is possible to know in advance the required complexity of the prediction for a given required gain. The mathematical description has been verified through Monte Carlo simulations preformed in a uniform PRI case, confirming the expected results from the theory for different values of PRF. The application of predictive quantization to the TanDEM-X system has been considered as well, showing poor quantization performance as the mission parameters are not suitable for this kind of technique. Moving to staggered PRI case, first an analysis by considering an extreme case of PRI variation has been performed, reporting the result

for different possible approaches considering different trade offs between complexity and accuracy of estimation. The LPC has shows to perform the same as the uniform PRI case even if the PRI is staggered. Applying the technique on an example of real PRI sequence of Tandem-L, the results confirms the expectations by maintaining the 4 dB gain. A complete bidimensional simulation has been performed both on distributed and "jump" target, featuring the joint operation of LPC and Block Adaptive Quantization (BAQ). The result of the technique on the complete scene simulation confirms the expected gain. Moreover, the implementation of a variable bitrate along the azimuth domain, known as Azimuth-Switched quantization, has demonstrated to reach the same performance of the direct BAQ implementation employing about 0.5 bit less per samples. The amount of reduced memory consumption is translated to an overall data reduction of 12.5%, as the employed bitrate for Tandem-L is of 4-bit BAQ.

Staggered SAR mode generates missing samples at some points of the azimuth domain. Being the prediction performed along the azimuth direction, a specific strategy to overcome this gaps without stopping the prediction has been successfully presented. The proposed technique, named "PC-Restart", exploits the usage of the a-priori knowledge of gaps position, allowing to assign a 1 bit flag in its positions and increase the bitrate before and after it. After interpolation, the values nearest to the gaps position are represented with the same accuracy (SQNR) as the overall signal.

This work represents a preliminary study for the research topic. As possible outlook, the proposed technique must be applied to real staggered data. A possible option of acquired data is the airborne Flugzeug SAR (F-SAR) [20] from DLR, which allows a specific setting of the instruments for making possible a Tandem-L-like raw data generation. For this, it is worth pointing out that it has been employed, for the simulations, a planar array approximation of the azimuth antenna pattern. It will be of great interest to analyze the performance of the proposed technique by considering real reflector patterns, and eventually take into account the pattern variation along range, which may have an impact on the resulting weights estimation. After the real data analysis, different options of improvements are planned. First of all, the application of polar BAQ together with LPC in order to exploit the circular symmetry of the complex raw data signal. Finally, the predictive process can be improved by considering more complex techniques, such as non-linear predictors, which may be further investigated to increase the data reduction capability of the system, eventually at the cost of a higher computational cost.

Bibliography

[1] Arthur Albert. The Gauss–Markov theorem for regression models with possibly singular covariances. *SIAM Journal on Applied Mathematics*, 24(2):182–187, 1973.

[2] Sergio Barbarossa and Alfonso Farina. Detection and imaging of moving objects with synthetic aperture radar. part 2: Joint time-frequency analysis by wigner-ville distribution. In *IEE Proceedings F (Radar and Signal Processing)*, volume 139, pages 89–97. IET, 1992.

[3] Jens Fischer, Ursula Benz, and Alberto Moreira. Efficient SAR raw data compression in frequency domain. In *Proceedings of International Geoscience and Remote Sensing Symposium (IGARSS), 1999*, pages 2261–2263, 1999.

[4] Nicolas Gebert, Felipe Almeida, and Gerhard Krieger. Advanced multi-channel SAR imaging—measured data demonstration. In *Proc. Int. Radar Symp (ISSPA)*, pages 525–529, 2009.

[5] Allen Gersho and Robert M Gray. *Vector quantization and signal compression.* Springer Science & Business Media, 2012.

[6] Sigurd Huber, Marwan Younis, and Gerhard Krieger. The TanDEM-X mission: overview and interferometric performance. *International Journal of Microwave and Wireless Technologies*, 2(3-4):379–389, 2010.

[7] Nuggehally Jayant and Peter Noll. *Digital Coding of Waveforms–Principles and Applications to Speech and Video Englewood Cliffs.* New Jersey: Prentice-Hall, 1984.

[8] Alon Kipnis, Yonina C Eldar, and Andrea J Goldsmith. Analog-to-digital compression: A new paradigm for converting signals to bits. *IEEE Signal Processing Magazine*, 35(3):16–39, 2018.

[9] Gerhard Krieger, Nicolas Gebert, Marwan Younis, Federica Bordoni, Anton Patyuchenko, and Alberto Moreira. Advanced concepts for ultra-wide-swath sar imaging. In *Synthetic Aperture Radar (EUSAR), 2008*, pages 1–4, 2008.

[10] Gerhard Krieger, Alberto Moreira, Hauke Fiedler, Irena Hajnsek, Marian Werner, Marwan Younis, and Manfred Zink. TanDEM-X: A satellite formation for high-resolution SAR interferometry. *IEEE Transactions on Geoscience and Remote Sensing*, 45(11):3317–3341, 2007.

[11] Gerhard Krieger, Marwan Younis, Nicolas Gebert, Sigurd Huber, Federica Bordoni, Anton Patyuchenko, and Alberto Moreira. Advanced digital beamforming concepts for future SAR systems. In *Proceedings of International Geoscience and Remote Sensing Symposium (IGARSS), 2010*, pages 245–248, 2010.

[12] Ronald Kwok and William TK Johnson. Block adaptive quantization of magellan SAR data. *IEEE Transactions on Geoscience and remote sensing*, 27(4):375–383, 1989.

[13] David C Lancashire, Bartholomew AF Barnes, and Stephen J Udall. Block adaptive quantization, July 3 2001. US Patent 6,255,987.

[14] Michele Martone, Benjamin Bräutigam, and Gerhard Krieger. Azimuth-switched quantization for SAR systems and performance analysis on TanDEM-X data. *IEEE Geoscience and Remote Sensing Letters*, 11(1):181–185, 2014.

[15] Michele Martone, Benjamin Bräutigam, and Gerhard Krieger. Quantization effects in TanDEM-X data. *IEEE Transactions on Geoscience and Remote Sensing*, 53(2):583–597, 2015.

[16] Alberto Moreira and Fabian Blaser. Fusion of block adaptive and vector quantizer for efficient SAR data compression. In *Proceedings of International Geoscience and Remote Sensing Symposium (IGARSS), 1993*, pages 1583–1585, 1993.

[17] Alberto Moreira, Gerhard Krieger, Irena Hajnsek, Konstantinos Papathanassiou, Marwan Younis, Paco Lopez-Dekker, Sigurd Huber, Michelangelo Villano, Matteo Pardini, Michael Eineder, Francesco De Zan, and Alessandro Parizzi. Tandem-L: A highly innovative bistatic SAR mission for global observation of dynamic processes on the Earth's surface. *IEEE Geoscience and Remote Sensing Magazine*, 3(2):8–23, 2015.

[18] Alberto Moreira, Pau Prats-Iraola, Marwan Younis, Gerhard Krieger, Irena Hajnsek, and Konstantinos Papathanassiou. A tutorial on synthetic aperture radar. *IEEE Geoscience and Remote Sensing Magazine*, 1(1):6–43, 2013.

[19] Cristina Párraga Niebla and Gerhard Krieger. Optimization of block-adaptive quantization for SAR raw data. *Space Technology*, 23(2):131–141, 2003.

[20] Marc Rodriguez-Cassola, Stefan V Baumgartner, Gerhard Krieger, and Alberto Moreira. Bistatic TerraSAR-X/F-SAR spaceborne–airborne SAR experiment: description, data processing, and results. *IEEE Transactions on Geoscience and Remote Sensing*, 48(2):781–794, 2010.

[21] Michelangelo Villano. *Staggered synthetic aperture radar.* PhD dissertation, Deutsches Zentrum für Luft-und Raumfahrt (DLR), 2016.

[22] Michelangelo Villano, Gerhard Krieger, and Alberto Moreira. Staggered SAR: High-resolution wide-swath imaging by continuous PRI variation. *IEEE Transactions on Geoscience and Remote Sensing*, 52(7):4462–4479, 2014.

[23] Michelangelo Villano, Gerhard Krieger, and Alberto Moreira. Onboard processing for data volume reduction in high-resolution wide-swath SAR. *IEEE Geoscience and Remote Sensing Letters*, 13(8):1173–1177, 2016.

[24] Rolf Werninghaus. TerraSAR-X mission. In *SAR Image Analysis, Modeling, and Techniques VI*, volume 5236, pages 9–17. International Society for Optics and Photonics, 2004.

[25] Marwan Younis, Johannes Böer, Carlos Ortega, Daniel Schulze, Sigurd Huber, and Josef Mittermayer. Determining the optimum compromise between SAR data compression and radiometric performance-An approach based on the analysis of TerraSAR-X data. In *Proceedings of International Geoscience and Remote Sensing Symposium (IGARSS), 2008*, pages 104–107, 2008.

[26] Manfred Zink, Hauke Fiedler, Irena Hajnsek, Gerhard Krieger, Alberto Moreira, and Marian Werner. The TanDEM-X mission concept. In *Proceedings of International Geoscience and Remote Sensing Symposium (IGARSS), 2006*, pages 1938–1941, 2006.